VILNIUS UNIVERSITY

ŠARŪNAS MASYS

INVESTIGATION OF ELECTRONIC AND CRYSTALLINE STRUCTURE OF PEROVSKITE CRYSTALS

Doctoral Dissertation

Physical Sciences, Physics (02 P)

Vilnius, 2014

Doctoral Dissertation was prepared at Institute of Theoretical Physics and Astronomy of Vilnius University in 2009–2013.

Scientific Supervisor:

Dr. Valdas Jonauskas (Vilnius University, Physical Sciences, Physics — 02 P)

VILNIAUS UNIVERSITETAS

ŠARŪNAS MASYS

PEROVSKITINIŲ KRISTALŲ ELEKTRONINĖS IR KRISTALINĖS SANDAROS TYRIMAS

Daktaro disertacija

Fiziniai mokslai, fizika (02 P)

Vilnius, 2014 metai

Daktaro disertacija 2009–2013 metais rengta Vilniaus universiteto Teorinės fizikos ir astronomijos institute.

Mokslinis vadovas:

dr. Valdas Jonauskas (Vilniaus universitetas, fiziniai mokslai, fizika — 02 P)

Acknowledgements

It is a delight to acknowledge those who have impacted me both personally and professionally over the last several years. In the first place, I would like to thank my supervisor, Dr. Valdas Jonauskas, for his guidance, insight, encouragement, and remarkable support in every step I take towards the deeper knowledge of Physics. I am also grateful to Dr. Alicija Kupliauskienė for her understanding and helpful advices. Many thanks to my colleagues, Aušra and Sigitas, for all the cheerful moments spent together.

I am indebted to my family and beloved Daina for the care, patience, and inexhaustible belief. Nothing would make sense without you.

Contents

List of the Most Common Abbreviations

BLYP — Becke-Lee-Yang-Parr

BM — Birch-Murnaghan

DFT — Density Functional Theory

DMFT — Dynamical Mean-Field Theory

DOS — Density Of States

EL — Euler-Lagrange

FWHM — Full Width at Half Maximum

GGA — Generalized Gradient Approximation

HAXPES — HArd X-ray PhotoEmission Spectroscopy

HF — Hartree-Fock

HK — Hohenberg-Kohn

KS — Kohn-Sham

LCAO — Linear Combination of Atom-centred [Gaussian] Orbitals

LDA — Local Density Approximation

MARE — Mean Absolute Relative Error

MLs — MonoLayers

PBE — Perdew-Burke-Ernzerhof

PDOS — Projected DOS

PSW — Partial Spectral Weight

SIC — Self-Interaction Correction

SIE — Self-Interaction Error

SOGGA — Second-Order GGA

TF — Thomas-Fermi

TPSS — Tao-Perdew-Staroverov-Scuseria

UPS — Ultraviolet Photoemission Spectroscopy

VRH — Voigt-Reuss-Hill

WC — Wu-Cohen

WS — Wigner-Seitz

XC — eXchange-Correlation

Chapter 1

Introduction

The whole story begins in 1839, when the naturally occurring mineral $CaTiO_3$ was discovered in the Ural Mountains by German geologist Gustav Rose. The name *perovskite* was given for $CaTiO_3$ in honour of the eminent Russian mineralogist Lev Alexevich von Perovski. However, nowadays the *perovskite crystals* are associated with a vast family of crystalline ceramics which structures are based on that of $CaTiO_3$ [1, 2]. To a surprise of many, the following family comprises several compounds that are thought to be the main constituents of the Earth's lower mantle [3].

Perovskite-structured oxides are represented by the general formula ABO_3, in which A elements can be rare earth, alkaline earth, alkali, and other large ions, whereas B elements can be $3d$, $4d$, and $5d$ transition metal ions [4]. These materials have attracted and challenged the interest and curiosity of scientific community for many decades due to the enormous variety of complex phenomena — from ferroelectricity, ferromagnetism, and piezoelectricity up to insulator-to-metal transition, weak ferromagnetism, colossal magnetoresistance, and superconductivity — arising from the subtle coupling between structural, electronic, and magnetic degrees of freedom [5–7]. Needless to say, the perovskite oxides have already found their applications in numerous technological areas such as electrochemistry, heterogeneous catalysis, and modern solid-sate electronics, thereby paving the way for novel solutions in different sectors of emerging sciences [1, 8].

Among the diverse family of perovskite oxides, $LaNiO_3$ is a rare example characterized by paramagnetic metallic behaviour down to the lowest temperatures and being structurally compatible with many functional layers [9, 10]. For a long time, the technological interest in this nickelate has been limited to the development of highly conductive bottom electrodes for various ferroelectric thin film devices [11–13]. But recently, the enthusiasm was renewed by experimental recognition of electric-field tunable metal-to-insulator transition and theoretical findings that heterostructures and superlattices composed of thin $LaNiO_3$ layers separated by wide-gap insulators could possibly exhibit high-temperature superconductivity [14–16]. Of course, the fact that the hunt for novel superconducting materials is at the vanguard of condensed matter physics research sheds a new light on the outlook of $LaNiO_3$, but on the other hand, it does not automatically mean that the bulk properties of this oxide are already fully explored. One can find that in a variety of theoretical studies [17–20] based on conventional density functional theory (DFT) and beyond-DFT techniques the electronic structure of $LaNiO_3$ has been merely analysed for its valence band rather than as a whole made of valence and core states. Since electrons in perovskites can exhibit strongly pronounced localized and delocalized characters, the proper methods for describing valence and core states may significantly differ and therefore provide some useful insights into the electronic structure. In addition, the comprehensive analysis of chemical bonding and importance of relativistic effects should also be reconsidered and taken into account in order to deepen the knowledge of physics that lies behind $LaNiO_3$.

Similar to $LaNiO_3$, $SrRuO_3$ is another well-known perovskite oxide possessing many beneficial properties. This conducting ferromagnetic ruthenate with the Curie temperature of 160 K [21] is a material of uncommon scientific interest due to its outstanding electrical, magnetic, and thermal properties, high resistant to chemical solutions, and low lattice mismatch with plenty of functional oxides [22–24]. In recent years, $SrRuO_3$ has become the most popular epitaxial electrode for complex oxide heterostructures and has been utilized in ferroelectrics, Schottky junctions, magnetocalorics, and magnetoelectrics [25–28]. Moreover, it has attracted the attention of superconductor and spintronics communities [23, 29, 30]. Reflecting this broad interest, about 1000 papers spanning the physics, materials science, and applications of $SrRuO_3$ have been published over the last two decades. But, despite all that has been learned, a thorough understanding of $SrRuO_3$ is still lacking.

Some of the most important open questions in the physics of $SrRuO_3$ are its degree of electron correlation and what factors control it. Due to the highly extended nature of Ru 4*d* orbitals, it is natural to expect that electron correlation effects in ruthenates should be weak. However, in the literature there are several studies [31–33] — in contrast to some others [34–36] — indicating the presence of strong electron correlation in $SrRuO_3$. Being essentially based on photoemission spectroscopy observation of the incoherent part of the spectrum dominating over the coherent one, this phenomenon prevents from reaching the general consensus on the microscopic origin of the physical properties of $SrRuO_3$. This is because it is widely assumed that the coherent feature at the Fermi level (E_F) basically represents the extended states of Ru 4*d* orbitals, whereas the incoherent feature at 1.2–1.5 eV below E_F should be attributed to the presence of the localized electronic states and therefore taken as a direct evidence of the manifestation of strong electron correlation effects. Although various theoretical methods [37–39] were applied to reproduce experimental findings, the electronic structure of $SrRuO_3$ has not been completely elucidated due to different, and in some cases contrasting, conclusions.

Concerning the crystalline structure of $SrRuO_3$, it should be noted that calculations available so far were done at its orthorhombic and cubic phases[1] using standard DFT approaches [37,39,41,42]. A recent work [43] also includes revised DFT functionals together with several combinations of their hybrid schemes, but despite that, it is somehow surprising that in the literature scarcely any first-principles calculations of tetragonal $SrRuO_3$ have been reported to date. Even more intriguingly, one can hardly find any theoretical or experimental investigation on the elastic properties of $SrRuO_3$, except for several polycrystalline measurements for the orthorhombic phase at its paramagnetic configuration [44–46]. Having in mind that high-temperature tetragonal phase has been recently stabilized at ambient conditions by tensile strain and introduction of oxygen vacancies [47–50], the deep knowledge of structural parameters, elastic features, and mechanical stability becomes highly necessary for both technological and fundamental reasons.

From all that has been stated above, it is clear that, for one reason or another, the investigation of $LaNiO_3$ and $SrRuO_3$ is far from over allowing us to contribute by solving the questions under debate and raising the new ones.

---

[1] Upon heating, $SrRuO_3$ undergoes a series of phase transformations: orthorhombic $\xrightarrow{820\ \mathrm{K}}$ tetragonal $\xrightarrow{950\ \mathrm{K}}$ cubic [40].

1.1 The Main Goal and Tasks of the Study

The main goal of the present study is to systematically investigate the electronic and crystalline structure of $LaNiO_3$ and $SrRuO_3$ by combining the most appropriate theoretical tools and available experimental data. To be more specific, for $LaNiO_3$ more focus is placed on the electronic structure of the core states, relativistic effects, and chemical bonding, whereas for $SrRuO_3$ more emphasis is put on the coherent and incoherent features of the binding energy spectrum, introduction of vacancies, and elasticity. Thus, in order to achieve this goal, the following tasks are to be done:

- Perform full geometry optimization and make a thorough analysis on obtained structural parameters to find out the exchange-correlation functionals that best simulate the low-temperature experimental data.
- Calculate the density of states to reproduce and identify the spectral peaks at the core and valence bands of $LaNiO_3$.
- Carry out the Mulliken population analysis and visualize the electron density difference map to determine the chemical bonding in $LaNiO_3$.
- Calculate the density of states and evaluate the impact of coherent and incoherent features in low-energy and high-energy photoemission spectra of $SrRuO_3$.
- Determine the role of oxygen vacancies for the manifestation of strong electron correlation effects in $SrRuO_3$.
- Evaluate single-crystal elastic constants, macroscopic elastic parameters, and mechanical stability of $SrRuO_3$.

1.2 Scientific Novelty and Relevance

For $LaNiO_3$, it is shown that hybrid functionals substantially improve the description of the binding energy peak positions in the core region thus allowing to reproduce the experiment without the usage of more sophisticated and computationally demanding methods. What is more, the inclusion of spin-orbit interaction enables to correctly distinguish the contribution of O 2*s* and La 5*p* states to the spectrum, whereas the complete picture of chemical bonding is determined from the combination of mutually consistent electron density difference map, Mulliken population analysis, and hybridization of corresponding orbitals.

For $SrRuO_3$, it is demonstrated that revised functionals effectively improve the description of the crystalline structure mostly due to the modification of a single parameter in exchange. Concerning the electronic structure, a strong proof that $SrRuO_3$ does not naturally possess different electronic states at its bulk and surface is provided. In addition, it is revealed that the incoherent feature which experimentally manifests itself as a broad shoulder at 1.2–1.5 eV below E_F could be due to the finite admixture of O 2*p* states and the asymmetric shape of the coherent Ru 4*d* peak at E_F. Moreover, the influence of introduction of oxygen vacancies on the binding energy spectrum implies that oxygen vacancies might be responsible for what was previously attributed to the strong electron correlation effects in stoichiometric specimens. Concerning the elasticity, single-crystal elastic constants and macroscopic elastic parameters calculated using a variety of functionals at least partially fill the existing gap of knowledge. The discovery of mechanical instability of tetragonal $SrRuO_3$ and isosymmetric phase transition of orthorhombic $SrRuO_3$ raises new questions about the fundamental nature and technological applications of this material.

1.3 Statements Presented for the Defence

1. DFT approximations and their hybrid schemes applied for the different regions of the binding energy spectrum allow to accurately simulate the essential photoemission results of $LaNiO_3$. Yet, the correct identification of the peaks in the core region requires relativistic treatment, namely, the inclusion of spin-orbit interaction.

2. $SrRuO_3$ is a weakly correlated material with a clearly expressed coherent Ru 4*d* peak at the Fermi level. An introduction of oxygen vacancies into

$SrRuO_3$ reproduces the previously observed strong spectral weight transfer from coherent to incoherent feature.

3. Tetragonal $SrRuO_3$ is mechanically unstable at zero temperature and pressure conditions. The structural transformation that is related to the transition to energetically lower states is an abrupt reorientation of RuO_6 octahedra around x and z axes.

4. Under C_{44} related shear deformation, orthorhombic $SrRuO_3$ undergoes an isosymmetric phase transition at the critical strain values of $\sim \pm 0.02$. The structural transformation which is associated with the following behaviour is a strongly pronounced rotation of RuO_6 octahedra around z axis.

1.4 Author's Contribution and Approbation of the Results

The author has performed the theoretical calculations, analysed the obtained data, and together with co-authors prepared the publications.

The results were published in 4 scientific papers:

1. Š. Masys, S. Mickevičius, S. Grebinskij, and V. Jonauskas, "Electronic structure of $LaNiO_{3-x}$ thin films studied by x-ray photoelectron spectroscopy and density functional theory," Phys. Rev. B **82**, 165120 (2010).

2. S. Grebinskij, Š. Masys, S. Mickevičius, V. Lisauskas, and V. Jonauskas, "*Ab initio* and photoemission study of correlation effects in $SrRuO_3$ thin films," Phys. Rev. B **87**, 035106 (2013).

3. Š. Masys, V. Jonauskas, S. Grebinskij, S. Mickevičius, V. Pakštas, and M. Senulis, "Theoretical and experimental study of non-stoichiometric $SrRuO_3$: A role of oxygen vacancies in electron correlation effects," Lith. J. Phys. **53**, 150 (2013).

4. Š. Masys and V. Jonauskas, "A first-principles study of structural and elastic properties of bulk $SrRuO_3$," J. Chem. Phys. **139**, 224705 (2013).

The results were presented at 4 scientific conferences:

1. Š. Masys, V. Jonauskas, S. Mickevičius, and S. Grebinskij, “Electronic structure of $LaNiO_{3-x}$ thin films: X-ray photoelectron spectroscopy and theoretical study,” Radiation Interaction with Material and Its Use in Technologies 2010: 3rd International Conference, Kaunas, Lithuania, 20–23 September, 2010: Program and Materials, p. 129–132.

2. Š. Masys, V. Jonauskas, E. Baškys, S. Mickevičius, and S. Grebinskij, “Experimental and *ab initio* study on valence-band structure of $SrRuO_3$,” Radiation Interaction with Material and Its Use in Technologies 2012: 4th International Conference, Kaunas, Lithuania, 14–17 May, 2012: Program and Materials, p. 593–596.

3. Š. Masys and V. Jonauskas, “Elastic properties of perovskite $SrRuO_3$: An employment of revised density functional for solids,” Solid State Chemistry 2012: 10th International Conference, Pardubice, Czech Republic, 10–14 June, 2012: Book of Abstracts, p. 175.

4. Š. Masys and V. Jonauskas, “Ortorombinės $SrRuO_3$ fazės elastinės savybės [Elastic properties of orthorhombic phase of $SrRuO_3$],” 40-oji Lietuvos nacionalinė fizikos konferencija: programa ir pranešimų tezės, Vilnius, 2013 m. birželio 10–12 d., p. 61.

Chapter 2

Review of Density Functional Theory

> *"I think I can safely say that nobody understands quantum mechanics."*
>
> Richard P. Feynman

2.1 Introduction

Density functional theory (DFT) has had a major impact on electronic-structure calculations by giving a sounder theoretical basis than they ever had before [51]. Over the past twenty years, this theory has turned to one of the most efficient and widely used tools in molecular quantum chemistry as well as solid-state physics [52], providing useful predictions for atoms, molecules (including biomolecules), nanostructures, solids, and solid surfaces [53]. Moreover, the combination of DFT with new and powerful linearized methods for solving self-consistent single-particle Schrödinger-like equations has led to an outburst of electronic-structure works in condensed matter physics. The striking success of DFT has come despite the complaints about arbitrary parametrization of potentials and gripes about the absence of a universal principle (other than comparison with experiment) that can guide improvements in the way the variational principle has led the development of wavefunction-based methods [54]. Naturally, a great part of the following success lies in the fact that DFT-based calculations have the advantage of a significant economy of computational resources compared with calculations of a many-body wavefunction.[1] DFT simply avoids the problem of calculating the many-electron ground-state wavefunction. Instead, ground-state properties — such as total energies, lattice constants, and magnetic moments — are directly

---

[1] This is certainly the case for the approximations of exchange-correlation functional, however, this is not necessarily true for the exact form of it. One should not rule out the possibility that the exact form of exchange-correlation functional might be rather complicated and thus much more computationally demanding [55].

expressed in terms of the electron density[2] $n(\mathbf{r})$, which in a given state determines the probability of finding any of the N electrons[3] within the volume element d^3r at point $\mathbf{r}$:

$$n(\mathbf{r}) = N \int \dots \int |\Psi(\mathbf{x}, \mathbf{x}_2, \dots, \mathbf{x}_N)|^2 ds d^3x_2 \dots d^3x_N. \tag{2.1}$$

Here, $\Psi(\mathbf{x}, \mathbf{x}_2, \dots, \mathbf{x}_N) \equiv \Psi(\mathbf{x}_1, \mathbf{x}_2, \dots, \mathbf{x}_N)$ denotes a wavefunction for an N-electron system and notation $(\mathbf{x} \equiv \mathbf{r}, s)$ stands for the set of spatial and spin coordinates. Generally, $n(\mathbf{r})$ is a non-negative function of only the three spatial variables which vanishes at infinity and integrates to the total number of electrons:

$$\int n(\mathbf{r}) d^3r = N. \tag{2.2}$$

It is obvious that while the complexity of a wavefunction increases with the number of electrons, the electron density has the same number of variables, independently of the system size [55]. Therefore, $n(\mathbf{r})$ is a simpler quantity to deal with both conceptually and practically. Besides, electron density is an observable and can be measured experimentally — in contrast to the elusive and somewhat mysterious nature of the wavefunction [54].

2.2 The Basics

The strengths of a modern DFT are practicality, universality, and a sound theoretical foundation [53] — the Hohenberg-Kohn (HK) theorems [57] and the Kohn-Sham (KS) equations [58]. Within the adiabatic approximation, the Hamiltonian of the system with M nuclei and N electrons can be described:[4]

$$\hat{H} = -\frac{1}{2}\sum_{i=1}^{N} \nabla_i^2 + \sum_{i=1}^{N}\sum_{i<j}^{N} \frac{1}{|\mathbf{r}_i - \mathbf{r}_j|} - \sum_{i=1}^{N}\sum_{A=1}^{M} \frac{Z_A}{|\mathbf{R}_A - \mathbf{r}_i|} + \sum_{A=1}^{M}\sum_{A<B}^{M} \frac{Z_A Z_B}{|\mathbf{R}_A - \mathbf{R}_B|}, \tag{2.3}$$

---

[2] Strictly speaking, $n(\mathbf{r})$ is a probability density, but calling it electron or one-electron density is a common practice [56].

[3] We are interested in probability of finding the electron with any spin. See Appendix B for details.

[4] Time-independent, non-relativistic, expressed in atomic units: $e = m_e = \hbar = \frac{1}{4\pi\varepsilon_0} = 1$.

where Z is the atomic number, while $\mathbf{r}$ and $\mathbf{R}$ denote the coordinates of the electrons and nuclei, respectively. In Cartesian coordinates, the Laplacian ∇_i^2 is given by

$$\nabla_i^2 = \left(\frac{\partial^2}{\partial x_i^2} + \frac{\partial^2}{\partial y_i^2} + \frac{\partial^2}{\partial z_i^2} \right). \tag{2.4}$$

Since the nuclear repulsion term[5] may be considered as a constant, the electronic Hamiltonian of the same system can be written in the form of

$$\hat{H} = \hat{T} + \hat{U} + \hat{V} = -\frac{1}{2}\sum_{i=1}^{N} \nabla_i^2 + \sum_{i=1}^{N}\sum_{i<j}^{N} U(\mathbf{r}_i, \mathbf{r}_j) + \sum_{i=1}^{N} V(\mathbf{r}_i), \tag{2.5}$$

in which $\hat{T}$, $\hat{U}$, and $\hat{V}$ correspondingly represent the kinetic energy, the repulsive potential due to the electron-electron interaction, and the external potential acting on the electrons from nuclei and any additional external fields. One can note that (2.5) is uniquely determined by the number of electrons and the external potential, thus providing the identity of the system under consideration. In other words, terms $\hat{T}$ and $\hat{U}$ are universal for any N-electron system, whereas $\hat{V}$ is the term that completely fixes the particular Hamiltonian. This observation sets the stage for the first HK theorem which legitimizes the use of electron density as a basic variable [59]. It states that, for non-degenerate ground states, *the external potential $V(\mathbf{r})$ is determined, within a trivial additive constant, by the electron density $n(\mathbf{r})$*. The proof of the theorem is disarmingly simple, since it is based on the minimum-energy principle for the ground state. Assume two different external potentials $V_1(\mathbf{r})$ and $V_2(\mathbf{r})$ resulting in the same electron density $n(\mathbf{r})$ for some N-electron system. Two different potentials imply that the two Hamiltonians are different, $\hat{H}_1$ and $\hat{H}_2$, and the corresponding lowest energy wavefunctions are also different, Ψ_1 and Ψ_2. Taking Ψ_2 as an approximate function for $\hat{H}_1$ and applying the variational principle yields

$$\begin{aligned} E_1 < \langle \Psi_2 | \hat{H}_1 | \Psi_2 \rangle = \\ \langle \Psi_2 | \hat{H}_2 | \Psi_2 \rangle + \langle \Psi_2 | \hat{H}_1 - \hat{H}_2 | \Psi_2 \rangle = E_2 + \int n(\mathbf{r})[V_1(\mathbf{r}) - V_2(\mathbf{r})] d^3 r, \end{aligned} \tag{2.6}$$

---

[5] The last term in (2.3).

where E_1 and E_2 are the ground-state energies for $\hat{H}_1$ and $\hat{H}_2$, respectively. Analogously

$$E_2 < \langle\Psi_1|\,\hat{H}_2\,|\Psi_1\rangle = \langle\Psi_1|\,\hat{H}_1\,|\Psi_1\rangle + \langle\Psi_1|\,\hat{H}_2 - \hat{H}_1\,|\Psi_1\rangle = E_1 + \int n(\mathbf{r})[V_2(\mathbf{r}) - V_1(\mathbf{r})]d^3r. \quad (2.7)$$

Addition of these two inequalities leads to the contradiction

$$E_1 + E_2 < E_2 + E_1, \quad (2.8)$$

revealing that the assumption was wrong. It means that there cannot be two different $V(\mathbf{r})$ that give the same $n(\mathbf{r})$ for their ground state. Therefore, there is one-to-one correspondence between the electron density and the external potential. By taking into account (2.2), it becomes obvious that $n(\mathbf{r})$ uniquely determines the Hamiltonian and hence all the properties of the system. Consequently, wavefunction, as well as energy, can be treated as a unique functional[6] of the electron density, $\Psi[n]$ and $E[n]$, respectively.

Now, the total ground-state electronic energy can be written in the form of

$$E[n] = \langle\Psi|\,\hat{T} + \hat{U} + \hat{V}\,|\Psi\rangle = T[n] + U[n] + \int n(\mathbf{r})V(\mathbf{r})d^3r, \quad (2.9)$$

where $T[n]$ is the kinetic energy and $U[n]$ denotes electron-electron interaction, containing the classical Coulomb repulsion, $J[n]$:

$$J[n] = \frac{1}{2}\int\int \frac{n(\mathbf{r})n(\mathbf{r}')}{|\mathbf{r} - \mathbf{r}'|} d^3r d^3r'. \quad (2.10)$$

The second HK theorem introduces the variational principal into DFT. It states that *for a trial density* $\tilde{n}(\mathbf{r})$*, such that* $\tilde{n}(\mathbf{r}) \geqslant 0$ *and* $\int \tilde{n}(\mathbf{r})d^3r = N$*,*

$$E[n] \leqslant E[\tilde{n}] \quad (2.11)$$

---

[6] Remember that a *function* is a rule for going from a variable, x, to a number, $f(x)$. A *functional* is a rule for going from a function, $f(x)$, to a number, $F[f]$. In other words, a functional is a function of which the variable is a function [59].

where $E[\tilde{n}]$ *is the energy functional of* (2.9) *and* $E[n]$ *corresponds to the exact ground-state energy.* This theorem simply proves that the true ground-state density minimizes the total electronic energy of the system. Since the first HK theorem allows $\tilde{n}(\mathbf{r})$ to determine its own external potential, Hamiltonian, and wavefunction, the latter can be taken as a trial function for the Hamiltonian generated from the true external potential $V(\mathbf{r})$. Thus,

$$\langle\tilde{\Psi}|\,\hat{H}\,|\tilde{\Psi}\rangle = T[\tilde{n}] + U[\tilde{n}] + \int \tilde{n}(\mathbf{r})V(\mathbf{r})d^3r = E[\tilde{n}] \geqslant E[n]. \tag{2.12}$$

Assuming that $E[n]$ is differentiable, the variational principle (2.11) requires the ground-state density to satisfy the stationary principle. By incorporating the N-electron constraint on the density with a Lagrangian multiplier μ, the stationary condition at the minimum can be formulated as

$$\delta\left[E[n] - \mu\left(\int n(\mathbf{r})d^3r - N\right)\right] = 0, \tag{2.13}$$

which leads to the Euler-Lagrange (EL) equation

$$\mu = \frac{\delta E[n]}{\delta n(\mathbf{r})} = \frac{\delta T[n]}{\delta n(\mathbf{r})} + \frac{\delta U[n]}{\delta n(\mathbf{r})} + V(\mathbf{r}). \tag{2.14}$$

If we knew the exact form of $T[n]$ and $U[n]$, (2.14) would be an exact equation for the ground-state electron density. Unfortunately, the HK theorems do not provide this, only that they exist. Note that $T[n]$ and $U[n]$ are defined independently of the external potential $V(\mathbf{r})$, so once we have a form for these functionals they can be applied to any of the system at hand. It becomes obvious that the explicit form of $T[n]$ and $U[n]$ is the major challenge of DFT.

The kinetic energy has a large contribution to the total energy,[7] therefore it cannot be represented poorly, since even small errors may prove disastrous. Unfortunately, due to many-body effects the explicit form of $T[n]$ lies in the dark. The basic idea in the KS formalism is splitting the kinetic energy functional into two parts — one of which is calculated exactly and the remaining is treated as a

---

[7] It is common to assume that $|T[n]| >> |E_{\mathrm{X}}[n]| > |E_{\mathrm{C}}[n]|$ where the exchange term $|E_{\mathrm{X}}[n]|$ is typically ten times greater than the correlation term $|E_{\mathrm{C}}[n]|$. However, $E_{\mathrm{XC}}[n]$ plays a crucial role, since without it atoms would bond weakly if at all.

small correction term [55]. This division is a key point for making DFT a useful tool for practical calculations [51]. For this reason, a non-interacting N-electron reference system is invoked. The Hamiltonian, then, can be expressed as

$$\hat{H}_{\mathrm{S}} = -\frac{1}{2}\sum_{i=1}^{N}\nabla_i^2 + \sum_{i=1}^{N} V_{\mathrm{S}}(\mathbf{r}_i), \tag{2.15}$$

in which there are no electron-electron repulsion terms. Such system has an exact eigenfunction that is a single Slater determinant constructed from the N lowest eigenstates of the one-electron equations

$$\left[-\frac{1}{2}\nabla^2 + V_{\mathrm{S}}(\mathbf{r})\right]\psi_i(\mathbf{x}) = \varepsilon_i\psi_i(\mathbf{x}). \tag{2.16}$$

The corresponding EL equation is

$$\mu = \frac{\delta T_{\mathrm{S}}[n]}{\delta n(\mathbf{r})} + V_{\mathrm{S}}(\mathbf{r}). \tag{2.17}$$

For this system, the kinetic energy and electron density are exactly expressed by

$$T_{\mathrm{S}}[n] = -\frac{1}{2}\sum_{i=1}^{N}\langle\psi_i|\,\nabla^2\,|\psi_i\rangle\,, \tag{2.18}$$

$$n(\mathbf{r}) = \sum_{i=1}^{N}|\psi_i(\mathbf{x})|^2, \tag{2.19}$$

whereas the total energy is given in the form of

$$E_{\mathrm{S}}[n] = T_{\mathrm{S}}[n] + \int n(\mathbf{r})V_{\mathrm{S}}(\mathbf{r})d^3r. \tag{2.20}$$

The quantity $T_{\mathrm{S}}[n]$ does not correspond to the true kinetic energy functional $T[n]$ from (2.9), though it is tempting to assume so. Kohn and Sham reformulated the interaction problem in such a way that its kinetic term is defined to be $T_{\mathrm{S}}[n]$ with (2.9) rearranged to give

$$E[n] = T_{\mathrm{S}}[n] + J[n] + \int n(\mathbf{r})V(\mathbf{r})d^3r + E_{\mathrm{XC}}[n], \tag{2.21}$$

where $E_{\mathrm{XC}}[n]$ is the exchange-correlation energy, containing the non-classical electron-electron repulsion and the difference between the exact and non-interacting kinetic energy[8]

$$E_{\mathrm{XC}}[n] = (U[n] - J[n]) + (T[n] - T_{\mathrm{S}}[n]). \tag{2.22}$$

Now, the EL equation becomes

$$\mu = \frac{\delta T_{\mathrm{S}}[n]}{\delta n(\mathbf{r})} + V_{\text{eff.}}(\mathbf{r}), \tag{2.23}$$

where the KS effective potential, $V_{\text{eff.}}(\mathbf{r})$, is defined by

$$V_{\text{eff.}}(\mathbf{r}) = V(\mathbf{r}) + \int \frac{n(\mathbf{r}')}{|\mathbf{r} - \mathbf{r}'|} d^3r' + V_{\mathrm{XC}}(\mathbf{r}) \tag{2.24}$$

with the exchange-correlation potential

$$V_{\mathrm{XC}}(\mathbf{r}) = \frac{\delta E_{\mathrm{XC}}[n]}{\delta n(\mathbf{r})}. \tag{2.25}$$

Note that (2.23) is precisely the same equation as the one for non-interacting electrons moving in the external potential $V_{\mathrm{S}}(\mathbf{r}) = V_{\text{eff.}}(\mathbf{r})$. Thus, for a given exact $V_{\text{eff.}}(\mathbf{r})$, one obtains $n(\mathbf{r})$ of the original many-electron system simply by solving the N one-electron equations[9]

$$\left[-\frac{1}{2}\nabla^2 + V_{\text{eff.}}(\mathbf{r})\right] \psi_i(\mathbf{x}) = \varepsilon_i \psi_i(\mathbf{x}), \tag{2.26}$$

since $n(\mathbf{r}) = n_{\text{eff.}}(\mathbf{r})$. Having in mind that $V_{\text{eff.}}(\mathbf{r})$ depends on $n(\mathbf{r})$ via (2.25), equations (2.19), (2.24), and (2.26) must be solved iteratively. One starts with an initial guess for $n(\mathbf{r})$, typically by using a superposition of atomic densities

---

[8] Term $(T[n] - T_{\mathrm{S}}[n])$ can be considered as the kinetic correlation energy [55]. For most atomic and molecular systems, it can reach a few electronvolts — the order of magnitude of the Coulomb correlation energy [59], which is defined as the difference between the exact and the Hartree-Fock energy obtained in a complete basis set [52].

[9] The solutions of (2.26) are doubly degenerate; namely, for each eigenvalue ε_i, there are two independent solutions sharing the same spatial part. They can be chosen as $\varphi_i(\mathbf{r}, \alpha)$ and $\varphi_i(\mathbf{r}, \beta)$. In the case of an even number of electrons, the α-spin density is equal to the β-spin density giving $n(\mathbf{r}) = 2n_\alpha(\mathbf{r}) = 2n_\beta(\mathbf{r}) = \sum_{i=1}^{N/2} \sum_{s=\alpha,\beta} |\varphi_i(\mathbf{r}, s)|^2$. This prescription of the spatial parts of orbitals coincides with that of the restricted Hartree-Fock (HF) method. However, the KS and HF cases differ in nature, since the restriction on spatial orbitals in the KS equations is the natural consequence of the theory, while the restriction in the restricted HF method is a further qualification on the determinantal-wavefunction approximation [59].

[60], then constructs $V_{\text{eff.}}(\mathbf{r})$ from (2.24) and solves the KS equations (2.26) for $\psi(\mathbf{x})$. From these one calculates a new electron density and repeats the procedure until the density and exchange-correlation energy have converged to within some tolerance. The KS orbitals $\psi(\mathbf{x})$ can be evaluated numerically or they can be expressed in terms of a set of atomic basis functions. In the case of the latter, solving the KS equations amounts to finding the coefficients in an atomic basis set expansion [60].

From all above, we can conclude that within the KS framework the intractable many-body problem of interacting electrons in a static external potential is reduced to a tractable problem of non-interacting electrons moving in an effective potential [52]. The connection between these two systems is that they are defined to have exactly the same ground-state electron density and energy. The complexity of the many-electron problem is now contained in the unknown exchange-correlation potential $V_{\text{XC}}(\mathbf{r})$ [51].

It is interesting to note that Hartree-Fock (HF) [61,62] and KS theories[10] provide one-electron equations for describing many-electron systems [59]. However, the KS theory, exact in principle, is different from the HF theory in its availability to fully incorporate the exchange-correlation effects of electrons. In HF theory, approximate by definition, electron correlation effects are missing and their incorporation is by no means an easy task. One should also remember that DFT optimizes an electron density, whereas HF theory optimizes a wavefunction. So, in order to determine a particular physical property using DFT, we need to know how that property depends on the density, while to determine the same property using a wavefunction, we need to know the correct quantum-mechanical operator [52]. Besides, HF theory is variational, providing an upper bound to the true energy, whilst DFT is only variational if the exact functional is applied. Formally, the KS orbitals are pure mathematical constructs used for representing the density; they are not, as in HF theory, an approximation of the wavefunction. Nevertheless, the shapes of KS orbitals tend to be remarkably similar to the ones found from the HF equations and they can be quite useful in qualitative analysis of chemical

---

[10] At this point, the reader should be familiar with the HF theory. If not, see Appendix A for a brief introduction.

properties [63]. Even more so because DFT is able to correctly reproduce the Fermi energy [51]. Having in mind that KS orbitals are consistent with the exact ground-state density and are associated with the effective potential which includes all non-classical effects, it can even be argued that HF orbitals are in a sense much farther away from the real system, since they neither reflect correlation effects nor do they yield the exact density [56].

The KS equations are open for improvement with each successive better approximation for $E_{\mathrm{XC}}[n]$ and, importantly, would give the exact results if $E_{\mathrm{XC}}[n]$ was known exactly. It is thus no wonder that finding the improved exchange-correlation functionals is the focus of much modern research. However, surprisingly enough, even the simplest possible model, known as the local density approximation (LDA), has proven to be very successful, especially in the field of condensed matter physics.

2.3 Local Density Approximation

Since there is no systematic way to find an exact density functional, at the centre of the LDA framework lies the idea of a uniform electron gas (jellium). A model proposed by Thomas [64] and Fermi [65] suggests that due to a large number of electrons N the system of volume V can be treated using quantum-statistical arguments. In such a hypothetical system, the electrons move in a uniformly distributed positive charge sufficient to retain electroneutrality. The uniform electron gas is then defined as the limit $N \to \infty$, $V \to \infty$, with the density, $n = \frac{N}{V}$, remaining finite. The Thomas-Fermi (TF) kinetic energy functional for the non-interacting uniform electron gas has the form

$$T_{\mathrm{TF}}[n] = \frac{3}{10}(3\pi^2)^{\frac{2}{3}} \int n^{\frac{5}{3}}(\mathbf{r}) d^3r. \tag{2.27}$$

If this expression is combined with the classical electrostatic energies of electron-nucleus attraction and electron-electron repulsion (neglecting exchange and correlation terms), we get an energy formula for an atom in terms of electron density alone:

$$E_{\mathrm{TF}}[n] = \frac{3}{10}(3\pi^2)^{\frac{2}{3}} \int n^{\frac{5}{3}}(\mathbf{r})d^3r - Z\int \frac{n(\mathbf{r})}{\mathbf{r}}d^3r + \frac{1}{2}\int\int \frac{n(\mathbf{r})n(\mathbf{r}')}{|\mathbf{r}-\mathbf{r}'|}d^3rd^3r'. \quad (2.28)$$

Historically, this can considered as the first example allowing to map a density $n(\mathbf{r})$ onto an energy $E[n]$ without any additional information required. It is interesting to note that TF model was introduced before the HK theorems were formulated, thus at that time it was unknown whether expressing the energy as a density functional is physically justified [52]. The HK theorems revealed that TF model may be regarded as an approximation to an exact DFT [59]. A reasonable next step in improving (2.28) would be an inclusion of at least the exchange term of the energy. An expression for the exchange energy of the uniform electron gas was given by Dirac [66]:

$$E_{\mathrm{X}}^{\mathrm{D}}[n] = -\frac{3}{4}\left(\frac{3}{\pi}\right)^{\frac{1}{3}} \int n^{\frac{4}{3}}(\mathbf{r})d^3r. \quad (2.29)$$

Now, within Thomas-Fermi-Dirac framework, the total energy of the electronic system can be written as

$$E_{\mathrm{TFD}}[n] = \frac{3}{10}(3\pi^2)^{\frac{2}{3}} \int n^{\frac{5}{3}}(\mathbf{r})d^3r + \int n(\mathbf{r})V(\mathbf{r})d^3r + J[n] - \frac{3}{4}\left(\frac{3}{\pi}\right)^{\frac{1}{3}} \int n^{\frac{4}{3}}(\mathbf{r})d^3r. \quad (2.30)$$

Although these models are nicely simple due to the direct dependence on electron density, there are seemingly invincible difficulties in going beyond the crude level of this sort of approximation [59]. One of the most serious defects is the lack of bonding, which means that molecules and solids cannot be formed in TF models. Besides, the calculated total energies of real systems are typically in error by 15–50% mostly due to the poor representation of kinetic energy [55]. The introduction of KS equations (2.26) has effectively solved this issue allowing to evaluate the kinetic energy to good accuracy and leaving only a small residual correction that should be handled separately. The price of this gain is that there are now N equations to be solved as opposed to only one equation for the total density derived from the direct approximation of the TF type [59]. Despite that, within KS formalism the uniform electron gas approach can be solely used for the unknown part of the energy functional, i.e., $E_{\mathrm{XC}}[n]$.

In the DFT framework, it is customary to separate $E_{\mathrm{XC}}[n]$ into two parts, a pure exchange, $E_{\mathrm{X}}[n]$, and a correlation contribution, $E_{\mathrm{C}}[n]$. Each of these energies is often written in terms of the energy density per particle, $\varepsilon_{\mathrm{X}}(n)$ and $\varepsilon_{\mathrm{C}}(n)$. For LDA, the corresponding relation:

$$E_{\mathrm{XC}}^{\mathrm{LDA}}[n] = E_{\mathrm{X}}^{\mathrm{LDA}}[n] + E_{\mathrm{C}}^{\mathrm{LDA}}[n] = \int n(\mathbf{r}) \left[\varepsilon_{\mathrm{X}}^{\mathrm{LDA}}(n) + \varepsilon_{\mathrm{C}}^{\mathrm{LDA}}(n)\right] d^3r = \int n(\mathbf{r}) \varepsilon_{\mathrm{XC}}^{\mathrm{LDA}}(n) d^3r, \quad (2.31)$$

where $\varepsilon_{\mathrm{XC}}^{\mathrm{LDA}}(n)$ indicates the exchange-correlation energy density per particle of a uniform electron gas of density $n(\mathbf{r})$. The exchange-correlation potential (2.25) now becomes

$$V_{\mathrm{XC}}^{\mathrm{LDA}}(\mathbf{r}) = \frac{\delta E_{\mathrm{XC}}^{\mathrm{LDA}}[n]}{\delta n(\mathbf{r})} = \varepsilon_{\mathrm{XC}}^{\mathrm{LDA}}(n) + n(\mathbf{r}) \frac{\delta \varepsilon_{\mathrm{XC}}^{\mathrm{LDA}}(n)}{\delta n(\mathbf{r})}, \quad (2.32)$$

and the KS equations (2.26) are expressed

$$\left[-\frac{1}{2}\nabla^2 + V(\mathbf{r}) + \int \frac{n(\mathbf{r}')}{|\mathbf{r} - \mathbf{r}'|} d^3r' + V_{\mathrm{XC}}^{\mathrm{LDA}}(\mathbf{r})\right] \psi_i(\mathbf{x}) = \varepsilon_i \psi_i(\mathbf{x}). \quad (2.33)$$

The exchange part of LDA is already known,[11] since it is given by the Dirac expression (2.29):

$$\varepsilon_{\mathrm{X}}^{\mathrm{D}}(n) = -\frac{3}{4} \left[\frac{3}{\pi}\, n(\mathbf{r})\right]^{\frac{1}{3}}. \quad (2.34)$$

If we insert it into (2.32), the exchange contribution to the potential becomes

$$V_{\mathrm{X}}^{\mathrm{D}}(\mathbf{r}) = -\left[\frac{3}{\pi}\, n(\mathbf{r})\right]^{\frac{1}{3}}. \quad (2.35)$$

For the correlation part, situation is more complicated because the exact form of $E_{\mathrm{C}}[n]$ is unknown even for the simple model of homogeneous electron gas. However, the extensive Monte Carlo simulations performed by Ceperley and Alder [67] have provided values of $\varepsilon_{\mathrm{C}}(n)$ over a wide range of densities. In order to use these results in DFT calculations, a suitable analytic interpolation formula must

---

[11] Here and hereafter, we are dealing with the spin-compensated case, $n_\alpha(\mathbf{r}) = n_\beta(\mathbf{r})$.

be available. This has been constructed by Vosko, Wilk, and Nusair (VWN) [68] and is generally considered to be a very accurate fit [55]. By taking into account that Wigner-Seitz (WS) radius

$$r_{\mathrm{s}}(\mathbf{r}) = \left[\frac{3}{4\pi n(\mathbf{r})}\right]^{\frac{1}{3}} \tag{2.36}$$

defines a sphere whose volume is the effective volume of an electron, the correlation energy density takes the form:[12]

$$\begin{aligned}\varepsilon_{\mathrm{C}}^{\mathrm{VWN}}(r_{\mathrm{s}}) = \frac{A}{2}\Bigg(& \ln\frac{x}{X(x)} + \frac{2b}{Q}\tan^{-1}\frac{Q}{2x+b} \\ & - \frac{bx_0}{X(x_0)}\left[\ln\frac{(x-x_0)^2}{X(x)} + \frac{2(b+2x_0)}{Q}\tan^{-1}\frac{Q}{2x+b}\right]\Bigg),\end{aligned} \tag{2.37}$$

where $x = \sqrt{r_{\mathrm{s}}(\mathbf{r})}$ and $X(x) = x^2 + bx + c$; the numerical parameters $A = 0.0621814$, $x_0 = -0.409286$, $b = 13.072$, $c = 42.7198$, and $Q = \sqrt{(4c - b^2)} = 0.044899$. Certainly, there exist other reliable parametrizations of Ceperley and Alder data, e.g., by Perdew and Zunger [69] or by Perdew and Wang [70], but in many cases they give almost identical results[13] [52].

One should pay attention to the fact that neither nuclear nor electronic charges are homogeneously distributed in actual systems, therefore, in general, the accuracy of the uniform electron gas model is rather poor. However, within the LDA framework it is assumed that the density can be locally treated as a uniform electron gas, or equivalently, that the density is a slowly-varying function [55]. It means that application of LDA to an atom, a molecule, or a solid amounts to assuming that the exchange-correlation energy for a non-uniform system can be obtained by applying homogeneous electron gas results to infinitesimal portions of the non-uniform electron distribution, each possessing $n(\mathbf{r})d^3r$ electrons, and then summing over all space the individual contributions $n(\mathbf{r})\varepsilon_{\mathrm{XC}}^{\mathrm{LDA}}(n)d^3r$ [59]. Naturally, this scheme is much more successful for slowly-varying densities of ordi-

---

[12] Have in mind that $\varepsilon_{\mathrm{C}}^{\mathrm{VWN}}(r_{\mathrm{s}}) = \varepsilon_{\mathrm{C}}^{\mathrm{VWN}}(n)$.

[13] Notice that a standard LDA framework corresponds to the combination of exchange part from (2.34) and correlation part from (2.37) which do not include the correction of the kinetic energy ($T[n] - T_{\mathrm{S}}[n]$). This difference is ignored in many modern functionals due to empirical parameters which necessarily introduce some kinetic energy correction if they are based on the experiment [52].

nary solids[14] compared to molecular systems, where the density gradients tend to be large, or strongly correlated materials, where an independent-particle picture breaks down. Nevertheless, the LDA model usually underestimates the exchange energy by at least 10%, thereby creating errors which are larger than the whole correlation energy. The correlation energy is in turn overestimated by a factor of 2 or more [55]. Although the partial error compensation between these two functionals allows to obtain the lattice constants of solids within the accuracy of 1–5% [71], the calculated bandgaps as a rule are too small [72]. In addition, it has been observed that LDA gives the ionization energies of atoms, dissociation energies of molecules, and cohesive energies with a fair accuracy of typically 10–20% [73]. It is obvious that the improvements over the LDA scheme have to consider a non-uniform electron gas — a spatially varying density and information on the rate of this variation.

2.4 Generalized Gradient Approximation

The improvements over LDA can be made by adding terms which depend not only on the density itself, but also on its derivatives. At first, a non-uniform electron gas was considered by performing a Taylor-like expansion of the density with LDA being the first term of it [55]. It was expected to obtain better approximations of the exchange-correlation functionals by extending the series with the next lowest term. In practice, however, the straightforward inclusion of low-order gradient corrections resulted in a complete failure due to the loss of several important features[15] fulfilled by LDA. Unluckily, higher-order corrections are exceedingly difficult to calculate, and little is known about them [52].

A major breakthrough has been achieved when it was realized that instead of power-series-like systematic gradient expansions one could experiment with more general functions of $n(\mathbf{r})$ and $\nabla n(\mathbf{r})$ satisfying exact theoretical constraints. If functional of the form

$$E_{\mathrm{XC}}^{\mathrm{LDA}}[n] = \int f(n) d^3 r \tag{2.38}$$

---

[14] Especially metallic solids with delocalized electrons that most closely resemble the uniform electron gas [52].

[15] The key properties of the exact exchange-correlation hole. See Appendix B for details.

was already recognized as LDA, then functional, written as

$$E_{\mathrm{XC}}^{\mathrm{GGA}}[n] = \int f(n, \nabla n) d^3 r, \tag{2.39}$$

has become known as generalized gradient approximation (GGA). It is interesting to note that different GGA functionals are much more different from each other compared to various parametrizations of LDA, since essentially there is only one correct expression for $\varepsilon_{\mathrm{XC}}^{\mathrm{LDA}}(n)$ and available forms of LDA are merely different ways of writing it. In the meantime, depending on the method of construction employed for obtaining $f(n, \nabla n)$ one can derive very dissimilar GGAs. For example, the semiempirical functionals are fitted to selected data from experiment or from precise *ab initio* calculations, whereas the non-empirical functionals are constructed to satisfy as many exact theoretical constraints as possible at the same time providing satisfactory numerical predictions for real systems. For a long time the most popular and reliable functional in molecular quantum chemistry was a combination of the exchange part introduced by Becke [74] and the correlation part proposed by Lee, Yang, and Parr [75] (BLYP). It is worthwhile to mention that the correlation term of semiempirical BLYP was constructed on the basis of the helium atom abandoning the uniform electron gas model.[16] In solid-state physics, the same role was played by the exchange-correlation functional suggested by Perdew, Burke, and Ernzerhof (PBE) [76]. Due to its well-tempered balance between computational efficiency, numerical accuracy, and reliability [77], this non-empirical functional requires a more detailed consideration.

Following the notation of (2.31), the GGA form for the exchange energy is simply

$$E_{\mathrm{X}}^{\mathrm{GGA}}[n] = \int n(\mathbf{r}) \varepsilon_{\mathrm{X}}^{\mathrm{LDA}}(n) F_{\mathrm{X}}^{\mathrm{GGA}}(s) d^3 r, \tag{2.40}$$

in which

$$s(\mathbf{r}) = \frac{|\nabla n(\mathbf{r})|}{2 k_{\mathrm{F}}(\mathbf{r}) n(\mathbf{r})} \tag{2.41}$$

---

[16] Functionals with as many as 21 fit parameters, violating some of the most basic exact constraints, are especially popular in chemistry [53].

is the dimensionless reduced density gradient,

$$k_{\mathrm{F}}(\mathbf{r}) = [3\pi^2 n(\mathbf{r})]^{\frac{1}{3}} \tag{2.42}$$

denotes a Fermi wavevector, and $F_{\mathrm{X}}^{\mathrm{GGA}}(s)$ is the exchange enhancement factor. For PBE, the exchange functional

$$E_{\mathrm{X}}^{\mathrm{PBE}}[n] = \int n(\mathbf{r})\varepsilon_{\mathrm{X}}^{\mathrm{LDA}}(n)F_{\mathrm{X}}^{\mathrm{PBE}}(s)d^3r \tag{2.43}$$

is expressed through the enhancement factor of the form:

$$F_{\mathrm{X}}^{\mathrm{PBE}}(s) = 1 + \kappa\left[1 - \frac{1}{1 + \frac{\mu}{\kappa}s^2(\mathbf{r})}\right]. \tag{2.44}$$

The parameter κ, which controls the behaviour at $s \to \infty$, is set to 0.8041 according to the relation

$$\kappa = \frac{\lambda_{\mathrm{LO}}}{2^{\frac{1}{3}}} - 1 \tag{2.45}$$

to ensure the Lieb-Oxford (LO) bound [78], which is an upper limit on the ratio of the exact exchange-correlation energy to the value of the LDA approximation of the exchange energy ($E_{\mathrm{X}}[n] \geq E_{\mathrm{XC}}[n] \geq \lambda_{\mathrm{LO}}E_{\mathrm{X}}^{\mathrm{LDA}}[n]$ with $\lambda_{\mathrm{LO}} = 2.273$). The parameter μ, which determines the behaviour for $s \to 0$, is set to 0.2195 to satisfy the LDA jellium response — a complete cancellation between beyond-LDA exchange and correlation contributions as $s \to 0$.

The PBE correlation functional is written as

$$E_{\mathrm{C}}^{\mathrm{PBE}}[n] = \int n(\mathbf{r})[\varepsilon_{\mathrm{C}}^{\mathrm{LDA}}(r_{\mathrm{s}}) + H(r_{\mathrm{s}}, t)]d^3r, \tag{2.46}$$

where $r_{\mathrm{s}}(\mathbf{r})$ is the WS radius (2.36),

$$t(\mathbf{r}) = \frac{|\nabla n(\mathbf{r})|}{2k_{\mathrm{TF}}(\mathbf{r})n(\mathbf{r})} \tag{2.47}$$

stands for appropriate reduced density gradient,

$$k_{\mathrm{TF}}(\mathbf{r}) = \sqrt{\frac{4k_{\mathrm{F}}(\mathbf{r})}{\pi}} \tag{2.48}$$

is a TF screening wavevector, and $H(r_\mathrm{s}, t)$ is given by

$$H(r_\mathrm{s}, t) = \gamma \ln \left(1 + \frac{\beta}{\gamma} t^2(\mathbf{r}) \left[\frac{1 + At^2(\mathbf{r})}{1 + At^2(\mathbf{r}) + A^2 t^4(\mathbf{r})}\right]\right) \tag{2.49}$$

with

$$A = \left[\frac{\beta}{\gamma}\right] \left(\exp\left[-\frac{\varepsilon_\mathrm{C}^\mathrm{LDA}(r_\mathrm{s})}{\gamma}\right] - 1\right)^{-1}. \tag{2.50}$$

The numerical coefficients were set to $\gamma = 0.031091$ and $\beta = 0.066725$. The value of the latter was taken from the second-order term in gradient expansion of the slowly-varying high densities [79]. Indeed, in the slowly-varying limit, $t \to 0$, the correlation functional reduces to

$$E_\mathrm{C}^\mathrm{PBE}[n] = \int n(\mathbf{r})[\varepsilon_\mathrm{C}^\mathrm{LDA}(r_\mathrm{s}) + \beta t^2(\mathbf{r}) + \ldots] d^3r = E_\mathrm{C}^\mathrm{LDA}[n] + \int n(\mathbf{r})[\beta t^2(\mathbf{r}) + \ldots] d^3r. \tag{2.51}$$

While constructing the PBE functional, it was believed that for small density variations around the uniform density, LDA is an excellent approximation to the exchange-correlation energy, while gradient expansion is not [76]. As $s \to 0$, the exchange energy becomes

$$\begin{aligned} E_\mathrm{X}^\mathrm{PBE}[n] = \int n(\mathbf{r})\varepsilon_\mathrm{X}^\mathrm{LDA}(r_\mathrm{s})[1 + \mu s^2(\mathbf{r}) + \ldots] d^3r = \\ E_\mathrm{X}^\mathrm{LDA}[n] + \int n(\mathbf{r})\varepsilon_\mathrm{X}^\mathrm{LDA}(r_\mathrm{s})[\mu s^2(\mathbf{r}) + \ldots] d^3r, \end{aligned} \tag{2.52}$$

therefore in order for the beyond-LDA terms to cancel each other, μ must satisfy the following condition:

$$\mu = \frac{\pi^2}{3}\beta. \tag{2.53}$$

Later, it was showed [77,80] that obtaining the accurate exchange energy of neutral atoms requires $\mu \approx 0.2469$, which is a close value to the one used in the PBE functional. This is a nice feature of PBE, since the accurate exchange energies of atoms are vital to dissociation energies in molecules and cohesive energies in solids. And indeed, various calculations reveal that PBE considerably improves the total energies of atoms and atomization energies of molecules compared to LDA. Another good property of PBE is that it performs equally well for finite and infinite systems [81]. However, concerning the solid-state calculations, it was noticed that PBE, as well as other popular GGAs, systematically overestimates the experimental lattice constants[17] on average by 1–5% [71]. The same amount of discrepancy produced by LDA[18] indicates the need of more reliable tool for evaluating equilibrium properties of solids. This issue is of great importance, since many inherent material properties including phonon frequencies, elastic constants, ferromagnetism, ferroelectricity, and the possibility of structural phase transitions are critically volume dependent, thus highly accurate lattice parameters are indispensable for these features [85]. What is more, PBE seriously fails for the exchange-correlation component of the jellium surface energy, while LDA performs surprisingly well in that case. A detailed analysis [86, 87] reveals that LDA once again benefits from a large error compensation, whereas in PBE this delicate balance between exchange and correlation is not valid anymore, although exchange and correlation components of the surface energy are separately improved. Unfortunately, the shift from LDA to PBE framework does not show any appreciable improvement towards the bandgap problem which still remains too small.

On the whole, the introduction of GGA has quantitatively and even qualitatively[19] ameliorated the ground-state calculations for molecules and solids. However, there remain some cases, e.g., the electronic Wigner crystal or a long-range van der Waals attraction between non-overlapped electron densities, in which the starting point of an electron gas of slowly-varying density is fundamentally incorrect meaning that LDA and GGA are completely inadequate [73]. On the other hand, this should not be very surprising, since GGA, not to mention LDA, is a

---

[17] There are classes of solids for which PBE gives a very good agreement with experiment, e.g., solids containing $3d$ transition elements [82]. Interestingly, there are some cases in which LDA is the best, while PBE performs rather poorly, e.g., MgO. Having in mind that MgO possesses a bandgap of 7.8 eV [83], LDA is based on the uniform electron gas model, and usually the periodic valence-electron density in a simple metal has some resemblance to the uniform density, this result becomes quite surprising. Moreover, the fact that PBE reduces to LDA for slowly-varying and uniform electron densities is apparently not reflected. This suggests that success of LDA lies in the strongly pronounced error compensation between the exchange and correlation functionals that has only partially been preserved by common GGAs [84].

[18] LDA usually underestimates lattice constants by about the same amount PBE tends to overestimate them.

[19] A good example is a correct ferromagnetic ground state for the body-centred cubic Fe which LDA does not reproduce [51].

very restrictive form and it is even possible to show that it cannot be exact, in general, for either exchange or correlation [53]. Although the developers of DFT are not aware of a systematic series of approximations that would finally converge to the exact form of the exchange-correlation functional, a next natural step in improving DFT is an inclusion of not only electron density and its derivatives but also the kinetic energy density. Thus, the exchange-correlation functional of the form

$$E_{\mathrm{XC}}^{\mathrm{mGGA}}[n] = \int f(n, \nabla n, \nabla^2 n, \tau) d^3 r, \tag{2.54}$$

is known as the meta-GGA (mGGA). The kinetic energy density $\tau(\mathbf{r})$ involves derivatives of the occupied KS orbitals:

$$\tau(\mathbf{r}) = \frac{1}{2} \sum_{i=1}^{\mathrm{occ.}} \sum_{s=\alpha,\beta} |\nabla \psi_i(\mathbf{r}, s)|^2. \tag{2.55}$$

The integrated $\tau(\mathbf{r})$ is equivalent to the usual non-interacting kinetic energy (2.18):

$$T_{\mathrm{S}}[n] = \int \tau(\mathbf{r}) d^3 r. \tag{2.56}$$

Meta-GGAs strive to improve upon the GGA by employing the kinetic energy density as an indicator of one-electron regions of $n(\mathbf{r})$ and forcing the correlation energy density to vanish here [88]. The presence of $\tau(\mathbf{r})$ also enables one to reproduce gradient expansions of exchange and correlation energies for slowly-varying densities through higher orders in ∇ than is possible in the GGA.

One of the most accurate non-empirical meta-GGAs for exchange and correlation was suggested by Tao, Perdew, Staroverov, and Scuseria (TPSS) [89]. It adds several more exact constraints to those satisfied by PBE and utilizes only $\tau(\mathbf{r})$ without any $\nabla^2 n(\mathbf{r})$ terms. Thus, LDA together with non-empirical PBE and TPSS can be treated as universal functionals based upon the exact constraints and limits. Extensive molecular tests [90] have revealed an impressive increase in accuracy in the order of LDA $<$ PBE $<$ TPSS for atomization energies and a more moderate improvement for vibrational frequencies and hydrogen-bond properties. For other features, the order is generally LDA $<$ PBE $\approx$ TPSS. Concerning the solid-state calculations, PBE is a significant improvement over LDA for most bulk properties, but the progress from PBE to TPSS appears to be medium, especially for bulk moduli and cohesive energies [88]. Although it seems that meta-GGAs are capable to substantially improve the surface energies, predicting lattice constants more accurately still remains a tough issue, apparently demonstrated in a study of 60 solids [82]. By taking into consideration the fact that meta-GGA calculations are more computationally challenging compared to GGA and, what is worse, they are not yet available in many solid-state codes, one should look for another way to increase the desired accuracy.

One of the simplest and most effective solutions is to make a revision to the universal PBE functional. As was noticed by Perdew and co-workers [77], at the GGA level, it is impossible to perform well for certain pairs of properties, e.g., both for molecular atomization energies and for lattice constants of solids. Due to a limited form of GGA, one has to choose. Early attempts to refine the original PBE are known as revPBE [91] with empirical $\kappa = 1.245$ and RPBE [92] with exchange enhancement factor

$$F_{\mathrm{X}}^{\mathrm{RPBE}}(s) = 1 + \kappa \left(1 - \frac{1}{\exp\left[\frac{\mu}{\kappa} s^2(\mathbf{r})\right]} \right). \tag{2.57}$$

These functionals give better energies for atoms and molecules, but at the same time worsen the lattice constants of solids. The functionals specifically designed for solids were still to come.

2.5 Revised Functionals for Solids

The gradient expansion of the exchange-correlation energy includes the inhomogeneity corrections to the homogeneous electron gas model in a systematic fashion. Thus, any GGA that recovers the uniform gas limit can be expressed as [77]

$$F_{\mathrm{X}}^{\mathrm{GGA}}(s) = 1 + \mu s^2(\mathbf{r}) + \dots \ (s \to 0), \tag{2.58}$$

where the gradient expansion that is precise for slowly-varying electron gases has [93]

$$\mu_{\mathrm{GE}} = \frac{10}{81} \approx 0.1235. \tag{2.59}$$

Despite that, the gradient expansion coefficient μ of the popular GGAs was set to $\mu \approx 2\mu_{\mathrm{GE}}$ to obtain good atomic and atomization energies resulting in good thermochemistry, where enthalpies of formation are traditionally calculated via atomization energies [85]. The larger value of μ is needed to produce the correct asymptotic expansion of the exchange energy for a neutral atom of large atomic number Z [77,80]. For PBE, its value $\mu_{\mathrm{PBE}} = 0.2195$ was found from different non-empirical argument, namely, the LDA jellium response. However, non-molecular solids and their surfaces have important valence regions over which the density variation is so slow (with reduced density gradient $0 \lesssim s(\mathbf{r}) \lesssim 1$) that the exchange energy can be described by the second-order gradient expansion [85]. This suggests that recovery of the second-order gradient expansion over this range of $s(\mathbf{r})$ is a relevant constraint on a GGA for exchange in solids.[20] The following idea was realized in the PBEsol [77] exchange-correlation functional by retaining the same analytical form of PBE. The authors have modified two parameters: $\mu_{\mathrm{PBE}} = 0.2195 \rightarrow \mu_{\mathrm{PBEsol}} = \frac{10}{81} \approx 0.1235$ in exchange part and $\beta_{\mathrm{PBE}} = 0.0667 \rightarrow \beta_{\mathrm{PBEsol}} = 0.046$ in correlation part. The value of the latter was chosen in order to reproduce the accurate TPSS values of the exchange-correlation energy for a jellium surface. Note that this choice of β_{PBEsol} violates both the gradient expansion of correlation and the PBE choice of cancelling the second-order terms in the gradient expansion for exchange and correlation, which requires[21] [94]

$$\beta = 3\frac{\mu_{\mathrm{GE}}}{\pi^2} \approx 0.0375. \tag{2.60}$$

Being accurate for both surface exchange and exchange-correlation energies, PBEsol minimizes the reliance on error cancellation between exchange and correlation. Besides, PBEsol becomes exact for solids under intense compression, where real solids and their surfaces become truly slowly varying, and exchange dominates over correlation [80]. On the other hand, PBEsol shares the limitations common for all GGA functionals.

---

[20] Although a similar constraint is not so relevant for correlation [77].

[21] However, the violation of the gradient expansion for correlation in favour of good surface energies allows to have the disposition of $\beta_{\mathrm{PBEsol}} = 0.046$ which is considerably closer to the value of the jellium response requirement (0.0375) than that demanded by complete restoration of the gradient expansion (0.0667).

Calculations carried out using PBEsol functional show improved geometry predictions compared to PBE for various types of solids [77,82,84,85,95,96] including $4d$ and $5d$ transition metals.[22] Nevertheless, PBE still performs better for the alkaline-earth metals like Ca, Sr, and Ba (for which TPSS is also a very good choice) and most of the solid-state materials containing $3d$ transition elements.[23] Naturally, PBEsol performs badly for the thermochemistry of molecules and solids [85,94,95] for which a value of $\mu \approx 2\mu_{\mathrm{GE}}$ is more appropriate. Despite that, there are some cases (e.g., alkali metals and alkali halides) where PBEsol cohesive energies are excellent and much better than PBE [85]. It is also interesting to note that PBEsol outperforms PBE by correctly predicting the energy differences between isomers and hydrocarbons, while most of the GGAs and even meta-GGAs fail for this long-standing problem [85,97]. The considerable success achieved while evaluating the structural, electronic, and phonon properties of the cubic and tetragonal phases of perovskite-type $\mathrm{SrTiO_3}$ and $\mathrm{BaTiO_3}$ [98] is also encouraging. All these results suggest that restoring the gradient expansion for exchange over a wide range of reduced density gradients might not be necessary to obtain good lattice constants and bulk moduli for a limited class of materials, but for typical non-molecular solids it acts as an essential improvement. By taking into consideration that most of the non-empirical meta-GGAs exhibit excellent description of total atomic, molecular atomization, and jellium surface energies, the implementation of PBEsol-like condition could provide even more flexible and reliable computational tool than PBEsol.[24]

Later, it was realized that the step that led from PBE to PBEsol is not unique, and allows several variations [84]. In fact, PBE and PBEsol turned out to be just two particular members of a family of functionals each of which takes its parameters, β and μ, from different constraints. The resulting two-parameter fam-

---

[22] LDA yields even better agreement with the experiment for the $5d$ transition metals like Ir, Pt, and Au. However, PBEsol demonstrates an explicit improvement over PBE giving a close value to LDA [82].

[23] To be fair, for most $3d$ metals even the PBE functional gives too small lattice constants, therefore even shorter lattice constants given by PBEsol worsen the agreement [85]. These solids are bonded in part by the highly localized $3d$ orbitals to which the second-order gradient expansion of the exchange energy may not apply [96].

[24] And it actually does, since meta-GGA, named revTPSS [99], predicts the lattice constants as well as PBEsol [100]. Moreover, it produces accurate atomization energies of molecules, desorption energies of molecules from metal surfaces, and surface energies of metals [99,101].

ily of functionals, collectively denoted as PBE(β, μ), has been tested for atoms, molecules, and solids.[25] In other work [71], the authors have proposed to consider the three-parameter family of density functionals PBE(β, μ, κ) by including the modifications of the LO bound which is a fundamental property of the quantum mechanics of Coulomb-interacting systems.[26] The meaningful non-empirical combinations of these parameters are presented in Table 2.1. In one of these, PBE($\mathrm{G_c}, \mathrm{G_x}, \mathrm{LO}$), β and μ are both determined from gradient expansions, therefore guaranteeing that gradient expansion is recovered to the extent possible within the functional form of PBE. In another, PBE($\mathrm{J_s}, \mathrm{J_r}, \mathrm{LO}$), β and μ are both determined from jellium: β from the jellium surface energy, as in PBEsol, and μ from the jellium response function, as in PBE. Finally, PBE($\mathrm{J_r}, \mathrm{G_x}, \mathrm{LO}$) takes β from the jellium response function and μ from the gradient expansion of exchange. It is worth noting that functionals in which β and μ are taken from the same type of source [e.g., PBE($\mathrm{G_c}, \mathrm{G_x}, \mathrm{LO}$) and PBE($\mathrm{J_s}, \mathrm{J_r}, \mathrm{LO}$)] have the potential to benefit from error cancellation between the exchange and correlation to a larger extent than functionals that take them from different type of source (e.g., PBE and PBEsol). It also seems that PBE($\mathrm{J_s}, \mathrm{J_r}, \mathrm{LO}$) should be pretty good for simple metals, since this functional takes both of its parameters from jellium, the paradigmatic model of such metals. However, the calculations for a large set of 60 solids [71] comprising metals, semiconductors, and insulators have revealed that all changes in parameters relative to PBE produce significantly better lattice constants. In other words, the original choice of β, μ, and κ in PBE was rather unfortunate for lattice constants, as reasonable changes to any of its parameters end up improving the results. Comparing the absolute size of the change resulting from each modified parameter, it can be concluded that PBE is most sensitive to changes in μ and least sensitive to changes in κ. This is quite reasonable because a change in κ modifies the enhancement factor much more for large values

---

[25] In brief, it was found that the original PBE is the best at predicting ground-state energies of light atoms. For molecules, PBE predicts best atomization energies, whereas PBE($\mathrm{J_s}, \mathrm{J_r}$) (see Table 2.1) predicts best interatomic distances. For solids, PBEsol outperforms PBE but is itself outperformed by PBE($\mathrm{G_c}, \mathrm{G_x}$) for lattice constants and bulk moduli and by PBE($\mathrm{J_r}, \mathrm{G_x}$) for cohesive energies.

[26] In the original paper [71], the authors use notation PBE(β, μ, λ). Here, the notation PBE(β, μ, κ) is preferred because parameter κ directly appears in the expression of the exchange enhancement factor (2.44). Note that κ is simply related to λ through (2.45).

Table 2.1 Combination of the values of β, μ, and κ presented in the form of PBE(β, μ, κ). The abbreviations denote the satisfied constraints: gradient expansion of correlation ($\mathrm{G_c}$), gradient expansion of exchange ($\mathrm{G_x}$), jellium response ($\mathrm{J_r}$), jellium surface ($\mathrm{J_s}$), Lieb-Oxford bound (LO), and tighter Lieb-Oxford bound (tLO).

Functional	β	μ	κ
$\mathrm{PBE(G_c, J_r, LO)}^{\mathrm{a}}$	0.067	0.2195	0.8041
$\mathrm{PBE(J_s, G_x, LO)}^{\mathrm{b}}$	0.046	0.1235	0.8041
$\mathrm{PBE(J_s, J_r, LO)}$	0.046	0.1513	0.8041
$\mathrm{PBE(G_c, G_x, LO)}$	0.067	0.1235	0.8041
$\mathrm{PBE(J_r, G_x, LO)}$	0.038	0.1235	0.8041
$\mathrm{PBE(G_c, J_r, tLO)}$	0.067	0.2195	0.5521
$\mathrm{PBE(J_s, G_x, tLO)}$	0.046	0.1235	0.5521
$\mathrm{PBE(J_s, J_r, tLO)}$	0.046	0.1513	0.5521
$\mathrm{PBE(G_c, G_x, tLO)}$	0.067	0.1235	0.5521
$\mathrm{PBE(J_r, G_x, tLO)}$	0.038	0.1235	0.5521

[a] This combination corresponds to PBE.
[b] This combination corresponds to PBEsol.

of reduced density gradient, while a change in μ influences the enhancement factor predominantly in the low reduced density gradient region. Statistically, the best results were obtained using PBEsol, $\mathrm{PBE(J_r, G_x, LO)}$ and $\mathrm{PBE(G_c, G_x, LO)}$ functionals. This indicates that the value of β turns out to be almost irrelevant, whereas the value of μ appears to be responsible for the improved behaviour. The gradient expansion of exchange is thus seen to be the key ingredient in functionals that deliver good lattice constants. On the other hand, any modification of the original PBE which improves lattice parameters of solids significantly increases the error in the atomization energy of molecules.[27] It once again confirms the claim that at least GGAs of PBE-form cannot describe well solids and molecules simultaneously.

Regarding other approaches designed for solids, it is worthwhile to distinguish the second-order GGA (SOGGA) constructed by Zhao and Truhlar [94]. Compared to the original PBEsol, this functional satisfies the gradient expansion for exchange ($\mu_{\mathrm{SOGGA}} = \mu_{\mathrm{PBEsol}} = \frac{10}{81}$) as well as for correlation ($\beta_{\mathrm{SOGGA}} = \beta_{\mathrm{PBE}} = 0.0667$). What is more, the parameter $\kappa_{\mathrm{SOGGA}} = 0.5521$ is determined from a tighter LO bound, and the exchange enhancement factor is taken as a half-and-

---

[27] The tested set of molecules comprises $\mathrm{SiH_4}$, SiO, $\mathrm{S_2}$, $\mathrm{C_3H_4}$, $\mathrm{C_2H_2O_2}$, and $\mathrm{C_4H_8}$.

half mixing of the PBE and RPBE functionals:

$$F_{\mathrm{X}}^{\mathrm{SOGGA}}(s) = 1 + \kappa \left(1 - \frac{1}{2} \left[\frac{1}{1 + \frac{\mu}{\kappa} s^2(\mathbf{r})} \right] - \frac{1}{2} \exp\left[-\frac{\mu}{\kappa} s^2(\mathbf{r}) \right] \right). \tag{2.61}$$

Slightly different approximation was proposed by Wu and Cohen (WC) [102]. Here, the exchange enhancement factor is given by

$$F_{\mathrm{X}}^{\mathrm{WC}}(s) = 1 + \kappa \left[1 - \frac{1}{1 + \frac{x(s)}{\kappa}} \right], \tag{2.62}$$

where

$$x(s) = \frac{10}{81} s^2(\mathbf{r}) + \left(\mu - \frac{10}{81} \right) s^2(\mathbf{r}) \exp[-s^2(\mathbf{r})] + \ln[1 + c s^4(\mathbf{r})]. \tag{2.63}$$

Parameters μ and κ have the same values as in PBE, and $c = 0.0079325$ is set to recover the fourth-order parameters of the fourth-order gradient expansion of the exact exchange functional in the limit of a slowly-varying density.[28] The correlation part of WC functional, just as for SOGGA, is usually taken from the PBE functional.

A detailed investigation of the performance of the revised functionals for solids [82], namely, PBEsol, SOGGA, and WC, has revealed that concerning the lattice constants no clear winner has emerged, since all of them improve over LDA and PBE for many solids. Actually, the ordering of the functionals from the one which shows the largest underestimation to the one which shows the largest overestimation is LDA, SOGGA, PBEsol, WC, TPSS, and PBE. However, one should remember that PBE ant TPSS are equally good for both finite and infinite systems, whilst for the thermochemistry of molecules, PBEsol and SOGGA perform very poorly [94] and WC slightly deteriorates the PBE results [103].

---

[28] Unfortunately, incorrectly, since no GGA can recover the correct fourth-order gradient expansion for the exchange energy, even approximately, but a meta-GGA can (and TPSS in fact does, at least for very slowly-varying densities) [85].

2.6 Hybrid Functionals

Since the exchange contribution is usually significantly larger compared to the corresponding correlation effects, it seems to be logical to obtain the exchange values as precise as possible. The straightforward and seemingly most appropriate strategy for arriving at the most accurate exchange energy appears to be the use of the exact HF exchange expression[29] for the occupied KS orbitals instead of the approximate $E_{\mathrm{X}}^{\mathrm{DFT}}[n]$ functionals. The addition of respective correlation energy term $E_{\mathrm{C}}^{\mathrm{DFT}}[n]$ then would yield full exchange-correlation energy:

$$E_{\mathrm{XC}}[n] = E_{\mathrm{X}}^{\mathrm{HF}} + E_{\mathrm{C}}^{\mathrm{DFT}}[n]. \tag{2.64}$$

Unfortunately, in reality this strategy does not pay off. The reason for it is the incompatibility between GGA (or LDA) correlation and exact exchange. To be specific, the exact exchange hole in a real system can have a highly non-local, multicentred character which is largely cancelled by an almost equal but opposite non-local, multicentred character in the exact correlation hole. In the meantime, GGA exchange and correlation holes are localized because all properties are determined by the density and its gradient at one particular point in space. Thus, the combination of exact, delocalized exchange hole with a localized model hole for correlation forbids the cancellation between them, and the resulting total hole has the wrong characteristics [56].

But despite that, the idea appeared to have made its impact. The exchange-correlation energy in the KS scheme can be expressed in terms of the adiabatic connection[30]

$$E_{\mathrm{XC}}[n] = \int_0^1 E_{\mathrm{XC}}^{\lambda}[n] d\lambda, \tag{2.65}$$

where λ denotes the coupling strength parameter, which for the real interacting system is $\lambda = 1$ and for the non-interacting one $\lambda = 0$. The λ-dependent exchange-correlation energy $E_{\mathrm{XC}}^{\lambda}[n]$ stands for the non-classical contributions to the electron-electron interaction, and integrated over λ also incorporates the ki-

---

[29] See Appendix A and (A.5)–(A.8) therein.

[30] See Appendix C for details.

netic energy part into $E_{\mathrm{XC}}[n]$. As in the $\lambda = 0$ limit the electrons are non-interacting, there is consequently no correlation energy, only the exchange part [55]. Hence, the integral in (2.65) simply corresponds to the exchange contribution of a Slater determinant composed of the KS orbitals. The exchange energy then can be computed by applying the exact HF exchange expression. For $\lambda = 1$, the non-classical contributions are those of the fully interacting system, containing exchange as well as correlation parts. Although this interacting exchange-correlation energy is unknown, it can be more or less satisfactorily approximated by $E_{\mathrm{XC}}^{\mathrm{DFT}}[n]$ functional. Thus, the true exchange-correlation energy is given by the integral of (2.65) and we know its value for $\lambda = 0$ exactly and have a pretty good approximation for $\lambda = 1$. To exactly evaluate this integral, however, we need $E_{\mathrm{XC}}^{\lambda}[n]$ for intermediate values of λ. But this information is not available and we must try to find approximations to solve the following problem. The simplest approximation to solve (2.65) is to assume that $E_{\mathrm{XC}}^{\lambda}[n]$ is a linear function of λ. This leads to the expression proposed by Becke [104]

$$E_{\mathrm{XC}}^{\mathrm{HH}}[n] = \frac{1}{2}E_{\mathrm{XC}}^{\lambda=0}[n] + \frac{1}{2}E_{\mathrm{XC}}^{\lambda=1}[n] = \frac{1}{2}E_{\mathrm{X}}^{\mathrm{HF}} + \frac{1}{2}E_{\mathrm{XC}}^{\mathrm{DFT}}[n], \tag{2.66}$$

which is known as half-and-half (HH) mixing. From physical point of view, the non-locality of exact exchange hole plays some role in molecular bonds.[31] Since local electron gas model is physically inappropriate near the $\lambda = 0$ exchange-only limit [105] but, on the other hand, accurate DFT approaches must recognize this $\lambda = 0$ non-locality, the inclusion of certain amount of the exact exchange hole into the overall hole seems reasonable.[32] Functionals of this sort, where a certain amount of exact exchange is incorporated into their structure, are called hybrid functionals. In fact, $E_{\mathrm{XC}}^{\mathrm{HH}}[n]$ approach showed a promising performance and Becke suggested its modification [105] by introducing semiempirical coefficients to determine the weights of various components. Later, further changes proposed by Stephens and co-workers [106] turned out into one of the most popular computational tools in molecular quantum chemistry recognized as B3LYP. The B3LYP

---

[31] This effect is already observed in the simplest conceivable case, H_2 molecule.

[32] Note that we are considering only some amount of exact exchange, not all as it was suggested in (2.64).

exchange-correlation energy expression is given by

$$\begin{aligned} E_{\mathrm{XC}}^{\mathrm{B3LYP}}[n] &= E_{\mathrm{XC}}^{\mathrm{LDA}}[n] \\ &+ a(E_{\mathrm{X}}^{\mathrm{HF}} - E_{\mathrm{X}}^{\mathrm{LDA}}[n]) + b(E_{\mathrm{X}}^{\mathrm{GGA}}[n] - E_{\mathrm{X}}^{\mathrm{LDA}}[n]) + c(E_{\mathrm{C}}^{\mathrm{GGA}}[n] - E_{\mathrm{C}}^{\mathrm{LDA}}[n]), \end{aligned} \tag{2.67}$$

where parameters have values $a = 0.2$, $b = 0.72$, and $c = 0.81$. The amount of exact exchange in the functional is determined through a, while b and c control contributions of exchange and correlation gradient corrections to the LDA. The values of a, b, and c were chosen to optimally reproduce some atomization, ionization, and total energies as well as proton affinities. In B3LYP scheme, LDA corresponds to the exchange part of Dirac [66] and correlation part of Vosko, Wilk, and Nusair [68], whereas GGA stands for the Becke [74] exchange and Lee, Yang, and Parr [75] correlation. Concerning the molecular calculations, B3LYP experienced an unprecedented success due to its surprisingly good performance in many chemical applications[33] [56].

Interestingly, a fraction of exact exchange employed in B3LYP functional also seems to be reasonable from pure theoretical considerations on atomization energies [107, 108]. A parameter-free hybrid functional in which the amount of exact exchange has been derived as 25% from theoretical arguments through a perturbation theory became known as PBE0 [109]:

$$E_{\mathrm{XC}}^{\mathrm{PBE0}}[n] = E_{\mathrm{XC}}^{\mathrm{PBE}}[n] + \frac{1}{4}(E_{\mathrm{X}}^{\mathrm{HF}} - E_{\mathrm{X}}^{\mathrm{PBE}}[n]). \tag{2.68}$$

It immediately showed a promising performance for all important molecular properties along the whole periodic table, being competitive with the most reliable, empirically parameterized hybrids. However, while about 25% of exact exchange is reasonable for most typical systems, it is obvious that in general this parameter is not universal and depends on the actual situation. Besides, although based upon a valid physical insight, hybrids do not satisfy any exact constraints that their underlying DFT approaches do not satisfy.

For solids, the hybrid functionals do not constitute the standard choice because

---

[33] Especially for the calculation of geometrical and thermochemical properties.

of their inadequacy for metallic systems [110, 111] and the high computational cost that exact exchange involves [52, 81]. Nevertheless, hybrids often perform well for calculations of bandgaps [110–113] for which the use of LDA or GGA is not appropriate due to the local nature of these approximations[34] [114]. Although hybrid functionals are able to improve various solid-state properties over LDA or GGA [43, 115–117], it is very likely that the accuracy of obtained results is highly-dependent on the amount of exact exchange. Thus, for different materials one should systematically investigate the effect of modifying the exact exchange mixing parameter and try to identify the physics that stands beyond it.[35]

2.7 Self-Interaction Error

The classical electrostatic repulsion term (2.10) does not vanish for a one-electron system due to the spurious self-interaction inherent in it [118]. In HF theory, this does not lead to any problem, since all Coulomb self-interaction terms are exactly cancelled by the corresponding exchange self-interaction terms. This would neither cause any trouble in DFT scheme if the exact expression of $E_{\mathrm{XC}}[n]$ was used [51]. However, when an approximation like LDA or GGA is made, the cancellation is incomplete and the remainder, known as a self-interaction error (SIE), contributes to the energy. Of course, SIE is not limited to one-electron systems, where it can be identified most easily, but applies to all many-electron frameworks. Therefore, the interaction of each single electron with the potential generated by itself is believed to be the cause of many failures of approximate density functionals.

It is obvious that the one-electron self-interaction free exchange-correlation functionals for $E_{\mathrm{XC}}[n_\alpha, n_\beta]$ must satisfy the following conditions:

$$J[n_s] + E_{\mathrm{X}}[n_s, 0] = 0, \tag{2.69}$$

$$E_{\mathrm{C}}[n_s, 0] = 0, \tag{2.70}$$

where $n_s(\mathbf{r})$ stands for any one-electron density. The first equation expresses that

---

[34] Hybrid scheme incorporates the orbital-dependent potential.

[35] For instance, see [5].

a single electron does not interact with itself, while the second equation states that a single electron does not possess any correlation energy [53]. Unfortunately, no exchange-correlation functional at LDA, GGA, or meta-GGA level satisfies both of the conditions simultaneously[36] [118].

Although the self-interaction vanishes in the thermodynamic limit for delocalized states [119], the SIE remains particularly critical for spatially localized electronic states for molecules and crystals [52]. The delocalized electrons move fast, thus experiencing mainly the LDA mean-field potential. The localized electrons reside on each atomic site for so long that the surroundings must respond to their presence [120]. But the lack of self-interaction cancellation leads to an artificial overdelocalization of electrons [117]. For this reason, the problems of DFT approaches are most severe in systems where the electrons tend to be localized[37] and strongly interacting, e.g., strongly correlated materials. The well-known examples of such systems are the crystalline transition-metal oxides with localized d electron states[38] as well as compounds with localized f electrons. Large self-interaction also characterizes localized core states together with interface, surface, and impurity systems [119, 122].

If the SIE arose only in one-electron systems, it would be easy to apply the corresponding corrections. But the problem manifests itself in many-electron cases, therefore the SIE of a particular exchange-correlation approximation is much more difficult to quantify and correct. However, Perdew and Zunger [69] proposed a simple self-interaction correction (SIC) scheme which eliminates all spurious self-interaction terms orbital by orbital. Despite its apparent simplicity, the practical implementation of the self-interaction corrected density functional theory (SIC-DFT) is rather complicated due to the fact that the SIC-DFT equations do not share the same potential for all orbitals [51]. Instead, the SIC exchange-correlation potentials become orbital dependent, and since the KS orbitals thereby are not solutions to the same Hamiltonian, one cannot in general be sure that the orbitals are orthogonal [52].

---

[36] It is interesting to note that by construction LYP and TPSS correlation functionals satisfy (2.70), whereas VWN and PBE do not.

[37] In general, DFT approximations provide the best combination of accuracy and efficiency as long as overdelocalization effects do not poison their performance [121].

[38] To be concrete, the most prominent cases are MnO, FeO, CoO, and NiO.

The performance of SIC-DFT compared to the regular DFT might be ambivalent [118]. On one hand, SIC improves activation barriers of chemical reactions [123–125] and nuclear magnetic resonance chemical shifts [126]. On the other hand, it provides little or no improvement for reaction energies [123, 127] and results in too short bond lengths for molecules [127]. Concerning merely the solid-state calculations, a significant improvement in the description of both bulk and surface electronic properties for a variety of materials has been observed [72, 128, 129]. On the whole, SIC may affect plenty of phenomena encompassing, among others, surface reconstructions, adsorbtion and diffusion of atoms and molecules on surfaces, doping in semiconductors, alloys, homojunctions, and heterojunctions. Nevertheless, one should take into account that the discrepancies between theoretical and experimental results which are not attributable to the self-interaction should not be expected to disappear within the SIC-DFT framework [119].

In addition to the SIC-DFT scheme, there are several other methods for SIE problem ranging from conceptually straightforward DFT + U [130] to more sophisticated and computationally heavy quasiparticle Green function (GW) approach [131] or dynamical mean-field theory (DMFT) implementation [132]. It is interesting to note that the inclusion of non-local HF exchange into the hybrid functionals also efficiently cancels the self-interaction effects [133]. This gives a great improvement in the predicted electronic and magnetic properties [134–137] at a fraction of computational cost required for more complex techniques.

2.8 Strongly Correlated Systems

Correlation effects play a significant role practically in all materials [51]. The most simple example to consider is the chemical bonding of a H_2 molecule. For the two electrons involved, Heitler and London [138] suggested the following correlated ground-state wavefunction

$$\Psi(\mathbf{x}_1, \mathbf{x}_2) = \frac{1}{2}[\psi_1(\mathbf{r}_1)\psi_2(\mathbf{r}_2) + \psi_2(\mathbf{r}_1)\psi_1(\mathbf{r}_2)](\alpha_1\beta_2 - \beta_1\alpha_2), \tag{2.71}$$

where the functions $\psi_{1,2}(\mathbf{r})$ are centred on atoms 1 and 2, and the spin functions α and β denote the spin-up and spin-down states, respectively. In this case, $\Psi(\mathbf{x}_1, \mathbf{x}_2)$ does not contain ionic configurations in which both electrons are centred at one atom. It means that the mutual Coulomb repulsion of the two electrons is kept low because they are well separated. However, this is at the expense of their kinetic energy which would be lowered if the above restriction is dropped. Therefore, the implicit assumption of the Heitler-London approach is that the mutual Coulomb repulsion of the electrons is more important than their kinetic energy gain due to the delocalization. In other words, we are dealing with the strongly correlated electrons.

Quite an opposite view is taken by the molecular-orbital approximation based on the independent-electron description. Here, the antisymmetric wavefunction is given by

$$\begin{aligned}\Psi(\mathbf{x}_1, \mathbf{x}_2) = \frac{1}{\sqrt{2^3}}[&\psi_1(\mathbf{r}_1)\psi_1(\mathbf{r}_2) + \psi_2(\mathbf{r}_1)\psi_2(\mathbf{r}_2) \\ &+ \psi_1(\mathbf{r}_1)\psi_2(\mathbf{r}_2) + \psi_2(\mathbf{r}_1)\psi_1(\mathbf{r}_2)](\alpha_1\beta_2 - \beta_1\alpha_2). \qquad (2.72)\end{aligned}$$

The electrons move independently of each other and the chance to find both of them at the same atomic site, or ionic configuration, is $\frac{1}{2}$. Their kinetic energy is optimally lowered, but their Coulomb repulsion remains relatively large. Thus, (2.72) will be a reasonable description of the true wavefunction only when the kinetic energy gain due to the spreading of electrons over both atoms dominates the mutual electron repulsion [52]. This is the case of weakly correlated electrons.[39]

The same competition between the tendency towards delocalization leading to band formation and the tendency to localization leading to atomic-like behaviour is found in solids [139]. The kinetic energy gain caused by delocalization depends on how strong is the overlap of electronic wavefunctions with neighbouring atoms. Thus, *s* and *p* electrons of the valence band are less correlated in their motions than, e.g., *f* electrons of an incomplete *f* shell, since the latter are closer to the nuclei and their wavefunction overlap with the neighbouring sites is small. Besides, the relatively extended wavefunctions of *s* and *p* electrons result in a small

---

[39] In reality, a H_2 molecule is between the two limits defined by (2.71) and (2.72).

Coulomb repulsion compared to that of $4f$ electrons. In fact, $4f$ electrons are the strongest correlated valence electrons and describing then within an independent-particle approximation does not make much sense.

On the whole, strongly correlated systems with open $3d$, $4f$, and $5f$ shells have many remarkable properties and transitions between distinct, competing phases with dramatically different electronic and magnetic orders [140]. Due to the substantial Coulomb repulsion, the strongly correlated electrons, especially in metals [38], cannot be properly described as embedded in a static mean field generated by the other electrons. The influence of an electron on the others is simply too pronounced for each to be treated independently [141]. The effective one-particle model breaks down and the wavefunction of the system becomes essentially many-body-like, represented by combinations of Slater determinants [139]. For this reason, the traditional DFT approaches are not accurate enough when applied to the strongly correlated systems indicating the need for more sophisticated methods.[40]

---

[40] Like SIC-DFT or DFT + U in simpler cases and GW or DMFT for more complicated ones.

Chapter 3

Computational Details

3.1 General Parameters

The first-principles periodic calculations were carried out using CRYSTAL09 [142] code, in which the crystalline wavefunctions are expanded as a linear combination of atom-centred Gaussian orbitals (LCAO). Equilibrium atomic positions and lattice constants were obtained using analytical gradients of the total energy with respect to atomic coordinates and unit-cell parameters within the quasi-Newton algorithm. The Hessian matrix containing numerical second derivatives of the total energy was updated by means of the Broyden-Fletcher-Goldfarb-Shanno scheme [143–147]. The initial values of Hessian matrix were generated using a classical model proposed by Schlegel [148, 149]. Optimization convergence was checked on the root-mean-square (RMS) and the absolute magnitude of the largest components of both the gradients and the estimated nuclear displacements. The optimization was considered complete when these four parameters satisfied the determined thresholds which for the RMS values of gradients and displacements were set to 0.00006 and 0.00012 atomic units (a.u.), respectively. The maximum allowed gradients and displacements were 1.5 times larger. In order to improve the self-consistence field convergence, the Kohn-Sham matrix mixing technique together with modified Broyden's scheme [150] or Anderson's method [151] was applied. The default values of truncation criteria for bielectronic integrals were modified to tighter ones by setting the overlap thresholds for exchange and Coulomb integrals to 10^{-7} for orthorhombic and to 10^{-9} for tetragonal and cubic phases of $SrRuO_3$, and to 10^{-8} for rhombohedral $LaNiO_3$. Analogously, the tolerance on change in total energy was tightened to 10^{-9} a.u. for tetragonal and cubic phases, whereas for the computationally heavier orthorhombic phase the parameter was set to 10^{-7} a.u. For $LaNiO_3$, the tolerance was increased to 10^{-8} a.u. The initial amounts of asymmetric k points in the irreducible Brillouin zone used for cubic, tetragonal,

Table 3.1 Combinations of applied strains, associated space group symmetries, numbers of k points in the irreducible Brillouin zone, and coefficients of a quadratic term in the polynomial fitting of the total energy-strain curve for $SrRuO_3$.

Strain tensor ε	Initial symmetry	Symmetry under deformation	No. of k points	Coefficient of δ^2
$\begin{bmatrix}\delta&0&0\\0&0&0\\0&0&0\end{bmatrix}$	Cubic, No. 221 ($Pm\bar{3}m$) Tetr., No. 140 ($I4/mcm$) Orth., No. 62 ($Pbnm$)	Tetr., No. 123 ($P4/mmm$) Orth., No. 72 ($Ibam$) Orth., No. 62 ($Pbnm$)	196 428 125	$\frac{V_0}{2}C_{11}$
$\begin{bmatrix}0&0&0\\0&\delta&0\\0&0&0\end{bmatrix}$	Orth., No. 62 ($Pbnm$)	Orth., No. 62 ($Pbnm$)	125	$\frac{V_0}{2}C_{22}$
$\begin{bmatrix}0&0&0\\0&0&0\\0&0&\delta\end{bmatrix}$	Tetr., No. 140 ($I4/mcm$) Orth., No. 62 ($Pbnm$)	Tetr., No. 140 ($I4/mcm$) Orth., No. 62 ($Pbnm$)	244 125	$\frac{V_0}{2}C_{33}$
$\begin{bmatrix}\delta&0&0\\0&\delta&0\\0&0&0\end{bmatrix}$	Cubic, No. 221 ($Pm\bar{3}m$) Tetr., No. 140 ($I4/mcm$) Orth., No. 62 ($Pbnm$)	Tetr., No. 123 ($P4/mmm$) Tetr., No. 140 ($I4/mcm$) Orth., No. 62 ($Pbnm$)	301 244 125	$\frac{V_0}{2}(2C_{12}+C_{11}+C_{22})$
$\begin{bmatrix}\delta&0&0\\0&0&0\\0&0&\delta\end{bmatrix}$	Tetr., No. 140 ($I4/mcm$) Orth., No. 62 ($Pbnm$)	Orth., No. 72 ($Ibam$) Orth., No. 62 ($Pbnm$)	428 125	$\frac{V_0}{2}(2C_{13}+C_{11}+C_{33})$
$\begin{bmatrix}0&0&0\\0&\delta&0\\0&0&\delta\end{bmatrix}$	Orth., No. 62 ($Pbnm$)	Orth., No. 62 ($Pbnm$)	125	$\frac{V_0}{2}(2C_{23}+C_{22}+C_{33})$
$\begin{bmatrix}0&0&0\\0&0&\delta\\0&\delta&0\end{bmatrix}$	Cubic, No. 221 ($Pm\bar{3}m$) Tetr., No. 140 ($I4/mcm$) Orth., No. 62 ($Pbnm$)	Orth., No. 65 ($Cmmm$) Mon., No. 15 ($C/2c$) Mon., No. 14 ($P2_1/c$)	301 744 170	$2V_0C_{44}$
$\begin{bmatrix}0&0&\delta\\0&0&0\\\delta&0&0\end{bmatrix}$	Orth., No. 62 ($Pbnm$)	Mon., No. 14 ($P2_1/c$)	170	$2V_0C_{55}$
$\begin{bmatrix}0&\delta&0\\\delta&0&0\\0&0&0\end{bmatrix}$	Tetr., No. 140 ($I4/mcm$) Orth., No. 62 ($Pbnm$)	Orth., No. 69 ($Fmmm$) Mon., No. 14 ($P2_1/c$)	428 170	$2V_0C_{66}$

and orthorhombic $SrRuO_3$ were 84, 349, and 125, respectively. However, under $C_{\alpha\beta}$ related deformations these numbers, as well as space group symmetries of the system, have changed — see Table 3.1 for details. In case of $LaNiO_3$, the number of k points was confined to 417.

In CRYSTAL09, while numerically evaluating DFT exchange-correlation contribution, grid points are generated using Gauss-Legendre radial quadrature and Lebedev two-dimensional angular point distribution. In this study, an extra large grid was used which contains 75 radial points and 974 angular points in the most accurate integration region. Concerning the basis sets, small-core Hay-Wadt pseudopotentials [152] (PPs) corresponding to 28 core electrons ($1s^22s^22p^63s^23p^63d^{10}$) were applied for both Sr and Ru atoms. The remaining part ($4s^24p^65s^2$) of the basis set for Sr was taken from the strontium titanate study [153], whereas for Ru ($4s^24p^64d^75s^1$) it was adopted from the modified LANL2DZ basis set [154].

In order to avoid numerical problems usually caused by too diffuse valence functions overlapping with the core functions of the neighbouring atoms, the exponents smaller than 0.08 bohr^{-2} were removed. The outermost p shell exponent $\alpha_p = 0.083$ bohr^{-2} was decontracted and, together with the most external d shell exponent $\alpha_d = 0.1501$ bohr^{-2}, optimized by attempting to minimize the total energy per unit cell with the lattice constants and atomic positions fixed at experimental values. After optimization, the corresponding p and d exponents were set to 0.1301 and 0.1329 bohr^{-2}, respectively. For O, the all-electron basis set with a double set of d functions was taken from [155]. In case of LaNiO$_3$, the all-electron basis sets were applied for O as well as for Ni atoms [156], while for La atom small-core Hay-Wadt PP ($1s^2 2s^2 2p^6 3s^2 3p^6 3d^{10} 4s^2 4p^6 4d^{10}$) was combined with the remaining part ($5s^2 5p^6 5d^1 6s^2$) used in LaMnO$_3$ study [157].

We would like to remark that PBE, SOGGA, and WC exchange functionals were used with the correlation part of PBE, whereas the PBEsol exchange functional was employed with the correlation part of PBEsol and PBE. A separate notation PBEsol$^{\mathrm{PBE}}$ was introduced for the latter combination.

Our additional molecular HF study for LaNiO$_3$ was performed using DIRAC08 [158] and GAUSSIAN03 [159] computer codes. The lattice constants and tetragonally distorted structure of LaNiO$_3$ unit cell with 15 atoms were adopted from [9]. For comparison purposes, we have carried out two HF calculations employing non-relativistic (GAUSSIAN03) and 2-component relativistic (DIRAC08) Hamiltonians. The latter one is obtained after Barysz-Sadlej-Snijders transformation of the Dirac Hamiltonian in the finite basis set [160]. For relativistic calculations, we have reduced the recommended convergence criterion[1] (norm of the electronic gradient) to 10^{-5}, because we were only interested in binding energy. The relativistic all-electron double-zeta basis set for La developed with the Dirac-Coulomb Hamiltonian was taken from [161]. The non-relativistic equivalent was constructed from Hay-Wadt PP combined with the original part for the rest of electrons given therein. For Ni and O atoms, we have confined to standard 3-21G [162] and STO-2G [163] basis sets, respectively, noticeably reducing computational time.

---

[1] With the exception of this setting, the default computational parameters were used for both DIRAC08 and GAUSSIAN03.

All the calculations presented herein are non-magnetic. On one hand, $LaNiO_3$ is a paramagnetic material and $SrRuO_3$ loses its ferromagnetism above 160 K. On the other hand, the experimentally measured polycrystalline elastic parameters as well as lattice constants of tetragonal and cubic phases of $SrRuO_3$ can be solely found for the paramagnetic configuration. Therefore, the non-magnetic treatment appears to be a better choice for the direct comparison to the available experiment.

3.2 Elastic Constants

Under a linear elastic deformation, solid bodies are described by Hooke's law. In the tensorial form, it can be expressed as

$$\sigma_{ij} = \sum_{k,l=1}^{3} C_{ijkl}\varepsilon_{kl}, \tag{3.1}$$

where i, j, k, and l are the indices running from 1 to 3, σ_{ij} is the stress, ε_{kl} is the strain, and C_{ijkl} is a fourth-rank stiffness or elastic constants tensor having 81 components. In general, elastic constants describe the material's resistance against an externally applied strain. The symmetry relation $C_{ijkl} = C_{jikl} = C_{ijlk} = C_{klij}$ reduces the number of independent components to 21, which in turn can be further reduced if the material under consideration possesses its own symmetry. According to Voigt notation ($11 \to 1$, $22 \to 2$, $33 \to 3$, $23 = 32 \to 4$, $13 = 31 \to 5$, $12 = 21 \to 6$), the C_{ijkl} components can be arranged in a symmetric 6×6 matrix. Then, (3.1) can be written as [164]

$$\sigma_{\alpha} = \sum_{\beta=1}^{6} C_{\alpha\beta}\varepsilon_{\beta}, \tag{3.2}$$

where

$$\sigma_{\alpha} = \sigma_{ij}, \tag{3.3}$$

$$\varepsilon_{\beta} = \varepsilon_{kl} \text{ if } \beta = 1, 2 \text{ or } 3, \tag{3.4}$$

$$\varepsilon_{\beta} = 2\varepsilon_{kl} \text{ if } \beta = 4, 5 \text{ or } 6. \tag{3.5}$$

The relation (3.2) for the stresses expressed in the strains can be inverted to give strains in terms of the stresses

$$\varepsilon_\alpha = \sum_{\beta=1}^{6} S_{\alpha\beta}\sigma_\beta, \tag{3.6}$$

in which the compliance matrix $S_{\alpha\beta}$ is inverse to the stiffness matrix $C_{\alpha\beta}$.

The total energy of the distorted crystal's unit cell can be expressed through a Taylor series in terms of the strains

$$E(\varepsilon) = E_0 + \sum_{\alpha=1}^{6} \left.\frac{\partial E(\varepsilon)}{\partial \varepsilon_\alpha}\right|_{\varepsilon=0} \varepsilon_\alpha + \frac{1}{2}\sum_{\alpha,\beta=1}^{6} \left.\frac{\partial^2 E(\varepsilon)}{\partial \varepsilon_\alpha \partial \varepsilon_\beta}\right|_{\varepsilon=0} \varepsilon_\alpha\varepsilon_\beta + \ldots, \tag{3.7}$$

where $E_0 = E(0)$ refers to the equilibrium configuration. Having in mind the relations [165]

$$\sigma_\alpha = \frac{1}{V_0}\left.\frac{\partial E(\varepsilon)}{\partial \varepsilon_\alpha}\right|_{\varepsilon=0} \tag{3.8}$$

and

$$C_{\alpha\beta} = \frac{1}{V_0}\left.\frac{\partial^2 E(\varepsilon)}{\partial \varepsilon_\alpha \partial \varepsilon_\beta}\right|_{\varepsilon=0}, \tag{3.9}$$

(3.7) equation may be written in the form of

$$E(\varepsilon) = E_0 + V_0\sum_{\alpha=1}^{6} \sigma_\alpha\varepsilon_\alpha + \frac{V_0}{2}\sum_{\alpha,\beta=1}^{6} C_{\alpha\beta}\varepsilon_\alpha\varepsilon_\beta + \ldots, \tag{3.10}$$

where V_0 denotes the volume of the unstrained unit cell. If the crystalline structure is fully relaxed, the linear term in (3.10) is equal to zero and the second-order elastic constants can be obtained by evaluating total energy as a function of the applied strains. However, in order to remain in the linear regime, the deformation of the crystal should be sufficiently small. In this study, the magnitude of the applied strains δ was varied between -0.03 and 0.03 with a step[2] of 0.005 for 9 different deformations (see Table 3.1) that correspond to the appropriate elastic constants or their combinations. The energy-strain curve of the deformed structures (3.10) was fitted with polynomials in order to extract the coefficient of a quadratic term δ^2 which possesses the required data for the evaluation of elastic

---

[2] With several exceptions for tetragonal and orthorhombic phases of $SrRuO_3$, see Section 5.5 in Chapter 5.

constants. For a better stability, the polynomials up to order 5 were used during the fitting procedure. While computing the total energy under deformations, the internal atomic positions were allowed to relax with the deformed cell shape and volume remaining fixed.

3.3 Mechanical Stability and Macroscopic Elastic Parameters

A solid in equilibrium is mechanically stable if under arbitrary but small deformations the quadratic term in (3.10) is positive definite for all real values of strains unless the strains are zero. This determines restrictions, expressed in the form of inequalities, for the elastic constants [164]. For the cubic, tetragonal, and orthorhombic crystalline structures the necessary conditions for the mechanical stability are given by [166]:

$$C_{11} > 0,\ C_{44} > 0,\ (C_{11} - C_{12}) > 0,\ (C_{11} + 2C_{12}) > 0; \tag{3.11}$$

$$\begin{gathered} C_{11} > 0,\ C_{33} > 0,\ C_{44} > 0,\ C_{66} > 0, \\ (C_{11} - C_{12}) > 0,\ (C_{11} + C_{33} - 2C_{13}) > 0,\ (2C_{11} + C_{33} + 2C_{12} + 4C_{13}) > 0; \end{gathered} \tag{3.12}$$

$$\begin{gathered} C_{11} > 0,\ C_{22} > 0,\ C_{33} > 0,\ C_{44} > 0,\ C_{55} > 0,\ C_{66} > 0, \\ (C_{11} + C_{22} - 2C_{12}) > 0,\ (C_{11} + C_{33} - 2C_{13}) > 0,\ (C_{22} + C_{33} - 2C_{23}) > 0, \\ (C_{11} + C_{22} + C_{33} + 2C_{12} + 2C_{13} + 2C_{23}) > 0; \end{gathered} \tag{3.13}$$

respectively.

Since elastic properties of materials can be described in different ways, different relations between single-crystal and polycrystalline parameters exist. As was suggested by Voigt [167], the polycrystalline bulk (B) and shear (G) moduli can be expressed in the appropriate combinations of single-crystal elastic constants $C_{\alpha\beta}$:

$$B_{\mathrm{V}} = \frac{1}{9}[C_{11} + C_{22} + C_{33} + 2(C_{12} + C_{13} + C_{23})], \tag{3.14}$$

$$G_{\mathrm{V}} = \frac{1}{15}[C_{11} + C_{22} + C_{33} - C_{12} - C_{13} - C_{23} + 3(C_{44} + C_{55} + C_{66})]. \tag{3.15}$$

Analogously, Reuss [168] has derived the bulk and shear moduli expressions in terms of compliance constants $S_{\alpha\beta}$:

$$B_{\mathrm{R}} = [S_{11} + S_{22} + S_{33} + 2(S_{12} + S_{13} + S_{23})]^{-1}, \tag{3.16}$$

$$G_{\mathrm{R}} = 15[4(S_{11} + S_{22} + S_{33} - S_{12} - S_{13} - S_{23}) + 3(S_{44} + S_{55} + S_{66})]^{-1}. \tag{3.17}$$

Voigt has based his formulation on the assumption that the strain is uniform throughout the sample, whereas the stress can be discontinuous. Reuss, on the contrary, has assumed that the stress is uniform allowing the strain to be discontinuous. Since in the first model the forces between the grains will not be in equilibrium, and in the second the distorted grains will not fit together, Hill [169] has shown that, for any crystalline structure, the assumptions of Voigt and Reuss correspondingly lead to an upper and lower bounds of B and G. In solid-state physics, it is common to use the arithmetic average of Voigt and Reuss bounds for the evaluation of B and G. It is called the Voigt-Reuss-Hill (VRH) approximation:

$$X_{\mathrm{VRH}} = \frac{1}{2}(X_{\mathrm{V}} + X_{\mathrm{R}}),\ X \equiv B, G. \tag{3.18}$$

Regarding the general relations between Poisson's ratio (ν), bulk, shear, and Young's (Y) moduli [164], the VRH approximation for ν and Y can be written in the form of

$$\nu_{\mathrm{VRH}} = \frac{3B_{\mathrm{VRH}} - 2G_{\mathrm{VRH}}}{2(3B_{\mathrm{VRH}} + G_{\mathrm{VRH}})}, \tag{3.19}$$

$$Y_{\mathrm{VRH}} = \frac{9B_{\mathrm{VRH}}G_{\mathrm{VRH}}}{3B_{\mathrm{VRH}} + G_{\mathrm{VRH}}}. \tag{3.20}$$

Alternatively, the bulk modulus can be evaluated by fitting the total energy as a function of volume to the third order Birch-Murnaghan (BM) equation of state [170]:

$$E(V) = E_0 + \frac{9V_0B}{16}\left(\left[\left(\frac{V_0}{V}\right)^{\frac{2}{3}} - 1\right]^3 B' + \left[\left(\frac{V_0}{V}\right)^{\frac{2}{3}} - 1\right]^2 \left[6 - 4\left(\frac{V_0}{V}\right)^{\frac{2}{3}}\right]\right), \tag{3.21}$$

in which E_0 and V_0 denote the total energy and volume of equilibrium configuration, respectively, whereas V is the volume of deformed structure and B' stands for the pressure derivative of bulk modulus. The procedure is based on the constant volume but full geometry optimization under $\varepsilon_{11} = \varepsilon_{22} = \varepsilon_{33} = \delta$ (remaining $\varepsilon_{kl} = 0$) deformations of the unit cell. For each phase of $\mathrm{SrRuO_3}$, 11 points were fitted within the range of 0.92–1.08 variation of the initial volume V_0. Since in this study all the aforementioned macroscopic elastic parameters by default are presented using VRH approximation, the bulk modulus and its pressure derivative obtained from the BM equation of state will be correspondingly denoted as B_{BM} and B'_{BM}.

For polycrystalline material, the longitudinal (v_{L}) and transverse (v_{T}) sound velocities can be written in terms of bulk and shear moduli obtained within the VRH approximation [164]:

$$v_{\mathrm{L}} = \sqrt{\frac{3B_{\mathrm{VRH}} + 4G_{\mathrm{VRH}}}{3\varrho}}, \tag{3.22}$$

$$v_{\mathrm{T}} = \sqrt{\frac{G_{\mathrm{VRH}}}{\varrho}}, \tag{3.23}$$

where ϱ denotes the mass density. The Debye temperature then has the form

$$\theta_{\mathrm{D}} = \frac{\hbar \bar{v}}{k_{\mathrm{B}}} \left(\frac{6\pi^2 N}{V_0} \right)^{\frac{1}{3}}, \tag{3.24}$$

where

$$\bar{v} = \left(\frac{1}{3} \left[\frac{1}{v_{\mathrm{L}}^3} + \frac{2}{v_{\mathrm{T}}^3} \right] \right)^{-\frac{1}{3}} \tag{3.25}$$

stands for an average sound velocity, N is the number of atoms per unit cell, and V_0 is its volume.

Chapter 4

Calculations of $LaNiO_3$

4.1 Crystalline Structure

Under ambient conditions, bulk $LaNiO_3$ crystallizes in a rhombohedral structure of space group $R\bar{3}c$ (No. 167) shown in Figure 4.1. This material also exhibits equal in magnitude out-of-phase rotations of NiO_6 octahedra — the following rotation system is classified according to Glazer notation[1] [171] as $a^-a^-a^-$. Similarly to other rhombohedrally distorted perovskites, $LaNiO_3$ undergoes a temperature-induced rhombohedral-to-cubic phase transition upon heating to high temperatures [10]. However, $LaNiO_3$ shows no metal-to-insulator transition retaining its metallic-like behaviour and paramagnetism in a wide range of temperatures [172].

Having in mind that many inherent material properties including phonon frequencies, elastic constants, and the possibility of structural phase transitions are critically dependent on change in volume [71,85], we primarily focus our attention on the accuracy of the calculated lattice constants and other structural parameters. The obtained values together with low-temperature experimental data are presented in Table 4.1. The mean absolute relative error (MARE) was evaluated according to the expression

$$\mathrm{MARE} = \frac{100}{n}\sum_{i=1}^{n}\left|\frac{p_i^{\mathrm{calc.}} - p_i^{\mathrm{expt.}}}{p_i^{\mathrm{expt.}}}\right|, \tag{4.1}$$

in which $p_i^{\mathrm{calc.}}$ and $p_i^{\mathrm{expt.}}$ are the calculated and experimental values of the considered parameter.[2] Notation PBE0 corresponds to the concept of the hybrid scheme

---

[1] In Glazer notation, rotation system is written as $a^*b^*c^*$ where the Latin letters specify the corresponding rotation angles around x, y, and z axes, while the superscripts indicate whether adjacent octahedra along a given axis rotate in-phase (+), out-of-phase (−), or not at all (0).

[2] Note that here and hereafter we did not apply the zero-point anharmonic expansion (ZPAE) corrections for the experimental data. On one hand, the ZPAE corrections are straightforwardly applicable only for the cubic systems [173]. On the other hand, ZPAE can expand the equilibrium lattice constant by 1% for light atoms like Li and much less for heavy atoms [100], thus it should not have a noticeable influence on materials like $LaNiO_3$ or $SrRuO_3$.

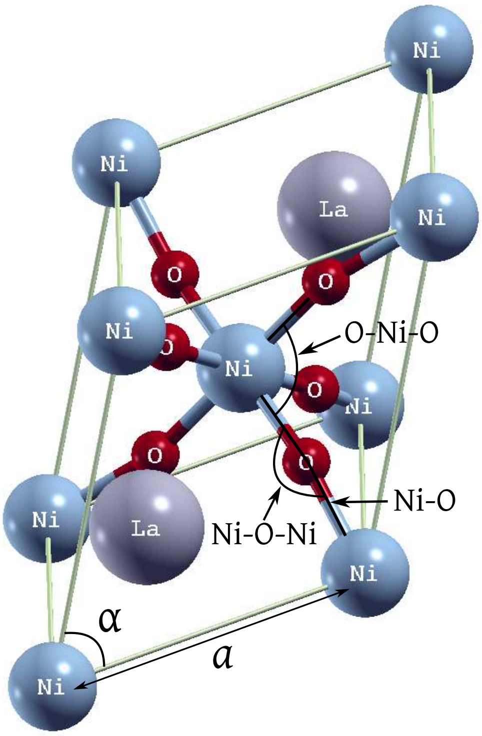

Figure 4.1 The crystalline structure of rhombohedral ($R\bar{3}c$) $LaNiO_3$. The structural parameters are presented in Table 4.1.

given by (2.68) where the part of HF mixing is varied from 15 to 40%.

As it could be expected, Table 4.1 reveals that LDA and PBE functionals tend to underestimate and overestimate lattice constant of $LaNiO_3$, respectively. As a direct consequence, this tendency is also reflected in a deviation of the volume values. However, the following results are in a good agreement with the recent plane-wave calculations [5, 10] demonstrating the reliability of our chosen basis set. Although the PBEsol exchange-correlation functional appears worse than PBE for the evaluation of the Ni-O-Ni bond angle, its performance for the most important structural parameters — a, α, and V — is truly impressive. The overall performance given by MARE leaves no doubt that the precise value of the second-order gradient expansion for exchange (2.59) has a huge impact on the crystalline structure of $LaNiO_3$.[3]

Interestingly, the inclusion of some part of the exact HF exchange — as it is in the PBE0 scheme — has a noticeable influence on the performance of PBE

---

[3] Notice that PBE and PBEsol functionals differ in the choice of parameters μ and β. But since the exchange energy in solids is larger than the correlation energy, we make an assumption that results should depend more sensitively on changes in μ.

Table 4.1 Calculated structural parameters of rhombohedral $LaNiO_3$ compared to the experimental data [174] at 1.5 K. Lattice constant a and bond distance Ni-O are given in Å, volume V is given in Å^3, angles α, Ni-O-Ni, and O-Ni-O are given in degrees. MARE (in %) stands for the mean absolute relative error. The numbers in brackets (in %) represent absolute relative errors for each of the considered parameters.

	LDA	PBEsol	PBE	PBE0 with percentage HF mixing						Expt.
				15%	20%	25%	30%	35%	40%	
a	5.338	5.378	5.447	5.417	5.407	5.398	5.388	5.380	5.371	5.384
	(0.85)	(0.11)	(1.17)	(0.62)	(0.44)	(0.26)	(0.08)	(0.08)	(0.24)	
α	60.72	60.94	61.13	60.69	60.59	60.46	60.41	60.30	60.20	60.86
	(0.23)	(0.13)	(0.44)	(0.28)	(0.44)	(0.65)	(0.74)	(0.92)	(1.08)	
V	109.30	112.29	117.15	114.16	113.29	112.38	111.64	110.84	110.06	112.48
	(2.82)	(0.17)	(4.15)	(1.49)	(0.72)	(0.09)	(0.75)	(1.46)	(2.15)	
Ni-O	1.907	1.927	1.960	1.937	1.930	1.923	1.917	1.912	1.905	1.933
	(1.35)	(0.27)	(1.40)	(0.18)	(0.16)	(0.52)	(0.80)	(1.11)	(1.43)	
Ni-O-Ni	168.78	166.87	164.61	167.66	168.52	169.63	170.42	171.56	172.97	164.82
	(2.40)	(1.24)	(0.13)	(1.72)	(2.25)	(2.92)	(3.40)	(4.09)	(4.94)	
O-Ni-O	89.12	88.83	88.54	89.08	89.21	89.37	89.45	89.59	89.72	88.78
	(0.38)	(0.07)	(0.27)	(0.34)	(0.49)	(0.67)	(0.75)	(0.91)	(1.06)	
MARE	1.34	0.33	1.26	0.77	0.75	0.74	0.96	1.43	1.82	

functional. As the amount of HF mixing increases from 30 to 40%, the MARE gets doubled and worsens the results of PBE, but within the range from 15 to 25% it remains at ∼0.75% showing an improvement over PBE. Yet, despite the following trend, the best result of PBE0 is still more than two times worse compared to that of PBEsol: 0.74 against 0.33%. If one would take into account the computational time and resources required for the calculations, PBEsol would have another advantage over the hybrid scheme of PBE0. Thus, to sum up, it can be stated that PBEsol appears to be the best choice among the considered functionals for the study of the crystalline structure of rhombohedral $LaNiO_3$.

4.2 Electronic Structure

Since calculations of the crystalline structure show that deviations from the experimentally observed geometry are functional-dependent, we have decided to apply the experimental lattice parameters while investigating the electronic structure of $LaNiO_3$. On one hand, it allows us to eliminate the differences that may rise due to the non-equivalent geometries distorting the direct comparison between various functionals. On the other hand, the exchange-correlation functional of PBEsol exhibits a very close resemblance to the experiment meaning that discrepancies in the electronic structure obtained with its own and experimental atomic positions should be negligible. For this reason, PBEsol was also chosen for demonstrating density of states (DOS), band structure, and electron density difference map of $LaNiO_3$.

The hard X-ray photoemission spectroscopy (HAXPES) spectrum of $LaNiO_3$, shown in Figure 4.2, is composed of three main regions. The lowest binding energy region in the vicinity of the Fermi level (E_F) contains a broad peak labelled A, above it lie four prominent peaks labelled B, C, D, and E, and the highest binding energy region contains another sharp peak labelled F. A detailed structure of peak A is presented in separate Figure 4.7. The total and projected DOS (PDOS) calculated using pure DFT approximation and the hybrid scheme with 30% of HF mixing are shown in Figures 4.3 and 4.4, respectively. Among all considered HF mixings, the latter was chosen due to its closest correspondence to the core region of the experimental spectrum (see Table 4.2). For a more accurate comparison, plots of the calculated DOS were broadened with Gaussian functions (FWHM = 0.6 eV)[4] to account for the experimental resolution.

The analysis of Figures 4.3 and 4.4 reveals that the valence band is mainly formed by Ni 3*d* and O 2*p* orbitals, whereas the upper core band is formed by La 5*p* and O 2*s* orbitals. The lower core band is essentially dominated by a pure La 5*s* shell. One can also notice a strong hybridization between Ni 3*d* and O 2*p* orbitals as well as a weak appearance of La 5*d* states in the valence region indicating significant and negligible covalent contributions to Ni-O and La-O chemical bonds, respectively (see Table 4.4 and Figure 4.9 for more details).

By comparing calculated and experimental spectra it can be noted that Figures 4.3 and 4.4 exhibit only three peaks in the La 5*p*/O 2*s* region, whereas in Figure 4.2 four peaks B, C, D, and E are distinguished. As our results show a very good qualitative agreement with the plane-wave based calculations [9,10,172], it took us awhile to find out the actual reason for the discrepancy. And, surprisingly enough, it proved to be by no means straightforwardly approachable. Since $LaNiO_3$ can

---

[4] FWHM stands for the full width at half maximum.

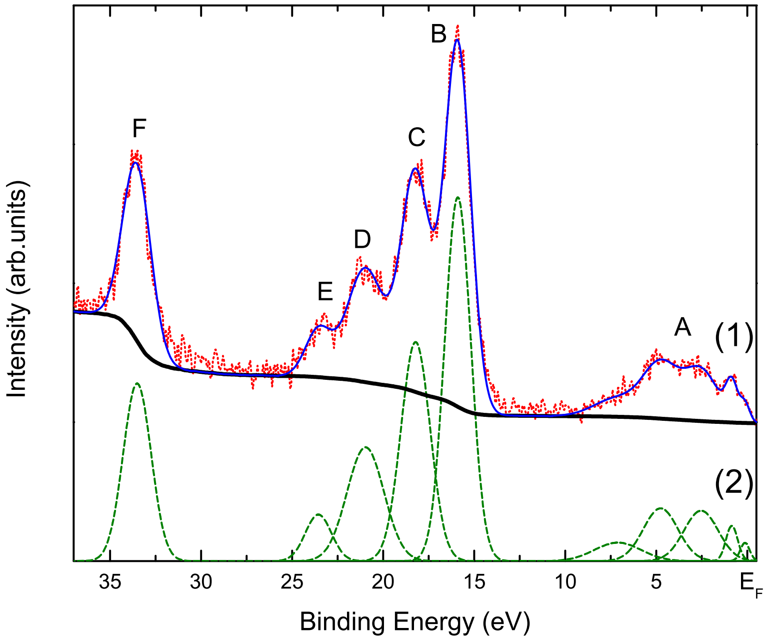

Figure 4.2 HAXPES ($h\nu = 3000$ eV) spectrum of $LaNiO_{3-x}$ thin film grown onto monocrystalline (100)-plane oriented $NdGaO_3$ substrate: (1) experimental data (dots), Shirley background (thick solid line), and spectrum envelope (thin solid line), (2) least-squares fitted spectral components (dashed lines) [175].

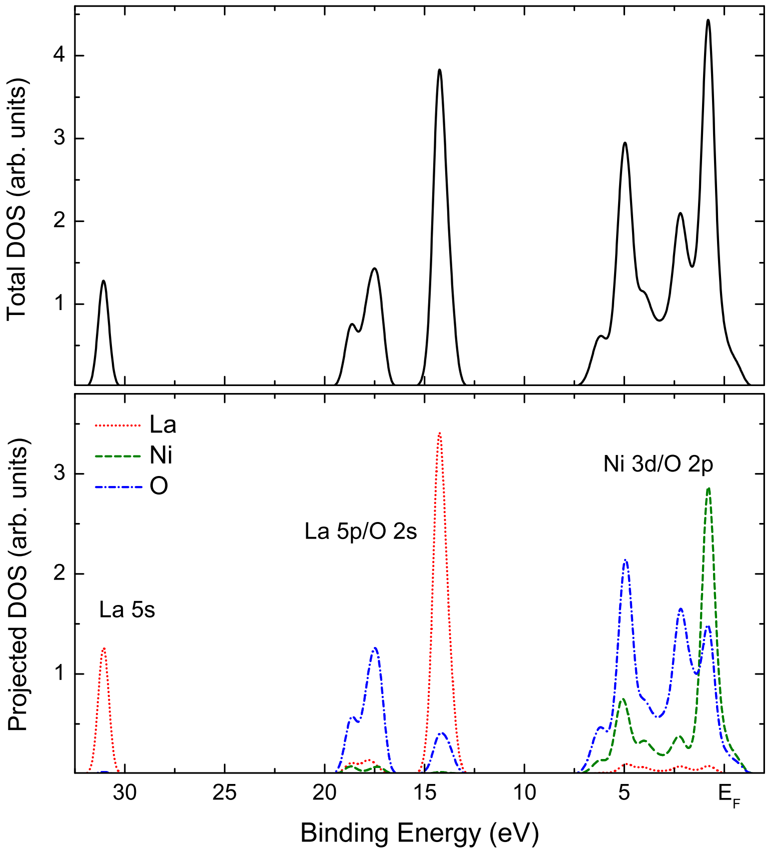

Figure 4.3 The total and projected DOS of $LaNiO_3$ calculated using PBEsol exchange-correlation functional.

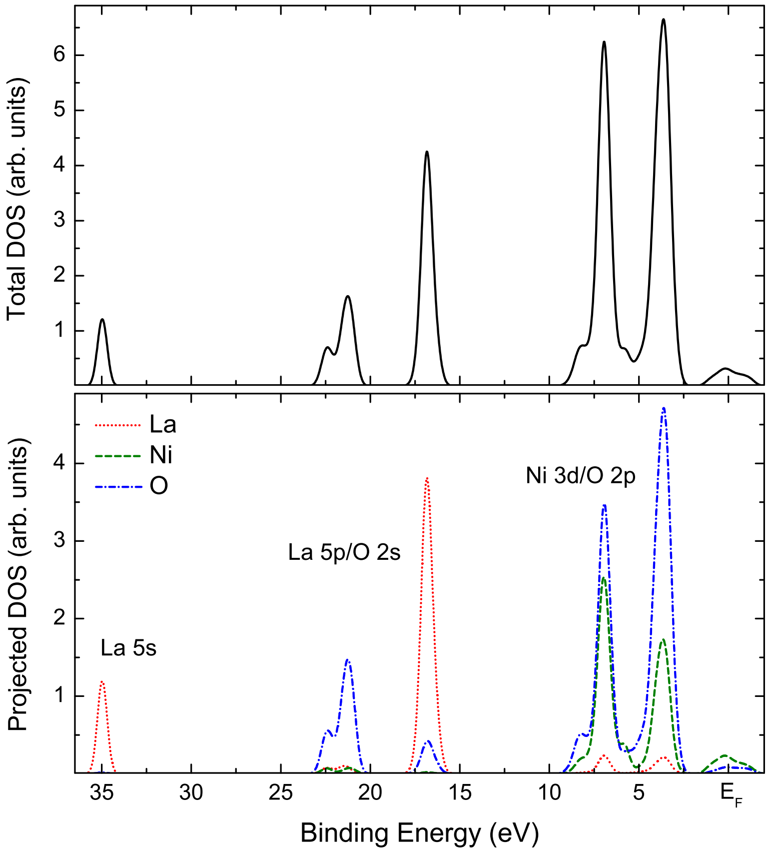

Figure 4.4 The total and projected DOS of $LaNiO_3$ calculated using hybrid PBE0 exchange-correlation functional with 30% HF mixing.

be considered as a heavy-element system, we made an assumption that fully relativistic treatment may have a great qualitative improvement on the calculated electronic structure. Thus, to evaluate not only scalar relativistic effects but also a spin-orbit interaction we carried out a computationally demanding relativistic HF study with DIRAC08. Although it has been made only at molecular level, La 5p/O 2s DOS presented in Figure 4.5(a) shows a good qualitative agreement with the structure of experimental spectrum, confirming our assumption. The doublet splitting of La 5p indicates that experimental peaks B and C should belong to La 5$p_{3/2}$ and 5$p_{1/2}$, respectively. Considerable shift in binding energy, seen in Figure 4.5(a), is most likely induced due to lack of strong crystalline field and electron correlation effects. Corresponding non-relativistic HF calculations performed with GAUSSIAN03 are presented in Figure 4.5(b). As it could be expected, they nicely agree with the structure of DOS calculated using CRYSTAL09.

As our theoretical investigation performed with CRYSTAL09 reproduces one La 5p peak instead of two with $J = 1/2$ and $J = 3/2$, we labelled it B/C and,

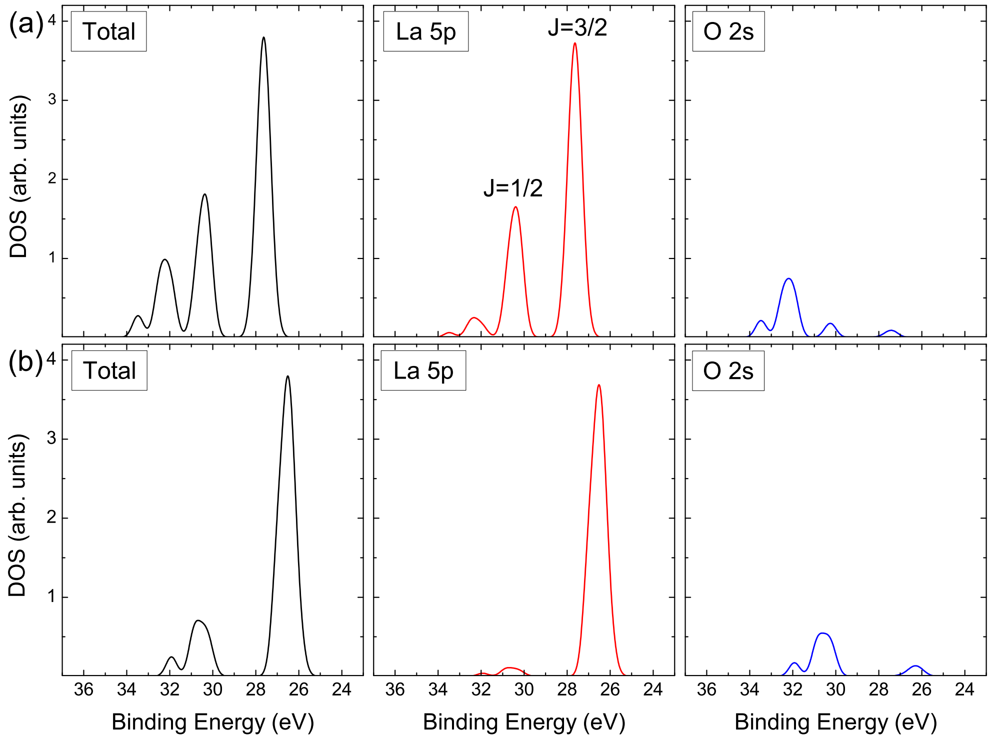

Figure 4.5 The total and projected DOS of La $5p$/O $2s$ region calculated at molecular HF level using: (a) DIRAC08 with relativistic Hamiltonian and (b) GAUSSIAN03 with non-relativistic Hamiltonian.

for a comparison, applied a simple expression which evaluates mean experimental binding energy of La $5p$:

$$E_{5p} = \frac{E_{5p_{3/2}}[J_{3/2}] + E_{5p_{1/2}}[J_{1/2}]}{[J_{3/2}] + [J_{1/2}]}, \tag{4.2}$$

where $[J_x] = 2x + 1$ expresses statistical weight of the energy level.

A comparison between the binding energies of experimental peaks D, E, F, mean value B/C, and corresponding calculated values is presented in Table 4.2. This table demonstrates that pure DFT calculations tend to underestimate binding energies of the core level states with MARE reaching ∼15%. In the meantime, hybrid scheme significantly improves the description of the peak positions, since at 30% of HF mixing MARE gets reduced to ∼3%. Interestingly, this optimum percentage of the exact HF exchange is very close to the theoretically ideal value of 25% showing a correlation with the results of structural parameters given in Table 4.1. It appears that there is no need to exceed 30% of HF mixing in PBE0 for the proper representation of crystalline and electronic structure of $LaNiO_3$.

The visual depiction of the shift in binding energy determined by the included

Table 4.2 Calculated binding energies (in eV) for the major energy peaks in the core region of the $LaNiO_3$ spectrum compared to the experimental data [175]. MARE (in %) stands for the mean absolute relative error. The numbers in brackets (in %) represent absolute relative errors for each of the considered peaks.

	LDA	PBEsol	PBE	PBE0 with percentage HF mixing						Expt.
				15%	20%	25%	30%	35%	40%	
B/C	14.02	14.25	14.39	15.55	15.97	16.40	16.85	17.25	17.69	16.67
	(15.93)	(14.50)	(13.69)	(6.71)	(4.20)	(1.62)	(1.08)	(3.48)	(6.12)	
D	17.26	17.49	17.60	19.35	20.02	20.58	21.26	21.84	22.56	20.97
	(17.72)	(16.58)	(16.07)	(7.73)	(4.53)	(1.86)	(1.38)	(4.15)	(7.58)	
E	18.43	18.62	18.75	20.50	21.12	21.75	22.38	23.04	23.71	23.56
	(21.78)	(20.98)	(20.42)	(12.99)	(10.36)	(7.68)	(5.01)	(2.21)	(0.64)	
F	30.85	31.06	31.34	33.09	33.72	34.35	34.97	35.61	36.23	33.51
	(7.93)	(7.30)	(6.46)	(1.25)	(0.63)	(2.51)	(4.36)	(6.27)	(8.12)	
MARE	15.84	14.84	14.16	7.17	4.93	3.42	2.96	4.03	5.62	

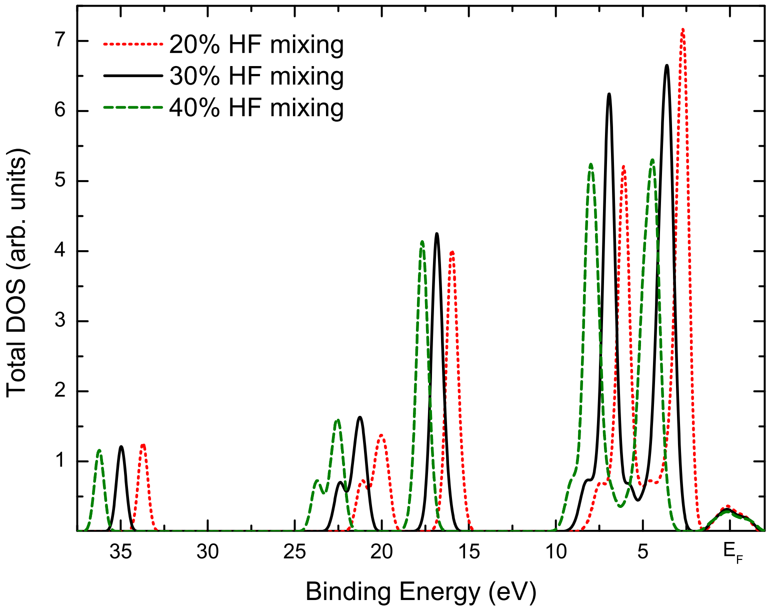

Figure 4.6 The comparison of total DOS of $LaNiO_3$ calculated within PBE0 framework at different percentage of HF mixing.

amount of exact exchange can be found in Figure 4.6. The following figure reveals that the shape of DOS is basically independent of the chosen percentage of HF mixing — the exact exchange solely affects the description of the peak positions.

Concerning the improvement of the hybrid functionals, it should be noted that unlike the hybridized and thus delocalized valence electrons the core level states retain their strongly localized electronic character. For this reason, the spurious SIE common for DFT approximations drastically increases, since LDA and GGA essentially describe non-interacting electrons moving in an effective self-consistent

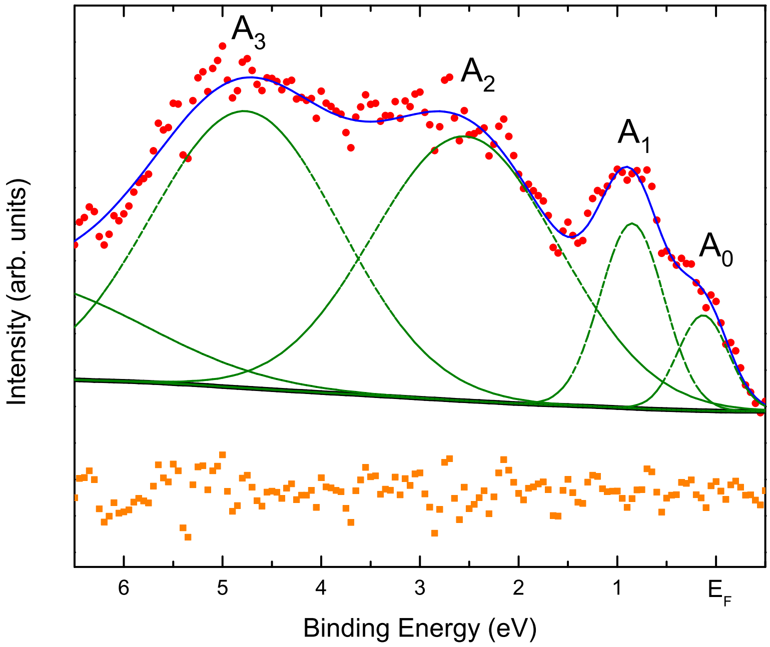

Figure 4.7 Detailed HAXPES spectrum of $LaNiO_{3-x}$ thin film in valence band region: experimental data (circles), Shirley background (thick solid line), spectrum envelope (thin solid line), least-squares fitted spectral components (dashed lines), and residual plot (squares) [175].

mean field. Although HF approximation is free of SIE, it omits correlation energy and therefore does not properly represent the physics in correlated materials. However, the incorporation of some amount of exact HF exchange into hybrid functionals partly compensates for the SIE and in this way substantially improves the results — as it could be seen from Table 4.2. In other words, the electronic structure of $LaNiO_3$ is a good example in which hybrid scheme can somewhat serve as a reasonable alternative for more sophisticated SIC-DFT or DFT + U methods.

Figure 4.7 presents a detailed structure of experimental spectrum in valence band region with four peaks labelled A_0, A_1, A_2, and A_3. A comparison with the calculations reveals that hybrid functionals fail to correctly reproduce the experiment exhibiting only two significantly shifted spectral features. On the contrary, DFT calculations demonstrate a fairly good agreement with energy peak positions A_1, A_2, and A_3 (see Table 4.3). This result can be explained by the fact that DFT approximations are perfectly consistent with the homogeneous electron gas model. Since $LaNiO_3$ shows a pronounced hybridization and also possesses a strong metallic character (see Figure 4.8), Ni 3d and O 2p electrons in valence

Table 4.3 Calculated binding energies (in eV) for the major energy peaks in the valence region of the $LaNiO_3$ spectrum compared to the experimental data [175]. MARE (in %) stands for the mean absolute relative error. The numbers in brackets (in %) represent absolute relative errors for each of the considered peaks.

	LDA	PBEsol	PBE	Expt.
A_1	0.78	0.81	0.80	0.85
	(8.82)	(4.66)	(6.12)	
A_2	2.08	2.19	2.25	2.54
	(18.27)	(13.86)	(11.34)	
A_3	4.91	4.97	4.93	4.76
	(3.11)	(4.37)	(3.55)	
MARE	10.07	7.63	7.00	

band can be considered as being effectively delocalized. The delocalized electrons experience mainly the DFT mean-field potential, thus allowing the homogeneous electron gas model to properly reproduce their properties. As hybrid functionals incorporate some part of exact HF exchange to compensate for the SIE, they behave well in regions where electrons preserve their strongly localized nature. But in the meantime, valence band region gets rather overcorrected. Pure DFT functionals due to spurious self-interaction underestimate binding energies in the core region but correctly reproduce the delocalized valence band. Thus, by applying pure DFT approximations and their hybrid schemes for the different regions of the binding energy spectrum it is possible to define the essential experimental findings.

A comparison between the binding energies of experimental peaks A_1, A_2, and A_3 and corresponding calculated values is listed in Table 4.3. We do not present the results of hybrid functionals because, as it was already mentioned, they apparently fail in predicting the correct energy peak positions. Among the remaining functionals, PBE and PBEsol demonstrate a very close performance with MARE reaching $\sim$7%. LDA performs slightly worse since its MARE increases to $\sim$10%. Although at first glance the values of MARE seem to be rather poor, one should take into account that the largest absolute error does not exceed 0.46 eV. This result points to a high accuracy of our calculations. However, we did not reproduce any structure that would correspond to a small peak A_0 lying in the vicinity of the Fermi level. The following spectral feature appears to be related to an enhanced screening of electron-electron interaction which in turn

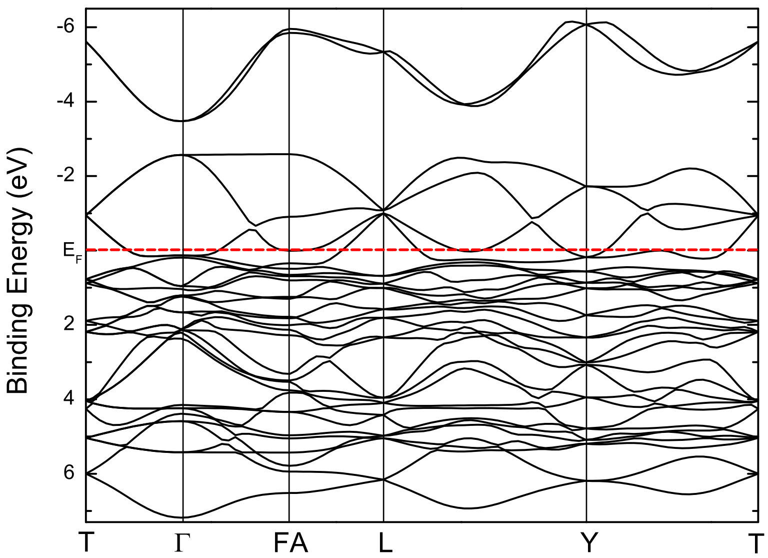

Figure 4.8 The band structure of $LaNiO_3$ calculated using PBEsol exchange-correlation functional. The Fermi level is indicated by a horizontal dashed line.

leads to a renormalization of the electronic states at the Fermi level [10]. All of the methods applied here exhibit overdelocalization of itinerant Ni 3*d* electrons, since the precise treatment of this subtle phenomenon requires the inclusion of dynamical screening effects which, unfortunately, are only available at the GW or DMFT level.

Despite the inability to distinguish peak A_0, the band structure obtained using PBEsol exchange-correlation functional indicates a strong metallic character of $LaNiO_3$. As it can be seen in Figure 4.8, the intercross of the highest valence and the lowest conduction bands leaves no place for the occurrence of the bandgap. It once more confirms the idea that DFT approximations are able to reproduce the most important experimentally observed properties of $LaNiO_3$.

The electron density difference map obtained by subtracting the superposition of spherical atomic charge distributions from the crystalline electron density is shown in Figure 4.9. It should be stresses that unlike the plane-wave framework, the LCAO approach directly allows this type of analysis. Figure 4.9 reveals that electron density significantly increases at the O atom in the La-O bond direction, whereas the La atom is mainly surrounded by negative isolines, implying that the La-O bond has a predominantly ionic character. The decrease in electron density at both O and Ni atoms gradually transforming to positive isolines within the Ni-O bond shows a substantial covalent part in the Ni-O bond. The following

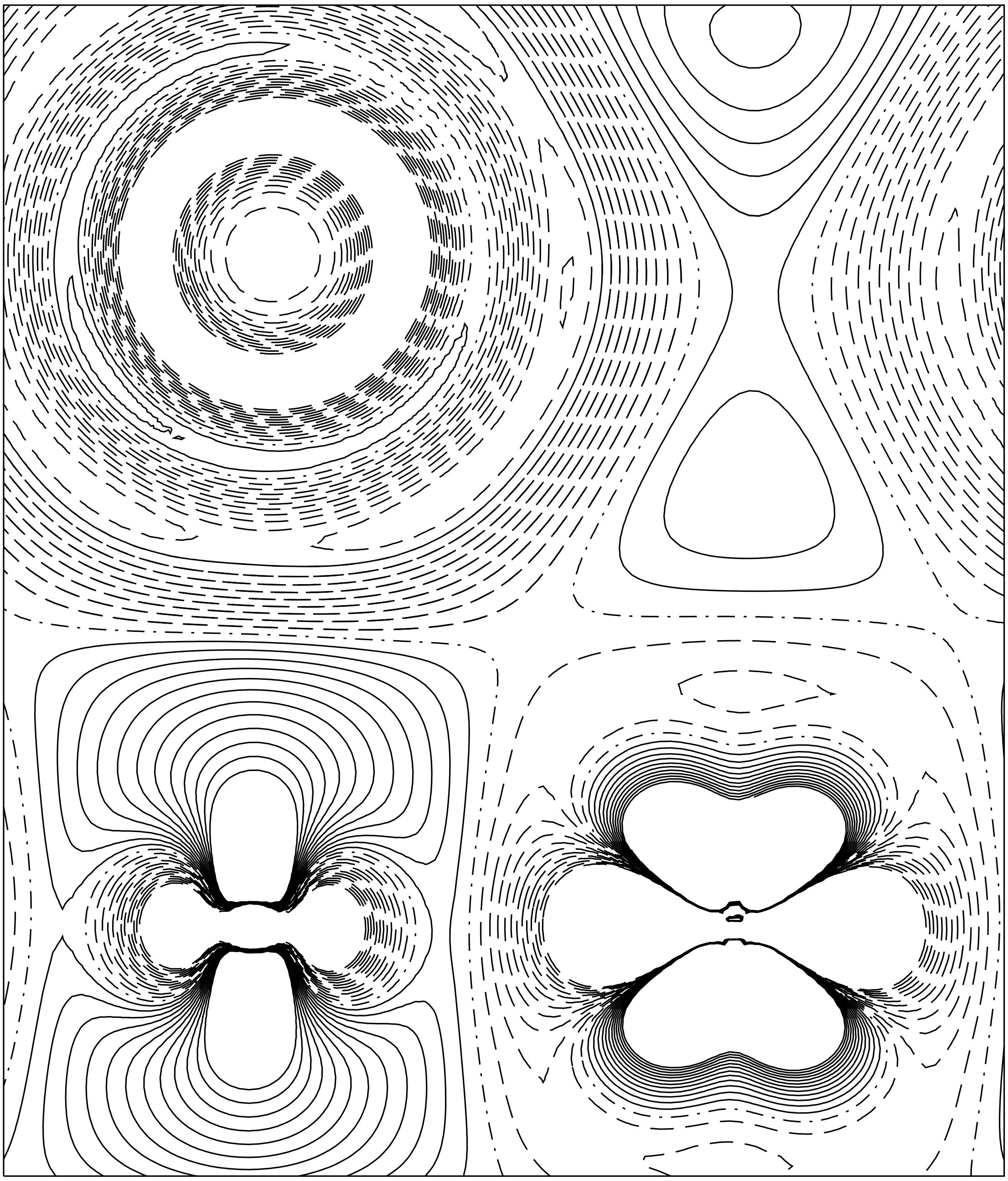

Figure 4.9 The electron density difference map of $LaNiO_3$ given as a difference between the crystalline electron density and the superposition of spherical atomic charge distributions. Calculations were performed using PBEsol exchange-correlation functional. Continuous, dotted-dashed, and dashed isolines represent positive, zero value, and negative differences of density in comparison to the neutral atoms, respectively. The isolines are drawn from -0.03 to 0.03 e/bohr^3 with a step of 0.0025 e/bohr^3. La, O, and Ni atoms are at the top left, bottom left, and bottom right side of the map, respectively.

Table 4.4 Mulliken atomic charges Q (in e) and overlap populations OP (in 10^{-3} e) in $LaNiO_3$ obtained using different functionals.

	LDA	PBEsol	PBE	PBE0 with percentage HF mixing					
				15%	20%	25%	30%	35%	40%
Q(La)	+2.453	+2.530	+2.514	+2.563	+2.578	+2.592	+2.605	+2.618	+2.631
Q(Ni)	+0.946	+0.997	+1.025	+1.070	+1.086	+1.102	+1.118	+1.135	+1.151
Q(O)	−1.163	−1.176	−1.180	−1.211	−1.221	−1.231	−1.241	−1.251	−1.261
OP(La-O)	−10	−9	−9	−16	−18	−20	−23	−25	−27
OP(Ni-O)	144	142	142	136	134	134	132	130	128

pictorial representation confirms our previous remarks made on chemical bonding in $LaNiO_3$, as predominantly ionic nature of La-O bond is also indicated by a much weaker hybridization than that of Ni-O atoms, apparently seen in Figures 4.3 and 4.4.

The Mulliken population analysis, also directly available using the LCAO approach, is given in Table 4.4. Although this sort of analysis is arbitrary and basis set dependent, it demonstrates that our results differ from formal ionic picture of La^{3+}, Ni^{3+}, and O^{2-}. The Mulliken charges found for the La, Ni, and O atoms are $\sim +2.5$, $\sim +1$, and ~ -1.2, respectively, exhibiting a weak dependence on the applied functionals. To be precise, one can notice that the atomic charges tend to slightly increase as the part of the exact exchange included in calculations gets larger. A high positive value of overlap population indicates a high degree of covalency in the bond, while a value around zero implies an ionic bond. Thus, within the accuracy of the Mulliken scheme, it can be concluded that the following analysis, electron density difference map, and figures of DOS are in tune with each other revealing a combination of covalent and ionic nature of $LaNiO_3$. The obtained results are consistent with findings from previous studies [172,176], despite that in [176] $LaNiO_3$ is more ionic, whereas in [172] it shows more covalency.

Chapter 5

Calculations of $SrRuO_3$

5.1 Crystalline Structure

At room temperature, bulk $SrRuO_3$ crystallizes in an orthorhombic (space group *Pbnm*, No. 62) $GdFeO_3$-type perovskite structure, in which the RuO_6 octahedra are tilted according to $a^-a^-c^+$ Glazer rotation pattern [see Figure 5.1(a)] [177]. As the temperature increases up to 950 K, this compound undergoes a series of phase transformations: an orthorhombic structure of $SrRuO_3$ consecutively transforms to tetragonal $I4/mcm$ (No. 140), stable in the temperature range of 820–950 K, and then to cubic $Pm\bar{3}m$ (No. 221) symmetry [40,44,178]. Concerning the recent low-temperature studies, it has been reported [179] that the crystalline structure of an orthorhombic phase remains practically invariable in the temperature range of 1.5–290 K. This finding is perfectly consistent with the previously discovered Invar effect [21] due to which the crystalline structure of $SrRuO_3$ undergoes only tiny changes below 160 K. What is more, $SrRuO_3$ retains its metallic character throughout the aforementioned high-temperature phases despite the fact that ferromagnetic behaviour of this perovskite is lost above 160 K.

The calculated equilibrium lattice constants together with other structural parameters of orthorhombic $SrRuO_3$ are given in Table 5.1. Notice that we do not present an analogous analysis for tetragonal and cubic phases of $SrRuO_3$ due to the thermal expansion which requires an extrapolation of high-temperature experimental data to 0 K. The accuracy of such procedure may be insufficient and thereby distort the results. Also, we did not include hybrid functionals in any calculations of $SrRuO_3$ because of their irrelevance for reproducing valence band of metallic systems and demand for computational resources.

As in case of $LaNiO_3$, Table 5.1 demonstrates that LDA and PBE functionals respectively underestimate and overestimate lattice constants and volume of $SrRuO_3$. In the meantime, calculated values of the revised functionals fall within

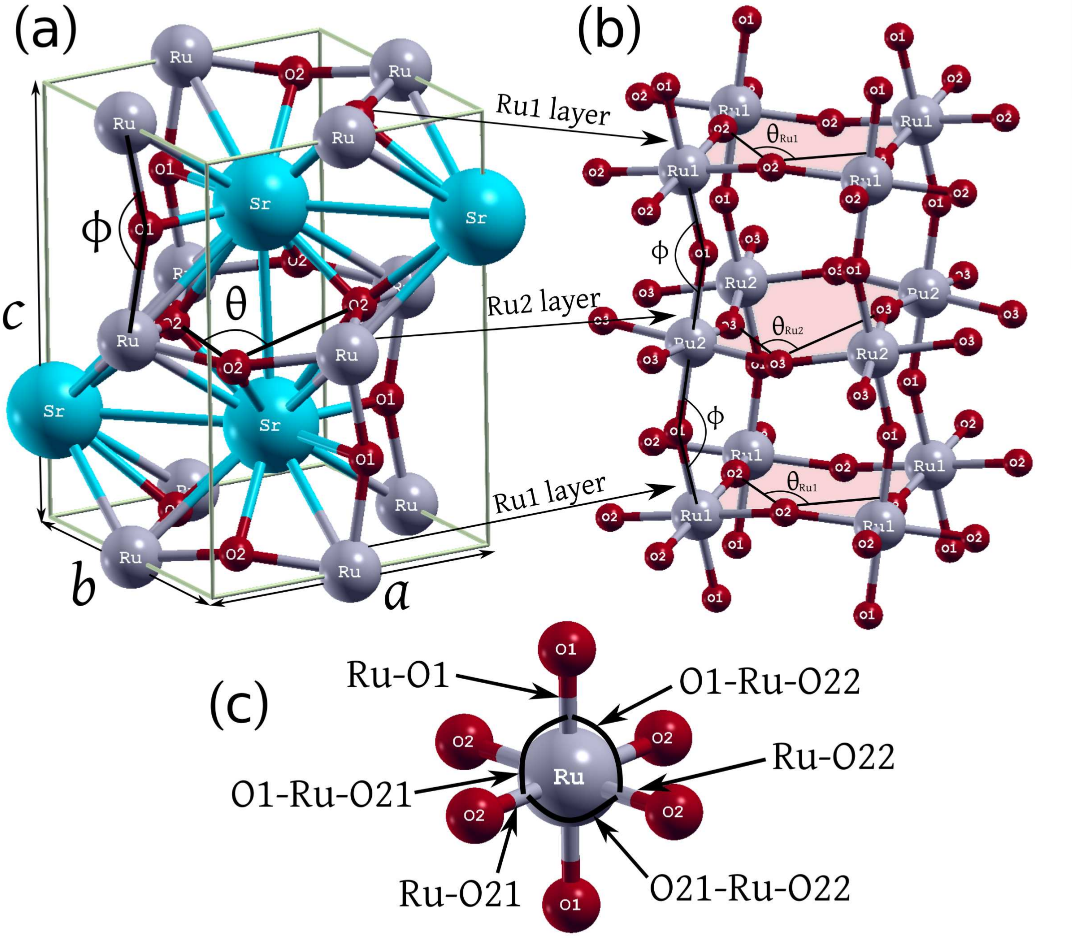

Figure 5.1 Schematic representation of (a) the crystalline structure of ground-state orthorhombic ($Pbnm$) $SrRuO_3$, (b) its RuO_6 octahedra network under C_{44} related shear deformation, and (c) octahedral parameters. The tilting angle of octahedra is defined through the relation $\Phi = (180° - \phi)/2$, whereas rotation angle is expressed as $\Theta = (90° - \theta)/2$. Due to strain-induced structural transformation, non-equivalent rotation angles for $Ru1O_6$ and $Ru2O_6$ exist [180].

the range between LDA and PBE and, most importantly, show a very good correspondence to the experiment.[1] If one would take MARE only for a, b, c, and V, the obtained results for LDA, PBEsol, and PBE would be 1.05, 0.22, and 2.08%, correspondingly. It indicates a significant improvement in favour of the revised scheme, despite that overall performance of LDA (1.03%) is just slightly worse than that of PBEsol (0.87%). One can note that independently of the functional used angles ϕ and θ are affected by larger relative errors than other lattice parameters. This is because DFT calculations are less sensitive to the subtle arrangement of octahedra compared to the stretching of interatomic distances.

---

[1] According to [82], revised functionals yield “good” theoretical values, since deviation from the experiment does not exceed 0.5% for any of the lattice constant of orthorhombic $SrRuO_3$.

Table 5.1 Calculated structural parameters of orthorhombic $SrRuO_3$ compared to the experimental data [179] at 1.5 K. Lattice constants a, b, and c together with bond distances Ru-O1, Ru-O21, and Ru-O22 are given in Å, volume V is given in Å^3, angles ϕ, θ, O1-Ru-O21, O1-Ru-O22, and O21-Ru-O22 are given in degrees [see Figure 5.1(a) and (c)]. MARE (in %) stands for the mean absolute relative error. The numbers in brackets (in %) represent absolute relative errors for each of the considered parameters.

	LDA	SOGGA	PBEsol$^{\text{PBE}}$	PBEsol	WC	PBE	Expt.
a	5.527	5.556	5.558	5.568	5.570	5.631	5.556
	(0.52)	(0.00)	(0.04)	(0.22)	(0.25)	(1.35)	
b	5.491	5.529	5.533	5.543	5.548	5.621	5.532
	(0.74)	(0.05)	(0.02)	(0.20)	(0.29)	(1.61)	
c	7.779	7.824	7.828	7.841	7.846	7.937	7.845
	(0.84)	(0.27)	(0.22)	(0.05)	(0.01)	(1.17)	
V	236.06	240.33	240.71	241.99	242.47	251.21	241.12
	(2.10)	(0.33)	(0.17)	(0.36)	(0.56)	(4.18)	
ϕ	158.98	159.12	159.16	158.89	158.78	158.50	161.99
	(1.86)	(1.77)	(1.75)	(1.91)	(1.98)	(2.15)	
θ	74.04	73.86	73.84	73.82	73.68	73.42	77.31
	(4.23)	(4.46)	(4.49)	(4.51)	(4.70)	(5.03)	
Ru-O1	1.978	1.989	1.990	1.994	1.996	2.020	1.986
	(0.40)	(0.15)	(0.20)	(0.40)	(0.50)	(1.71)	
Ru-O21	1.987	1.999	2.001	2.004	2.006	2.031	1.986
	(0.05)	(0.65)	(0.76)	(0.91)	(1.01)	(2.27)	
Ru-O22	1.985	1.998	1.999	2.003	2.005	2.029	1.987
	(0.10)	(0.55)	(0.60)	(0.81)	(0.91)	(2.11)	
O1-Ru-O21	90.39	90.33	90.31	90.28	90.27	90.13	90.33
	(0.07)	(0.00)	(0.02)	(0.06)	(0.07)	(0.22)	
O1-Ru-O22	91.16	91.09	91.07	90.98	90.97	90.67	90.27
	(0.99)	(0.91)	(0.89)	(0.79)	(0.78)	(0.44)	
O21-Ru-O22	91.43	91.32	91.30	91.31	91.30	91.18	91.07
	(0.40)	(0.27)	(0.25)	(0.26)	(0.25)	(0.12)	
MARE	1.03	0.78	0.78	0.87	0.94	1.86	

The fact that we used the same correlation functional for SOGGA, PBEsol$^{\text{PBE}}$, WC, and PBE allows us to present a few insights into the inner structure of $SrRuO_3$. Firstly, the step that leads from $F_{\text{X}}^{\text{PBE}}(s)$ to $F_{\text{X}}^{\text{PBEsol}}(s)$ seems to be the most important for the accurate description of the lattice parameters of $SrRuO_3$. This can be easily noticed by comparing the results of PBEsol$^{\text{PBE}}$ and PBE, since the only difference between these two functionals is the value of parameter μ, which was set from $\mu_{\text{PBE}} = 0.2195$ to $\mu_{\text{PBEsol}} = \frac{10}{81} \approx 0.1235$. Secondly, the modification of parameter β ($\beta_{\text{PBE}} = 0.0667 \rightarrow \beta_{\text{PBEsol}} = 0.046$), which appears in the correlation functional, has much less impact (seen from comparison between PBEsol$^{\text{PBE}}$

and PBEsol), indicating that the magnitude of the exchange energy is substantially larger than the correlation energy. What is more, the change in the form of the exchange enhancement factor for SOGGA and WC[2] does not have a significant influence on the overall performance compared to that of PBEsol$^{\text{PBE}}$. This allows to conclude that the PBE-like functionals with the parameter μ restored back to $\frac{10}{81}$ can be considered as simple but reliable tool for the investigation of the crystalline structure of $SrRuO_3$. For this reason, we choose PBEsol as a default functional for the demonstration of $SrRuO_3$ behaviour and properties throughout the rest of the study.

A comparison to other calculations in which the revised functionals were used [43] reveals similar trends and a reasonable quantitative agreement with our results. Although we demonstrate a closer correspondence to the experiment, it is important to note that in [43] the ferromagnetic configuration of $SrRuO_3$ was modelled.[3] However, the match would be probably better if the same basis sets for O and Ru atoms were applied. Especially for the latter, since basis sets optimized in a system under consideration may provide an appreciable improvement.

5.2 Electronic Structure

The electronic structure of orthorhombic $SrRuO_3$ obtained with PBEsol lattice parameters is presented in Figure 5.2. For a better comparison with experimental data, the plots of DOS were broadened with Gaussian functions (FWHM=0.5 eV).[4] Here, it is seen that valence band is essentially formed by strongly hybridized Ru 4*d* and O 2*p* orbitals with contribution from Sr 4*d* being negligible. What is more, the sharp peak at the Fermi level is dominated by Ru 4*d* character, whereas O 2*p* is more pronounced in the range of 2–8 eV below E_{F}. This result is nicely consistent with previous plane-wave DFT calculations [32, 37, 181, 182] demonstrating high reliability from a theoretical perspective.

---

[2] See (2.44), then (2.61)–(2.63).

[3] Here and hereafter, we are modelling the paramagnetic behaviour of $SrRuO_3$ by non-magnetic calculations. The transition from ferromagnetic to paramagnetic state of $SrRuO_3$ at 160 K practically does not affect its crystalline structure, therefore the non-magnetic calculations should give very close structural values to the ferromagnetic ones.

[4] Actually, to account for the instrumental resolution of HAXPES spectra (see Figures 5.4 and 5.5).

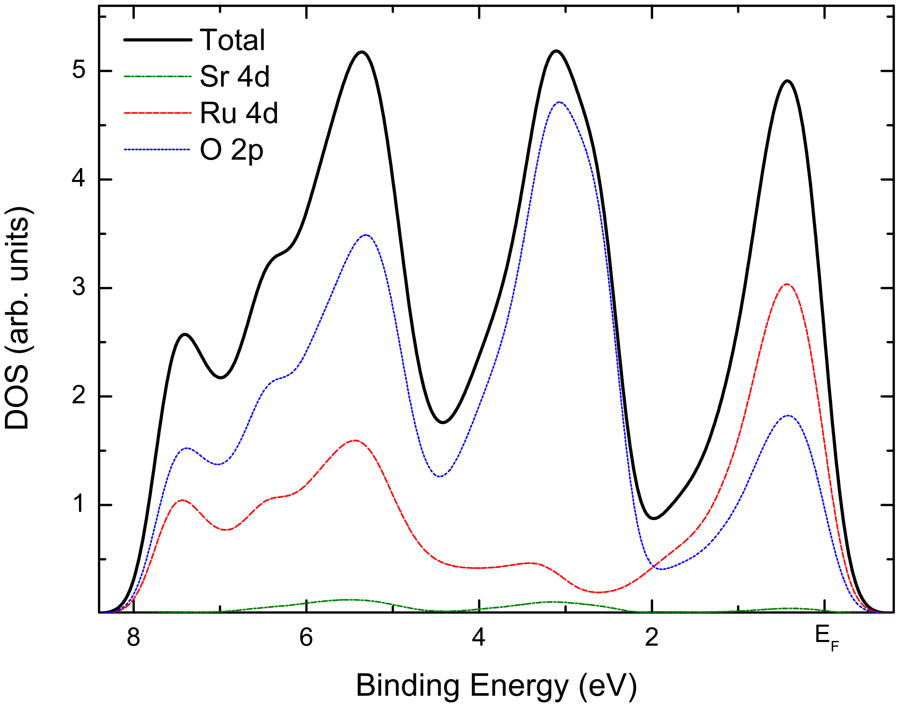

Figure 5.2 The total and projected DOS of $SrRuO_3$ calculated using PBEsol exchange-correlation functional.

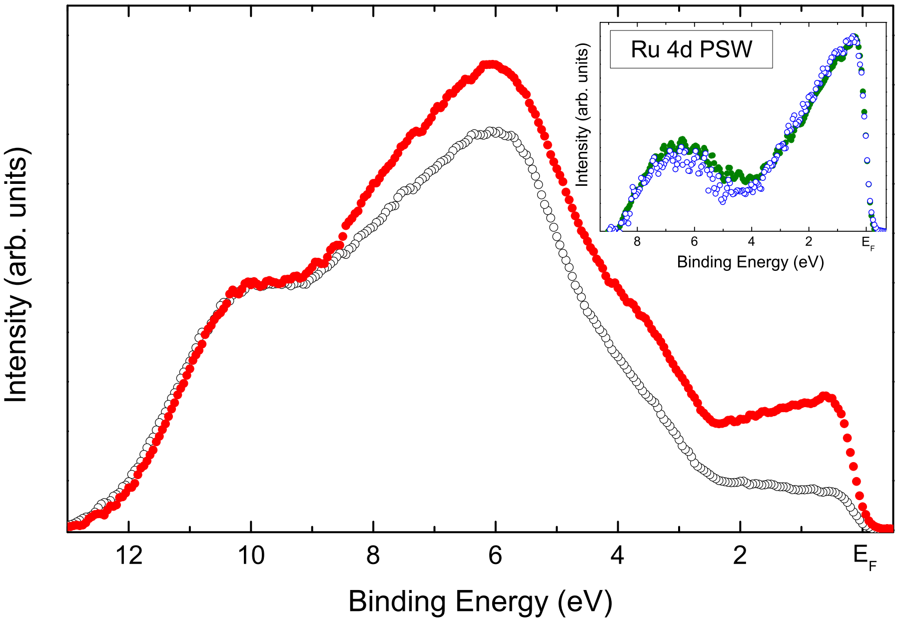

Figure 5.3 UPS spectra of $SrRuO_3$ thin film measured at Ru $4p \rightarrow 4d$ on-resonance ($h\nu = 59.5$ eV, filled circles) and off-resonance ($h\nu = 45.5$ eV, open circles) conditions after annealing in ultra-high vacuum at 200 °C for cleaning the surface of the sample. At the off-resonance condition, the contribution of Ru $4d$ to the total spectrum is only due to the direct photoemission process $4p^6 4d^n + h\nu \rightarrow 4p^6 4d^{n-1} + e$, but, at the on-resonance condition, the contribution is enhanced due to the additional excitation $4p^6 4d^n + h\nu \rightarrow 4p^5 4d^{n+1} \rightarrow 4p^6 4d^{n-1} + e$. The inset demonstrates the extracted Ru $4d$ PSW by two different methods [183].

The ultraviolet photoemission spectroscopy (UPS) spectra of $\mathrm{SrRuO_3}$, normalized to the intensity of contaminant carbon monoxide peak[5] at ∼10 eV, are given in Figure 5.3. The relative variation of these valence band spectra measured at on-resonance and off-resonance conditions is much larger for E_F–2 eV region compared to 2–8 eV region, confirming theoretical findings that Ru 4d states dominate in the vicinity of E_F, while O 2p states are mostly located at higher binding energies. Moreover, the inset reveals that the extracted Ru 4d partial spectral weight (PSW) spreads over a wide energy range[6] and is in a good quantitative accordance with Ru 4d PDOS in Figure 5.2, particularly for the bandwidth and height ratio of peaks at E_F and ∼6 eV. One can also notice that the intense Ru 4d coherent part[7] of the spectrum near the Fermi level is clearly identified in the experimentally extracted Ru 4d PSW. These observations make us believe that a spectral weight transfer from coherent to incoherent feature resulting in an apparent disagreement with DFT calculations — previously noticed for UPS measurements with *ex situ* specimens[8] [31–33,184–187] — could be eliminated by applying an advanced handling of experimental data and/or relevant preparation of samples. As it was suggested in [34], *in situ* grown and thus additional surface cleaning free thin films may provide the best opportunity to employ photoemission spectroscopy (PES) for studying intrinsic electronic structure of $\mathrm{SrRuO_3}$. Indeed, *in situ* prepared specimens have exhibited noticeably sharper Ru 4d PSW at the Fermi level [34,35], supporting the idea that the absence of coherent feature of the spectrum — which is taken as a proof of strong electron correlation in $\mathrm{SrRuO_3}$ — could be originated by the contribution from the affected electronic structure at the surface. It should be noted that less surface-sensitive X-ray PES measure-

---

[5] It is well known that a peak at around 10 eV rises due to the contaminations, most likely by carbon monoxide, on the surface or within the specimen [34, 184]. Since O 2p photoionization cross-section dependence on $h\nu$ is similar to that of CO, the normalization to this peak allows to distinguish the contribution of Ru 4d to the total spectrum.

[6] This is consistent with the expectation that 4d orbital is quite extended and makes a strong covalent bonding, as predicted by DFT calculations [183].

[7] The coherent feature at E_F corresponds to the delocalized states of electrons, whereas incoherent feature at 1.2–1.5 eV below E_F is generally attributed to the correlation-induced localized electronic states.

[8] Usually, the specimens are either introduced into the analysis chamber from outside the vacuum (*ex situ*), and subsequently cleaned by common annealing or scraping techniques, or grown in vacuum and transferred into an adjacent analysis chamber without breaking the vacuum (*in situ*) [23].

ments have also revealed a clearly pronounced Ru 4d peak at E_F [36, 188–190]. For all these reasons, we strongly believe that SrRuO$_3$ is a weakly correlated system and its bulk electronic structure can be successfully described by DFT approximations, since in this material valence band electrons are delocalized and self-interaction errors are negligible. The complete dominance of incoherent feature of the spectrum indicating the localized electronic states could be attributed to external factors, e.g., surface roughness, defects, or change of the symmetry that may occur during the growth and/or cleaning process.

In order to see how the Ru 4d PSW changes along the depth of the sample, we have examined the HAXPES spectrum dependence on the emission angle. Figure 5.4(b) shows a cumulative plot of valence band obtained by averaging spectra measured at different emission angles [see Figure 5.4(a)]: from $\alpha = 8°$ to $\alpha = 90°$, corresponding to the photoelectron escape depth that ranges from 1.5 to 10.7 monolayers (MLs).[9] The spectrum was fitted with six Gaussian peaks, thus valence band exhibits six distinct features marked by A, B, C, D, E, and F. Our theoretical calculations in Figure 5.2 reveal that the band between E_F and ∼2 eV is mainly composed of Ru 4d states, whereas O 2p states become dominant in the region of 2–4 eV (C). The sharp peak near the Fermi level (A) and the broad one centred at ∼1.2 eV (B) are assigned to the coherent and incoherent parts of the spectral function, respectively [31, 37, 185]. The peaks D and E can be attributed to the mixture of Ru 4d and O 2p orbitals. The finite emission at 8–11 eV (negligible peak F) is due to the contaminations.

At higher (> 300 eV) photon energies, the photoionization cross-section of O 2p electrons decreases more rapidly than that of Ru 4d electrons. For example, the atomic calculations predict Ru 4d/O 2p cross-section ratio of ∼36 and ∼74 for $h\nu = 1500$ and 8047.8 eV, respectively [192, 193]. Rough interpolation provides Ru 4d/O 2p cross-section ratio of ∼50 for $h\nu = 3000$ eV. In solids, due to the hybridization between O 2p and Ru 4d orbitals the following value somewhat decreases, but despite that Ru 4d states should form the main part of photoemission spectra measured in the vicinity of E_F. This becomes evident when the shape of spectra presented in Figure 5.4 is compared to that of UPS spectra (Figure 5.3)

---

[9] The value of inelastic mean free path was taken from [191].

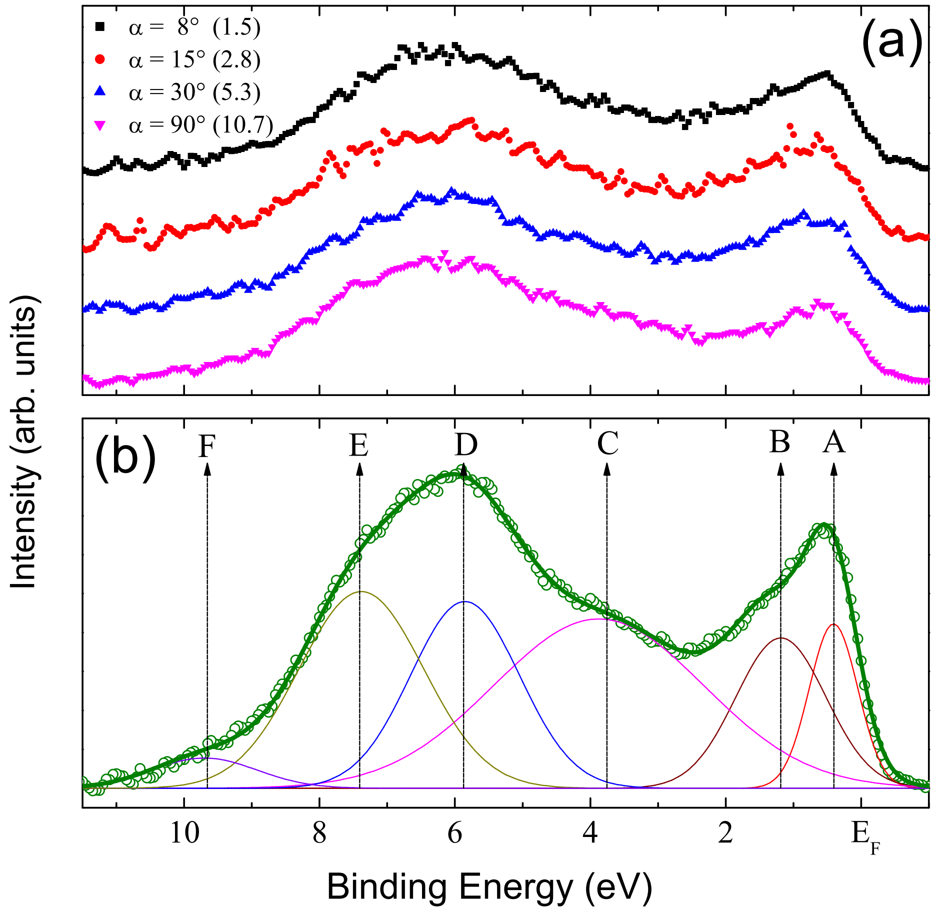

Figure 5.4 (a) HAXPES ($h\nu = 3000$ eV) spectra of $SrRuO_3$ thin film measured at different emission angles. The values in brackets are the photoelectron escape depths in MLs. (b) Fitted cumulative spectrum. Open circles correspond to the raw data, the thick line is the spectral envelope, and thin lines represent the spectral components [183].

with Ru $4d$/O $2p$ cross-section ratio of ~1.1 ($h\nu_{\mathrm{on}}$) and ~2.5 ($h\nu_{\mathrm{off}}$) [192]. In fact, HAXPES measurements provide a qualitative picture of Ru $4d$ PSW at low (< 2 eV) binding energies where Ru $4d$ states occupy the largest part of valence band. Further from E_{F}, O $2p$ contribution cannot be neglected, since theoretical calculations show that the intensity of O $2p$ states substantially increases compared to the intensity of Ru $4d$ states.

The approximate bulk and surface components of the Ru $4d$ band were obtained by subtracting O $2p$ contribution which was distinguished as peak C in Figure 5.4(b). The extracted Ru $4d$ spectrum was normalized to the integrated intensity and is shown in Figure 5.5(a). It is widely believed that coherent feature at ~0.4 eV corresponds to the delocalized DOS reproduced by DFT calculations, whereas incoherent feature at ~1.2 eV should be attributed to the presence of lo-

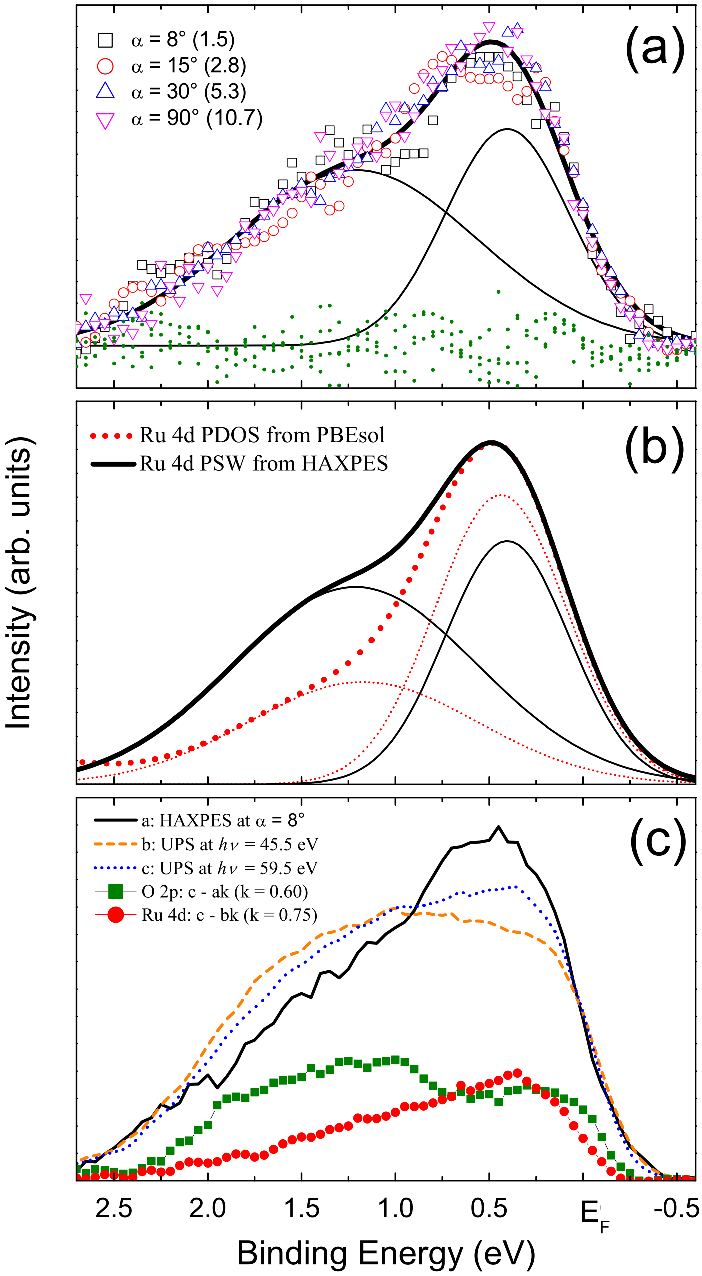

Figure 5.5 The dominant Ru 4*d* region: (a) Ru 4*d* PSW from HAXPES spectra after the subtraction of the O 2*p* contribution from higher binding energy states. The values in brackets are the photoelectron escape depths in MLs. Open symbols correspond to the raw data, the thick line is the spectral envelope, thin lines are the spectral components, and points are the residuals. (b) A comparison of Ru 4*d* PDOS from PBEsol calculations with Ru 4*d* PSW from HAXPES spectra. Thick and thin lines represent the experimental spectral envelope and components, while large and small dots stand for theoretical spectral envelope and components, respectively. (c) A comparison of normalized UPS spectra obtained at on-resonance ($h\nu = 59.5$ eV) and off-resonance ($h\nu = 44.5$ eV) conditions with HAXPES spectrum measured at grazing emission ($\alpha = 8°$). Squares correspond to the appropriately weighted difference between on-resonance and HAXPES spectra, whereas circles to the difference between on-resonance and off-resonance spectra. k is the weighting factor used in the estimation [183].

calized electronic states and requires beyond-DFT techniques. According to previously expressed assumptions on the electronic structure at the surface [186,189],[10] one may also expect the increase of the incoherent component with decreasing photoelectron escape depth. However, we demonstrate that the shape of Ru 4*d* band is actually independent of the emission angle. This result provides a strong proof that contribution from the coherent and incoherent features does not vary with increasing photoelectron escape depth L from ∼1.5 MLs ($\alpha = 8°$) to ∼10.7 MLs ($\alpha = 90°$).[11] Moreover, the incoherent component manifests itself as a shoulder rather than a separate feature.

It is somewhat surprising, since in the literature one can find some evidence that bulk and surface components deduced from the angle and $h\nu$ dependences of the PES spectra significantly differ, with incoherent states dominating at the surface [185–189]. Our results show that low emission angle ($L \approx 1.5$ MLs) HAXPES spectra represent the bulk electronic structure ($L \approx 10.7$ MLs) of $SrRuO_3$, with coherent Ru 4*d* states remaining dominant at the surface. Besides, these spectra are in a good agreement with Ru 4*d* PSW obtained from more surface-sensitive[12] resonant UPS measurements (see inset in Figure 5.3). The following findings apparently suppress the relative importance of localized surface states as naturally occurring ones.

It is worthwhile to mention that despite the absence of incoherent feature in DFT results, the asymmetric shape of coherent feature may provide some contribution to the Ru 4*d* PSW in the vicinity of incoherent peak. A direct comparison between theoretical Ru 4*d* PDOS with the experimental Ru 4*d* PSW, given in Figure 5.5(b), demonstrates that although the strongly correlated states are not present in DFT calculations, significantly broad component (∼40% of total intensity) arises in the Ru 4*d* PDOS at binding energy corresponding the reported data of incoherent peak position [31,37,185].

Even more importantly, O 2*p* states provide a finite contribution to the theoretical spectrum even in the region dominated by Ru 4*d* electrons (see Figure

---

[10] In short, the electronic structure at the surface might be affected by the absence of periodicity, different symmetry, and various defects.

[11] Actually, in [183] we confirm that the same trend holds for HAXPES spectra at $h\nu = 4500$ eV where L increases up to ∼15 MLs.

[12] For instance, for $h\nu_{on}$ the largest photoelectron escape depth is $L \approx 2$ MLs [191].

5.2), thus some admixture of O 2*p* states should also be visible in the experiments. Figure 5.5(c) illustrates the significance of this effect on Ru 4*d* spectra obtained at particularly different photon energies which are characterized by a very close escape depth.

As it was already mentioned, an increase in intensity around ∼1.2 eV with decreasing photon energy is usually explained in terms of different surface and bulk electronic structure [185–188]. In our case, however, both resonant UPS and HAXPES spectra presented in Figure 5.5(c) were obtained from approximately the same depth of the sample reaching no more than ∼2 MLs. The apparent difference in the spectra cannot be attributed to the localized Ru 4*d* surface states and should be related with a finite contribution from O 2*p* states, since an increase in $h\nu$ causes the growth of not only the escape depth, but also of Ru 4*d*/O 2*p* photoionization cross-section ratio. The difference between on-resonance and high-energy spectra provides a qualitative picture of O 2*p* PSW in dominant Ru 4*d* region, in agreement with data presented in [31, 184]. We would like to stress that the obtained O 2*p* PSW possesses a maximum at ∼1.2 eV which corresponds to the location of incoherent feature. In the meantime, the difference between on-resonance and off-resonance spectra provides approximate Ru 4*d* PSW which fairly well matches our DFT calculations in Figure 5.2. For all these reasons, it can be stated that both the finite admixture of O 2*p* states in the dominant Ru 4*d* region and the asymmetric shape of coherent Ru 4*d* feature, also obtained in previous theoretical studies [32, 37, 181, 182], may contribute to experimentally observed incoherent feature as a broad shoulder at 1.2–1.5 eV.

5.3 Introduction of Vacancies

A good agreement between theoretical, UPS, and HAXPES spectra allows us to conclude that $SrRuO_3$ is a weakly correlated material. By claiming this, we continue our efforts in trying to understand what can possibly induce the change of the degree of electron correlation in $SrRuO_3$. As it was summarized in [23], the question of correlation effects can be related to the systematic investigation of the influence of thin film thickness, strain, and stoichiometry. Indeed, it appears that the electronic structure of $SrRuO_3$ highly depends on thin film thickness with the sharp peak in the vicinity of the Fermi level occurring only at the sample thickness of 15 MLs [190]. What is more, the increase in tensile strain forces a thin film to undergo a room temperature phase transition strongly affecting the electronic and magnetic properties of $SrRuO_3$ [194]. It is equally important to point out that the intensity of the coherent peak is much more pronounced in stoichiometric specimens compared to non-stoichiometric ones [35] and that the electronic behaviour of $SrRuO_3$ thin films might be influenced by defects formed during film deposition process [37].

As vacancies and their complexes — the dominant point defects in most perovskites — are directly related to the variation in stoichiometry, we are concentrating on this line of investigation from both theoretical as well as experimental point of view. According to the scheme suggested in [195], experimentally vacancies might be introduced by annealing the air-exposed samples at moderate temperatures, since this process causes the desorption of SrO, Ru, O_2, and CO_2. The comparison between UPS measurements of the annealed specimens and theoretical calculations of non-stoichiometric $SrRuO_3$ seems to be promising for providing important insights on the nature of correlation effects in $SrRuO_3$.

A set of $SrRuO_3$ thin film valence band spectra measured after the appliance of annealing and sputtering treatment is shown in Figure 5.6. All spectra were normalized to the intensity of contaminant carbon monoxide peak centred at $\sim$10 eV. It should be also noted that the first spectrum from the annealing series is already presented in Figure 5.3, since $SrRuO_3$ was heated at 200 °C for the cleaning of the surface.

By comparing all of the spectra given in Figure 5.3 and Figure 5.6(a)–(c), one can clearly notice that the sharpness of the feature in the vicinity of E_F gradually decreases with increasing annealing temperature, qualitatively indicating that the intensity of the coherent peak at E_F decreases with increasing deviation in stoichiometry [195]. It is also seen that the decrease of the coherent feature is accompanied by the formation of the broad structure at higher binding energies around the incoherent peak position. The shape of valence band spectra drastically changes after Ar^+ sputtering [see Figure 5.6(d)] revealing the radi-

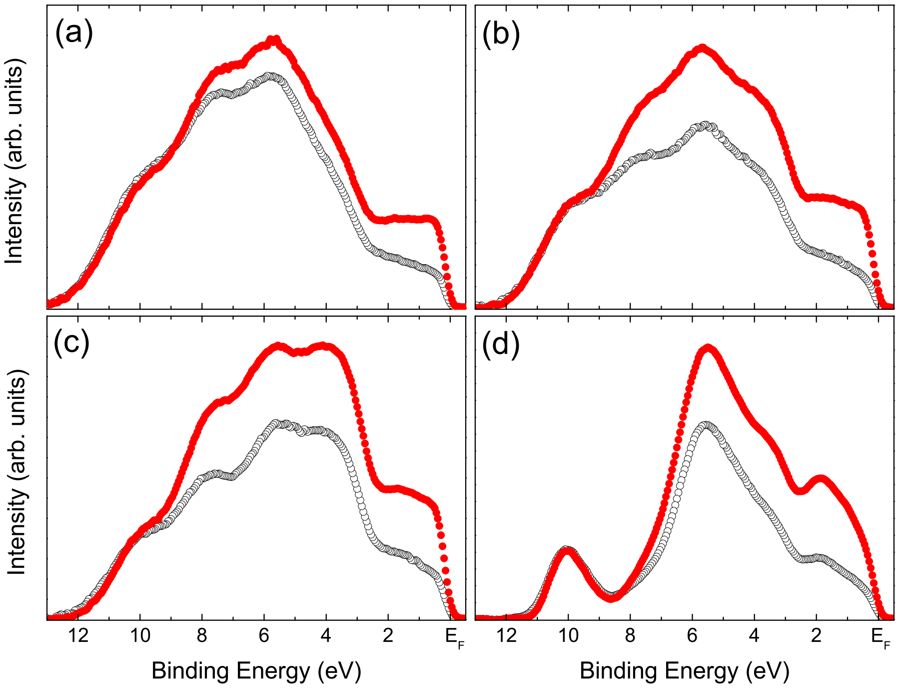

Figure 5.6 UPS spectra of $SrRuO_3$ thin film measured at Ru $4p \rightarrow 4d$ on-resonance ($h\nu = 59.5$ eV, filled circles) and off-resonance ($h\nu = 45.5$ eV, open circles) conditions after annealing in ultra-high vacuum at (a) 250 °C, (b) 300 °C, (c) 400 °C, and (d) argon sputtering [196].

cal reconstruction of the electronic structure at the surface. These results agree with the measurements in [35], where ruthenium-poor samples have exhibited a strongly pronounced spectral weight at 1.5 eV. Although it may seem that Ru vacancies can also be responsible for the spectral weight transfer in our UPS spectra, a few issues must be clarified before drawing such conclusions. On one hand, in [35] Ru-deficient specimens were intentionally grown, whereas in this work vacancies were introduced into stoichiometric $SrRuO_3$ by annealing and sputtering thus simulating the possible cleaning process. On the other hand, the formation of oxygen vacancies cannot be distinguished from the formation of ruthenium vacancies on the basis of lattice constants only [23], as it was done in [35]. Thus, it is obvious that due to the different experimental settings and possibly important role of oxygen vacancies one should turn to the theoretical modelling.

Theoretically, vacancies can be introduced by removing appropriate atoms or their combinations from stoichiometric $SrRuO_3$. According to [195], the heating of samples at moderate temperatures (300–500 °C) causes the desorption[13] of SrO,

---

[13] This process may also begin at somewhat lower temperatures.

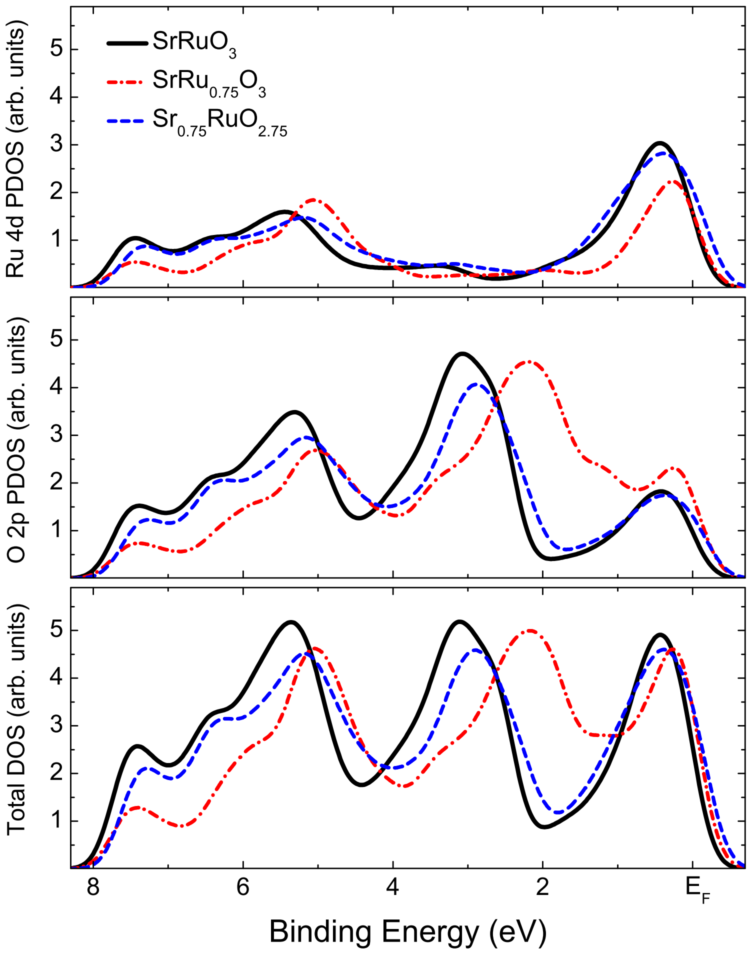

Figure 5.7 The total and projected DOS of $SrRuO_3$ after removal of Ru and SrO atoms from the unit cell. The calculations were performed without full relaxation of geometry using PBEsol exchange-correlation functional.

Ru, and O_2 which in turn leads to the decomposition of surface layers. However, experimental observations reveal that the initial and relatively small desorption of SrO and Ru starts only at ∼350 °C, while in our UPS spectra the shift in spectral weight is already seen at ∼250 °C. It apparently indicates that oxygen vacancies are preferentially formed under annealing of the samples. And indeed, our initial DFT calculations, shown in Figure 5.7, demonstrate that the removal of SrO atoms has rather quantitative than qualitative influence on the DOS of $SrRuO_3$. The introduction of Ru vacancies, on the other hand, results in a strongly pronounced spectral weight transfer of O $2p$ states towards the incoherent peak position. Although the following finding corresponds to the tendency seen for the raw spectra of Ru-deficient samples [35], one should notice that the intensity of Ru $4d$ gets lower without any redistribution of the spectral weight in E_F–2 eV region.

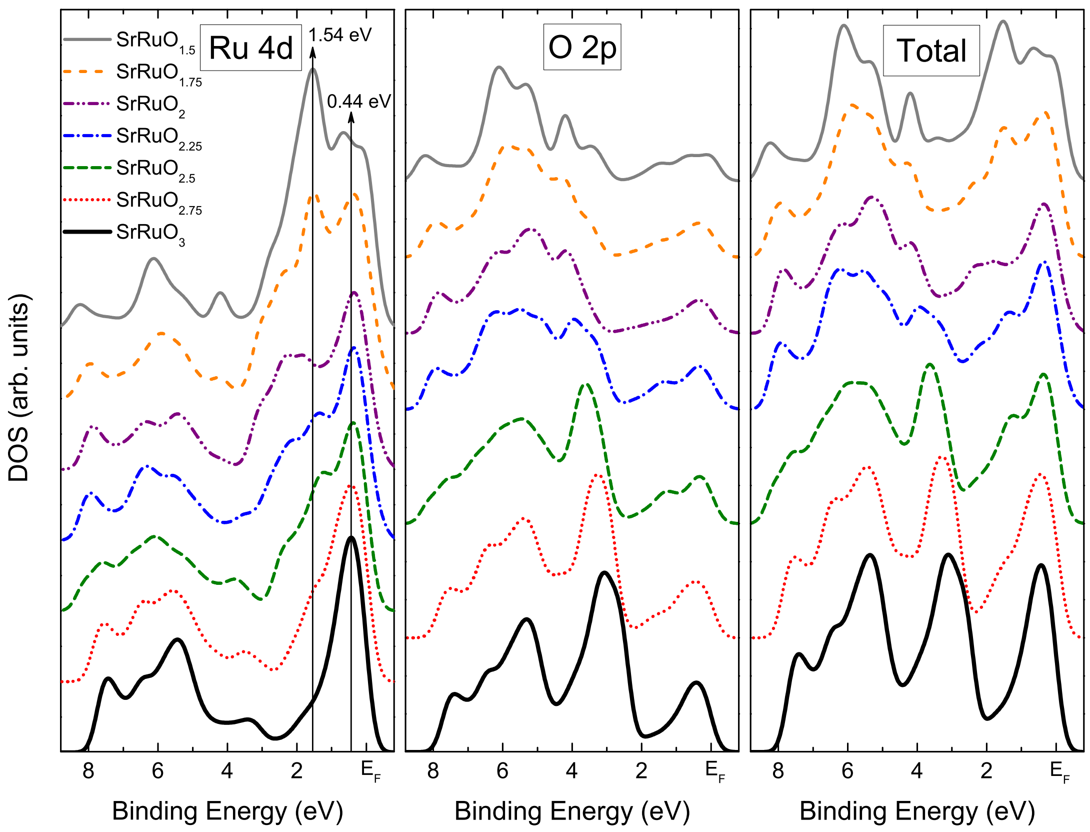

Figure 5.8 The total and projected DOS of $SrRuO_3$ after removal of O_x ($x = 1$–6) atoms from the unit cell. The calculations were performed with full relaxation of geometry using PBEsol exchange-correlation functional.

This contradicts to the variation of the on-resonance UPS spectra [see Figure 5.3 and Figure 5.6(a)–(c)], where a shift in the spectral weight can be directly related to the Ru 4*d* states, and thereby confirms the idea that more focus should be given to the oxygen vacancies.

The total and projected DOS of oxygen-deficient $SrRuO_3$ are presented in Figure 5.8. It is worthwhile to mention that the change in stoichiometry from $SrRuO_3$ to $SrRuO_{1.5}$ is realistic, since one can find experimental evidence that under annealing the original chemical composition can reduce to Sr:Ru:O=1:1:2 [195]. The most important aspect revealed in Figure 5.8 is, of course, a clearly expressed spectral weight transfer in Ru 4*d* PDOS which results in an increasing contribution of the incoherent peak as the stoichiometry of $SrRuO_3$ decreases. The initial complete dominance of the coherent peak at 0.44 eV gradually turns into the distinctly pronounced dominance of the incoherent feature at 1.54 eV. Besides, this transformation is accompanied by the reduction of the Ru 4*d* states at 4–8 eV as well as by the suppression of the O 2*p* states at E_F–4 eV. It is interesting that the following spectral weight transfer scenario is perfectly consistent with the UPS measurements shown in Figure 5.3 and Figure 5.6(a)–(c). This fact provides a strong proof that experimentally observed incoherent feature rises not due to the manifestation of strong electron correlation in stoichiometric specimens, as previously thought, but due to the redistribution of electronic states caused by the introduction of oxygen vacancies during the cleaning or/and growth of the samples.[14] Therefore, it becomes obvious why none of the previous *ex situ* specimens [31–33, 184–187] have exhibited a clear peak at the Fermi level in UPS measurements, in contrast to *in situ* ones [34, 35]. The effect of scraping the polycrystal surface, demonstrated in [34], shows a very close resemblance to the effect of annealing at moderate temperatures, revealed in our UPS spectra and DOS representations. All these findings allow us to conclude that $SrRuO_3$ is a weakly correlated material and its artificially affected surface states should not be related with the natural internal electronic structure. Besides, our conclusions are strengthened by several very recent studies on magnetic properties and momentum-resolved electronic structure [24,197] that also confirm the weakly correlated nature of $SrRuO_3$.

5.4 Elastic Properties

Due to the lack of experimental as well as theoretical data, we can only make a comparison between our own elastic constants obtained within different DFT approaches. Tables 5.2, 5.3, and 5.4 represent the calculated elastic constants and other parameters for cubic, tetragonal, and orthorhombic $SrRuO_3$, respectively. The tendency that can be seen is opposite to the one found for the lattice constants. In this case, LDA gives the highest, whereas PBE gives the lowest values of $C_{\alpha\beta}$ for all phases of $SrRuO_3$. The revised functionals perform quite similarly giving values that fall between the range determined by LDA and PBE. This result once more confirms that such quantities as elastic constants and polycrystalline moduli crucially depend on reliable evaluation of the lattice parameters.

---

[14] Note that although [35] points out the importance of ruthenium vacancies, this issue requires a further study to find out the amount of oxygen vacancies that might have been introduced in the experiment and the role of full geometry relaxation in the theoretical calculations.

Table 5.2 Equilibrium lattice constant a (in Å), elastic constants $C_{\alpha\beta}$ (in GPa), bulk modulus B (in GPa) from VRH approximation, bulk modulus B_{BM} (in GPa) and its pressure derivative B'_{BM} from BM equation of state, shear modulus G (in GPa), Young's modulus Y (in GPa), Poisson's ratio ν, longitudinal sound velocity v_{L} (in m/s), transverse sound velocity v_{T} (in m/s), average sound velocity $\bar{v}$ (in m/s), and Debye temperature θ_{D} (in K) calculated and compared to the available experimental data for cubic $\mathrm{SrRuO_3}$.

	LDA	SOGGA	$\mathrm{PBEsol^{PBE}}$	PBEsol	WC	PBE	Expt.
a	3.900	3.924	3.926	3.933	3.936	3.982	3.955[a], 3.974[b]
C_{11}	240.2	210.3	208.7	205.4	205.6	176.9	
C_{12}	204.6	194.6	193.2	192.9	190.2	176.6	
C_{44}	76.1	73.8	73.7	73.4	73.1	70.9	
B	216.5	199.8	198.4	197.1	195.3	176.8	
B_{BM}	215.9	198.9	197.6	196.3	196.2	176.5	
B'_{BM}	4.55	4.26	4.30	4.34	4.58	4.41	
G	42.9	32.1	32.0	30.2	31.8	21.1	
Y	120.6	91.6	91.2	86.2	90.4	60.7	
ν	0.407	0.424	0.423	0.427	0.423	0.443	
v_{L}	6415	6095	6082	6047	6058	5724	
v_{T}	2539	2219	2217	2157	2215	1835	
$\bar{v}$	2877	2520	2518	2451	2515	2089	
θ_{D}	375.5	326.9	326.3	317.2	325.4	267.1	

[a]From [40] at 973 K.
[b]From [178] at 1082 K.

The comparison between tetragonal and orthorhombic phases indicates that $C_{11}^{\mathrm{Tetr.}} = C_{22}^{\mathrm{Tetr.}} < C_{33}^{\mathrm{Tetr.}}$ and $C_{22}^{\mathrm{Orth.}} < C_{11}^{\mathrm{Orth.}} < C_{33}^{\mathrm{Orth.}}$. As C_{11}, C_{22}, and C_{33} are directly associated with the changes in the lattice along the x, y, and z axis, respectively, one can conclude that atomic bonding along the z axis is stronger than that along the x or y axis for both phases of $\mathrm{SrRuO_3}$. Smaller values of C_{44} and C_{55} compared to C_{66} mean that lattice is more easily deformed by a pure shear around the x or y axis in comparison to the z axis. Since bulk modulus B is essentially a special case of elastic constant and can be treated as a measure of the average bond strength, it is interesting to note that all three phases exhibit a very close value of it. This means that polycrystalline $\mathrm{SrRuO_3}$ retains its level of compressibility throughout a variety of geometric configurations. The fact that the largest discrepancy between the bulk moduli obtained using VRH approximation and BM equation of state does not exceed ∼3% demonstrates the reliability of performed calculations. Unlike the bulk modulus, shear and Young's moduli, which correspondingly describe the resistance of a material against the shear and

Table 5.3 Equilibrium lattice constants a and c (in Å), elastic constants $C_{\alpha\beta}$ (in GPa), bulk modulus B (in GPa) from VRH approximation, bulk modulus B_{BM} (in GPa) and its pressure derivative B'_{BM} from BM equation of state, shear modulus G (in GPa), Young's modulus Y (in GPa), Poisson's ratio ν, longitudinal sound velocity v_{L} (in m/s), transverse sound velocity v_{T} (in m/s), average sound velocity $\bar{v}$ (in m/s), and Debye temperature θ_{D} (in K) calculated and compared to the available experimental data for tetragonal $SrRuO_3$.

	LDA	SOGGA	PBEsol$^{\mathrm{PBE}}$	PBEsol	WC	PBE	Expt.
a	5.513	5.554	5.557	5.570	5.572	5.656	5.578[a], 5.589[b]
c	7.773	7.801	7.805	7.813	7.820	7.872	7.908[a], 7.917[b]
C_{11}	268.9	250.5	249.1	246.7	245.8	223.8	
C_{12}	146.7	132.9	131.8	129.9	129.7	110.6	
C_{13}	185.9	172.4	171.9	170.7	170.6	151.9	
C_{33}	343.8	325.1	322.6	321.7	321.1	299.9	
C_{44}[c]	71.6	68.8	68.7	68.8	68.6	65.7	
C_{66}	99.4	91.1	90.3	88.1	87.7	75.6	
B	209.2	193.7	192.7	190.9	190.5	170.5	
B_{BM}	205.1	189.4	187.9	186.2	185.8	165.3	
B'_{BM}	4.83	4.89	4.81	4.82	4.85	5.19	
G	71.2	67.7	67.3	66.8	66.5	62.8	
Y	191.9	181.9	180.8	179.6	178.8	167.7	
ν	0.347	0.344	0.344	0.343	0.344	0.336	
v_{L}	6746	6579	6566	6556	6553	6367	
v_{T}	3265	3212	3205	3203	3199	3164	
$\bar{v}$	3669	3608	3600	3598	3594	3551	
θ_{D}	479.6	468.8	467.4	466.4	465.5	454.3	

[a] From [40] at 823 K.
[b] From [178] at 894 K.
[c] Calculated within a range of strains δ from -0.0003 to 0.0003.

uniaxial deformations, have significantly lower values for cubic $SrRuO_3$ compared to the tetragonal and orthorhombic phases. Due to the interdependence between the polycrystalline parameters, the opposite tendency holds for Poisson's ratio which in turn defines the lateral structural deformation when material is stretched or compressed. For high-temperature cubic $SrRuO_3$, the average value of ν is $\sim$0.42, whereas low-temperature orthorhombic $SrRuO_3$ exhibits $\sim$0.34 which is a common value for most of the metals. Lower shear modulus for cubic $SrRuO_3$ also points to lower hardness and hence the decreased resistance against plastic deformation. Despite that, a high B/G ratio is inherent for all three phases of $SrRuO_3$ revealing that this material behaves in a ductile manner. The most common critical value that separates ductile and brittle nature was established in [198]: if $B/G > 1.75$, the material behaves in a ductile manner, otherwise,

Table 5.4 Elastic constants $C_{\alpha\beta}$ (in GPa), bulk modulus B (in GPa) from VRH approximation, bulk modulus B_{BM} (in GPa) and its pressure derivative B'_{BM} from BM equation of state, shear modulus G (in GPa), Young's modulus Y (in GPa), Poisson's ratio ν, longitudinal sound velocity v_{L} (in m/s), transverse sound velocity v_{T} (in m/s), average sound velocity $\bar{v}$ (in m/s), and Debye temperature θ_{D} (in K) calculated and compared to the available experimental data for orthorhombic $SrRuO_3$.

	LDA	SOGGA	$\mathrm{PBEsol}^{\mathrm{PBE}}$	PBEsol	WC	PBE	Expt.
C_{11}	306.9	286.9	285.2	284.8	284.2	260.1	
C_{12}	186.7	171.1	169.5	167.9	167.8	143.4	
C_{13}	156.2	145.1	144.4	143.6	143.4	128.2	
C_{22}	274.5	256.9	255.6	253.9	252.7	230.1	
C_{23}	147.7	139.8	139.1	138.3	137.9	125.9	
C_{33}	338.6	312.6	310.8	307.3	306.8	272.1	
C_{44}[a]	72.7	71.4	71.9	72.2	72.4	71.1	
C_{55}	67.7	66.4	66.4	66.7	66.7	65.9	
C_{66}	88.1	80.9	80.1	78.7	78.4	67.3	
B	210.8	196.1	194.9	193.6	193.1	172.7	
B_{BM}	210.5	195.9	194.4	192.8	192.5	172.8	192.3[b]
B'_{BM}	4.75	4.64	4.67	4.65	4.66	4.69	5.03[b]
G	72.8	69.3	69.1	68.9	68.7	64.6	60.1[c]
Y	195.8	185.9	185.4	184.7	184.3	172.3	161[c]
ν	0.345	0.342	0.341	0.341	0.341	0.334	
v_{L}	6782	6625	6614	6613	6612	6416	6312[c]
v_{T}	3298	3246	3246	3249	3248	3206	3083[c]
$\bar{v}$	3706	3646	3645	3648	3648	3596	
θ_{D}	484.5	472.8	473.5	473.1	472.7	460.6	448[c], 457[d]

[a] Calculated within a range of strains δ from -0.015 to 0.015.
[b] From [46] at room temperature.
[c] From [44] at room temperature.
[d] From [45] by applying fitting in the temperature range of 163–300 K.

its behaviour should be associated with brittleness. Intriguingly, $SrRuO_3$ satisfies even tighter criterion of $B/G > 2.67$ proposed in [199] which in a similar fashion distinguishes ductility from brittleness. It is worth mentioning that the following result is valid for all density functionals applied in this study. The fact that cubic $SrRuO_3$ becomes softer against shear-type distortions is also reflected in the lower sound velocities and Debye temperature. In the meantime, tetragonal phase is able to retain values of polycrystalline parameters that are very close to the orthorhombic ones.

Another property that should be taken into account is elastic anisotropy. Having in mind that there is no unique method to determine the degree of this characteristic, in the first place we employ a concept introduced in [200] where the percentage anisotropy in compressibility and shear is defined as

$$A_B = \frac{B_{\mathrm{V}} - B_{\mathrm{R}}}{B_{\mathrm{V}} + B_{\mathrm{R}}} \tag{5.1}$$

and

$$A_G = \frac{G_{\mathrm{V}} - G_{\mathrm{R}}}{G_{\mathrm{V}} + G_{\mathrm{R}}}, \tag{5.2}$$

respectively. A value of zero corresponds to elastic isotropy and a value of 100% identifies the largest possible anisotropy. Within PBEsol approximation, orthorhombic phase possesses $A_B \approx 0.2\%$ and $A_G \approx 1.5\%$, while tetragonal $\mathrm{SrRuO_3}$ acquires $A_B \approx 2.3\%$ and $A_G \approx 1.8\%$. This result reveals that orthorhombic and tetragonal $\mathrm{SrRuO_3}$ are similarly anisotropic in shear, whereas anisotropy in compressibility is more pronounced for the latter symmetry. On the whole, the values of anisotropic factors show that orthorhombic and tetragonal phases can be considered as weakly elastically anisotropic. However, completely different situation emerges for cubic $\mathrm{SrRuO_3}$. Although in this case isotropy in compressibility is assured by $B_{\mathrm{V}} = B_{\mathrm{R}}$, a very large value of $A_G \approx 54\%$ indicates a high degree of anisotropy in shear. It in turn means that cubic phase can be considered as highly elastically anisotropic. The following conclusions are also confirmed by estimation of universal elastic anisotropy index

$$A^U = 5\frac{G_{\mathrm{V}}}{G_{\mathrm{R}}} + \frac{B_{\mathrm{V}}}{B_{\mathrm{R}}} - 6 \tag{5.3}$$

proposed in [201]. In this analysis method, the departure of A^U from zero defines the extent of single-crystal anisotropy accounting for both the bulk and the shear contributions. For orthorhombic, tetragonal, and cubic $\mathrm{SrRuO_3}$, the values of A^U are ~0.16, 0.23, and 11.8, respectively, showing full compatibility with our previous findings.

Although experimental data available for orthorhombic phase of $\mathrm{SrRuO_3}$ allow to provide a few thoughts on the suitability of applied DFT approximations, the comparison between experiment and theory is not straightforward. It is because of thermal expansion which tends to reduce the elastic moduli. Therefore, one should expect the calculated parameters to be lower at room temperature. For example, the thermal effects can modify the bulk modulus by about 5–15% for various metals [85]. Besides, one should also remember that uncertainties in experimental bulk moduli are much greater than in lattice constants and can easily be as large as 10% [88]. By taking into account all these considerations, we can conclude that overall our calculated polycrystalline parameters demonstrate a good agreement with available experimental data. Yet, it is not easy to say which of the particular functionals perform best. The general trend observed for the lattice constants of orthorhombic $SrRuO_3$ suggests that it is very likely that revised functionals may yield the closest values to the possible low-temperature experiment, while LDA and PBE may show a slight overestimation and underestimation, respectively.

5.5 Mechanical Stability

Concerning the mechanical stability of $SrRuO_3$, a few issues were observed. Firstly, our C_{44} calculations for tetragonal structure show that strains δ taken in steps of 0.005 from -0.03 to 0.03 induce internal forces that drive lattice to the energetically lower states compared to the unstrained crystal (see Figure 5.9). Neither different DFT approaches, nor modification of calculation parameters have appreciable influence on this result. This basically means that tetragonal $SrRuO_3$ is mechanically unstable at zero temperature and zero pressure[15] in spite of the fact that remaining $C_{\alpha\beta}$ satisfy all the stability conditions given by (3.12). In other words, under ordinary C_{44} related deformation a more stable monoclinic structure emerges resulting in a negative value of C_{44} which in turn characterizes a pure shear instability. The structural transformation which could be related to the unusual behaviour of tetragonal $SrRuO_3$ is revealed in Figure 5.10(a). Here, it is seen that the evolution of tilting and rotation angles demonstrates a sharp discontinuity at the very first step of strain (from 0 to $-0.005/0.005$), while further steps (from $-0.005/0.005$ to $-0.03/0.03$) are fully uniform. If one would take into consideration that Ru-O bond lengths O-Ru-O bond angles show quite small

---

[15] Pressure is an important parameter in the Gibbs free energy, since it can compensate for the mechanical instability at zero temperature. The minimization of the Gibbs free energy in turn determines the lattice structure of a crystalline material in thermal equilibrium at ambient conditions.

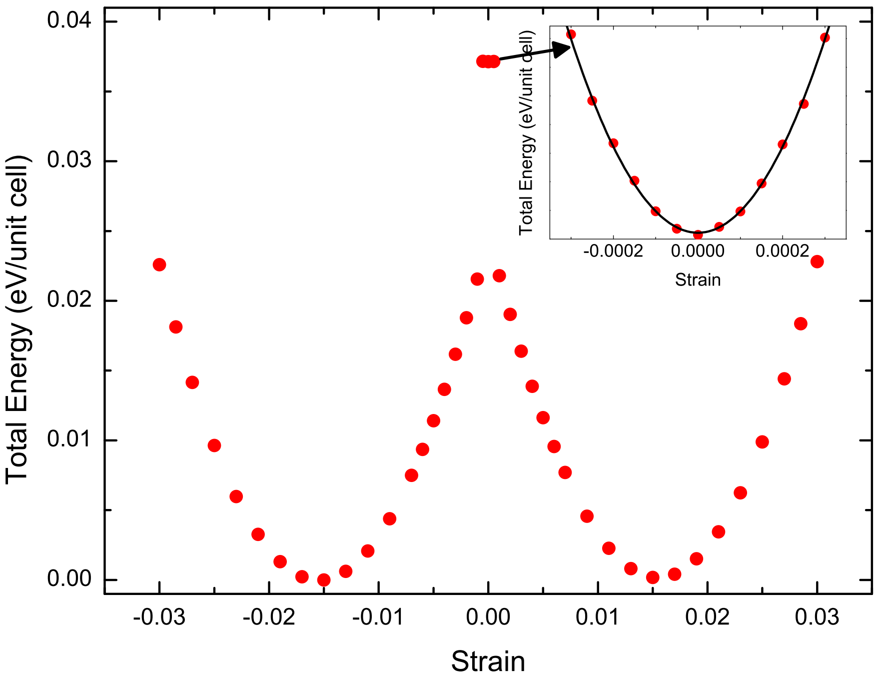

Figure 5.9 Total energy of ground-state tetragonal $SrRuO_3$ as a function of strain under C_{44} related shear deformation. The inset demonstrates the usual parabolic behaviour when magnitude of applied strains is reduced from -0.0003 to 0.0003. The calculations were performed using PBEsol exchange-correlation functional.

variations in magnitude at the discontinuity,[16] it becomes obvious that under C_{44} related shear deformation tetragonal $SrRuO_6$ undergoes a strong reorientation of RuO_6 octahedra. And indeed, the following abrupt reorientation around x and z axes is clearly visualized in Figure 5.10(b): ϕ decreases by $\sim$20 degrees, whereas θ increases by $\sim$8 degrees. Needless to say, no similar behaviour was observed for any of the remaining $C_{\alpha\beta}$ related deformations.

Actually, the finding of mechanical instability is in agreement with the fact that bulk samples of tetragonal phase have not been experimentally observed at low temperatures. Yet, it is worth to note that room-temperature stabilized tetragonal $SrRuO_3$ has been successfully obtained by tensile strain when grown as thin film on various substrates [47–49]. We would like to emphasize that these results are not in contradiction with our data, since the stability of thin film is determined by different factors compared to the bulk specimens [202].[17]

By remembering that the elastic energy, written as quadratic term in (3.10),

---

[16] See Figures D.1 and D.2 in Appendix D.

[17] However, a question of what exactly makes the tetragonal phase experimentally observable at high temperatures requires a separate investigation, therefore this interesting issue lies outside the scope of the present study

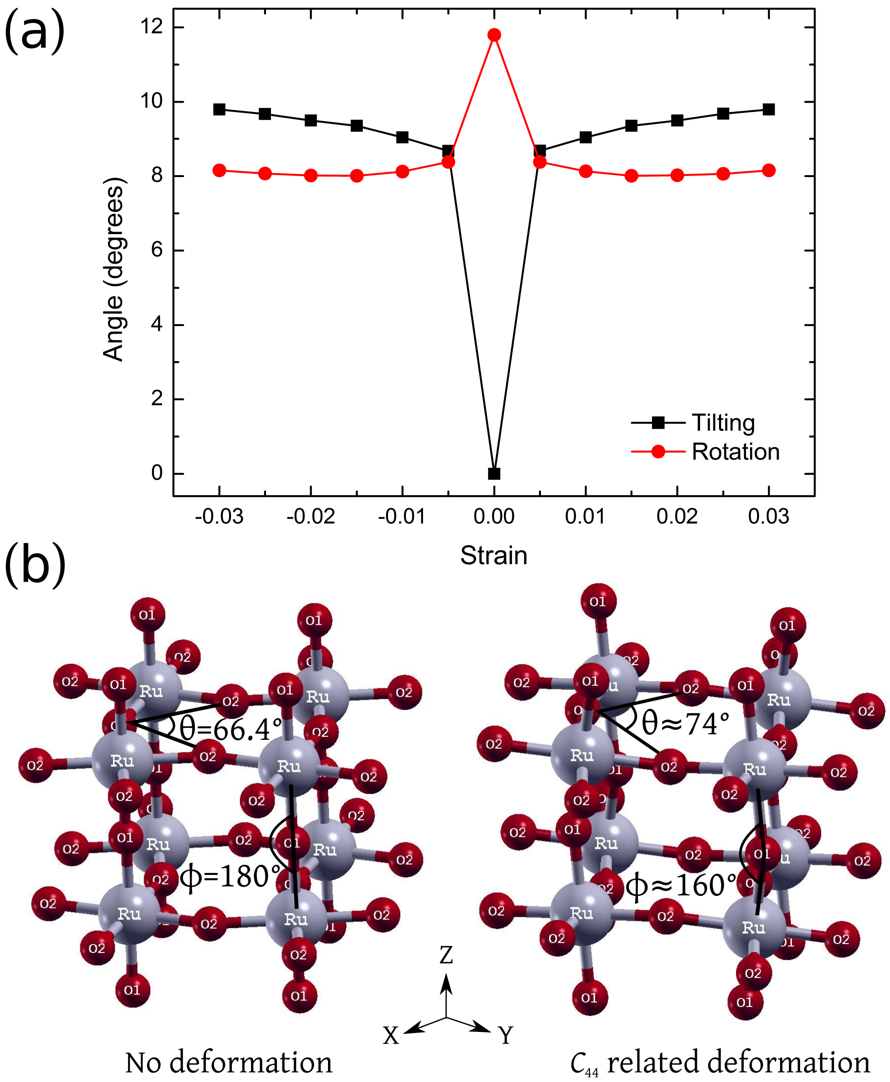

Figure 5.10 Tetragonal $SrRuO_3$: (a) the evolution of tilting and rotation angles as a function of strain under C_{44} related shear deformation and (b) schematic representation of RuO_6 octahedra network at its ground state and under C_{44} related shear deformation. In case of the latter, angles ϕ and θ are approximated, since after structural transformation the dependence of strain becomes relatively weak. The calculations were performed using PBEsol exchange-correlation functional.

must be positive definite under any arbitrary but small deformations, we were curious to find out whether the limit at which the system can be described by the usual parabolic behaviour exists. For this purpose, we had to narrow the range of the applied strains and to tighten the convergence criteria. The first attempt to reduce the magnitude of the applied strains from -0.003 to 0.003 was not successful, since the total energy of the strained lattice was still lower than that of the unstrained one. However, the second attempt in which the magnitude of the applied strains was lowered from -0.0003 to 0.0003 appeared to be fruitful (see inset in Figure 5.9). Certainly, in the first place we wanted to make sure that such calculations with very small changes in the total energy were not overpowered by numerical fluctuations and thus could be treated seriously. For a comparison, we tried to evaluate C_{44} without the geometry optimization[18] by varying δ from -0.03 to 0.03 and from -0.0003 to 0.0003. The obtained results for PBEsol revealed that in both cases the values of C_{44} were very close to each other: 85.6 against 86.3 GPa, respectively. Despite this correspondence, it is evident that in reality even at temperatures very close to 0 K zero-point fluctuations have a larger impact on atomic positions than such tiny strains. But since in DFT framework nuclei of the atoms form a perfectly static lattice, even the smallest atomic displacements in the system can be treated as reflecting its unique response to deformation. Having in mind the thorough analysis [203] in which the stability of elastic constants is attained using similarly small deformations, the values of C_{44} presented in Table 5.3 should provide realistic information on properties of tetragonal $SrRuO_3$. Surely, it would be particularly interesting to find out whether our results show a correspondence with the experiment or at least finite-temperature calculations.

Another issue is related to the calculation of C_{44} for the orthorhombic phase of $SrRuO_3$. The application of strains taken from the standard range[19] has revealed a distinct deviation from the initial parabolic behaviour apparently seen at strain values[20] of ±0.021 in Figure 5.11. Interestingly, the subsequent behaviour of the deformed material can be approximated by another parabola with quadratic coefficient being roughly two times smaller. It indicates that the strain-induced structural transformation causes quite substantial softening of C_{44}. The fact that the crystallographic space group of the system remained unchanged throughout the whole range of applied strains makes us firmly believe that we are dealing with isosymmetric phase transition, which is a fairly rare phenomenon for crystalline materials. In order to get a more accurate picture of isosymmetric $SrRuO_3$ behaviour, we have increased the number of strains from standard 12 to 60. A close examination of calculations showed that a small deviation from the initial parabola begins to emerge at ±0.017. Therefore, for the precise evaluation of C_{44},

---

[18] Elastic constant of the unrelaxed structure.

[19] From -0.03 to 0.03.

[20] Strain values of deviation slightly depend on the DFT approach used.

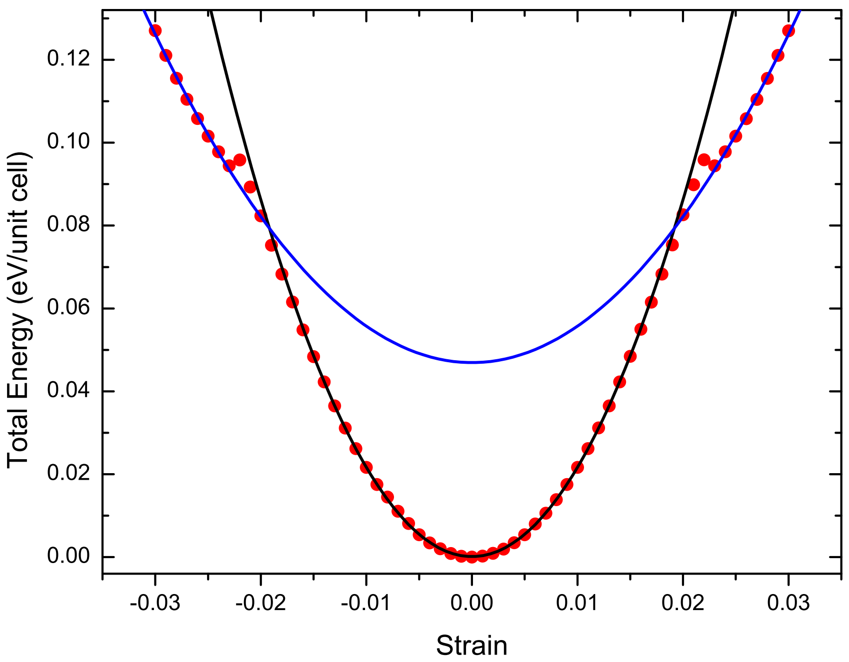

Figure 5.11 Total energy of ground-state orthorhombic $SrRuO_3$ as a function of strain under C_{44} related shear deformation. The lower parabola was obtained by polynomial fitting with magnitude of applied strains confined from -0.015 to 0.015. The upper parabola was fitted with strains falling in the range of $-0.03 \ldots -0.023$ and $0.023 \ldots 0.03$. The calculations were performed using PBEsol exchange-correlation functional.

we have confined the range of strains from -0.015 to 0.015. Thus obtained values of C_{44} are presented in Table 5.4.

Despite the unusual behaviour of orthorhombic $SrRuO_3$, the mechanical stability of this phase is beyond doubt, since all the elastic constants calculated within the standard range of strains obey the stability criteria expressed by (3.13). The same statement holds for the cubic phase of $SrRuO_3$, because its mechanical stability conditions (3.11) are also satisfied.

5.6 Shear Deformation for Orthorhombic Phase

C_{44} related shear deformation makes the orthorhombic structure of $SrRuO_3$ transform to monoclinic symmetry. This strain-induced symmetry-reduction is accompanied by the change of the number of non-equivalent Ru and O atoms. As can be seen from Figure 5.1(b), non-equivalent Ru atoms, labelled as Ru1 and Ru2, form repetitive layers perpendicular to the c or, equivalently, z axis, whilst non-equivalent O atoms, named as O1, O2, and O3, are located within the Ru-formed

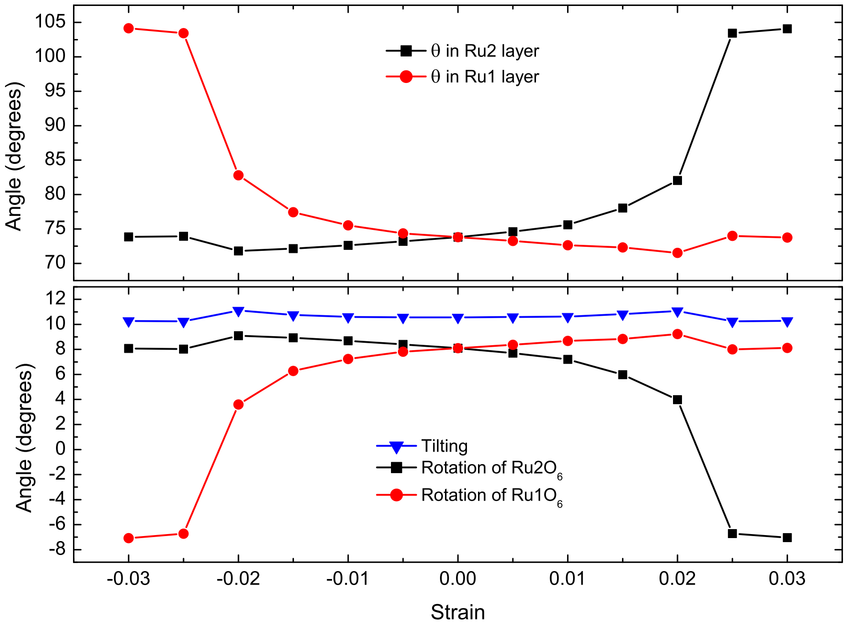

Figure 5.12 θ, tilting, and rotation angles of ground-state orthorhombic $SrRuO_3$ as a function of strain under C_{44} related shear deformation. The calculations were performed using PBEsol exchange-correlation functional.

layers (O2 and O3) or between them (O1). The following structural transformation indicates the emergence of two non-equivalent oxygen octahedra, namely, $Ru1O_6$ and $Ru2O_6$. The first one consists of a pair of O1 and four O2 atoms, whereas the second one possesses a pair of O1 and four O3 atoms. The fact that oxygen octahedra are not regular in strain-free $SrRuO_3$ [41] is also reflected in the structure of $Ru1O_6$ and $Ru2O_6$ implying that a larger set of parameters is required for the complete description of geometry of deformed $SrRuO_3$.[21] However, octahedra form a three-dimensional network, thus a change in bond length or angle in one direction necessarily restricts the allowed change in bond length or angle in other directions.

Under C_{44} related shear deformation, the evolution in internal geometry of oxygen octahedra is rather complex and it makes hard to identify the structural transformation which could be apparently linked to the extraordinary behaviour of $SrRuO_3$. On one hand, the evolution in Ru-O bond lengths shows some discontinuity but the variations of the magnitudes are rather small. On the other hand, the changes in O-Ru-O bond angles are much more pronounced but the evolution remains almost uniform throughout the whole range of strains. Fortunately, in

---

[21] See Figure 5.12 and Appendix D for details.

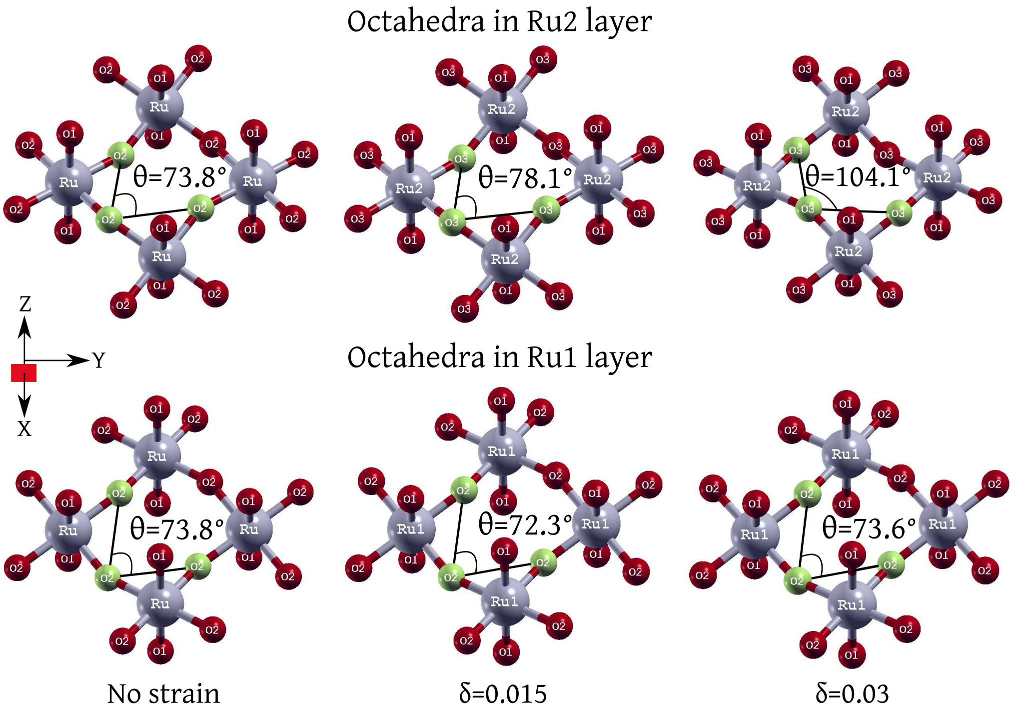

Figure 5.13 The evolution of RuO_6 octahedra rotation in Ru1 and Ru2 layers under tensile C_{44} related shear deformation within PBEsol exchange-correlation framework.

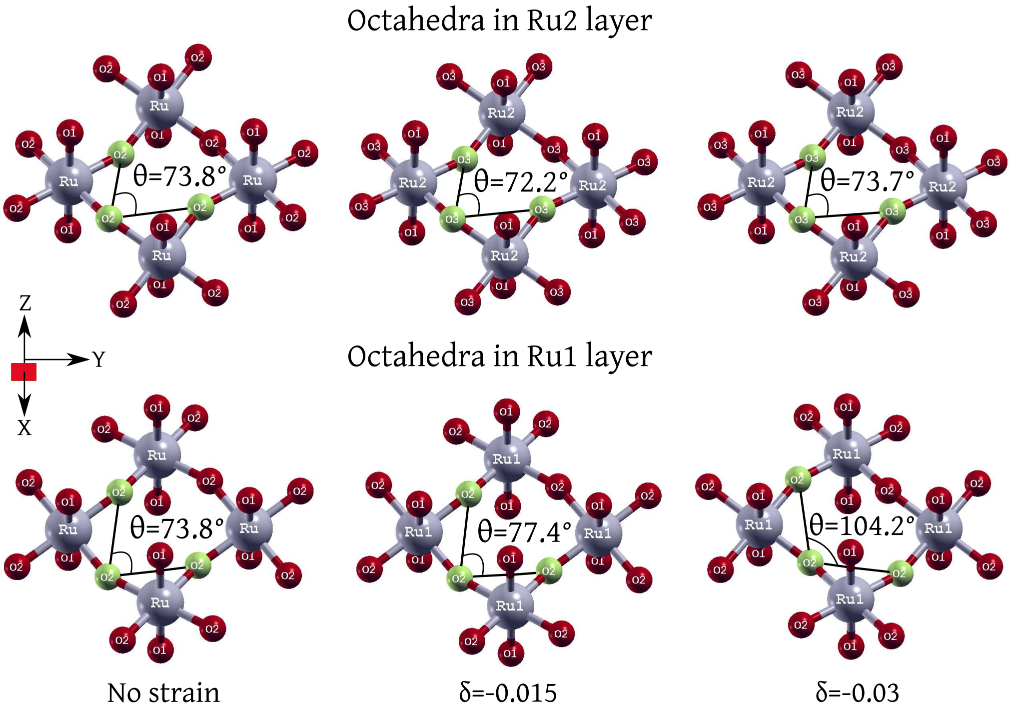

Figure 5.14 The evolution of RuO_6 octahedra rotation in Ru1 and Ru2 layers under compressive C_{44} related shear deformation within PBEsol exchange-correlation framework.

Figure 5.12 it is clearly seen that in case of tensile deformation, θ in Ru2 layer undergoes a huge increase reaching $\sim$21 degrees, while a step between two consecutive strains is only 0.005 — from 0.02 to 0.025. By taking into account that bond angle O31-Ru2-O32 remains almost unaltered,[22] it becomes evident that a significant rotation of Ru2O_6 octahedra occurs, with a change in rotation angle Θ reaching $\sim$11 degrees. In the meantime, variation in rotation of Ru1O_6 octahedra as well as tilting stays quite small compared to that of Ru2O_6. The opposite trend can be observed as the deformation becomes compressive: in this case, a significant and approximately equal in magnitude[23] rotation of Ru1O_6 octahedra occurs, while rotation of Ru2O_6 and tilting show small variations from their initial values. This evolution of octahedra rotation, clearly visualized in Figures 5.13 and 5.14, is also reflected in deviation from the initial parabola exhibited in Figure 5.11. As it was mentioned earlier, the fact that an abrupt change in $SrRuO_3$ behaviour is not accompanied by a change in crystallographic space group speaks for the manifestation of isosymmetric phase transition. Figures 5.12–5.14 allow us to point out the essential signature of this transformation — vast rotations of oxygen octahedra around z axis. Moreover, the rotation pattern manifests itself in such a way that under tension the Ru2O_6 octahedra are much more active in comparison to Ru1O_6, whereas under compression the opposite is observed. It is interesting to note that isosymmetric phase transition has been recently identified in biaxially strained $LaGaO_3$ [204], $LaNiO_3$ [205], and $BiFeO_3$ [206, 207] films. For these perovskite-structured materials, a sharp discontinuity in the magnitude of the tilting and rotation angles occurs which in turn is followed by an abrupt reorientation of the octahedra rotation axis direction. However, no similar trend was observed for biaxially strained orthorhombic $SrRuO_3$ [41], making our results even more intriguing.

In order to find out the influence the isosymmetric phase transition has on the electronic structure of $SrRuO_3$, we also include Figure 5.15 in which the total and projected DOS (FWHM=0.1 eV) at several values of strain are presented. Notation $-0.015/0.015$ and $-0.03/0.03$ indicates that $SrRuO_3$ behaviour basically

---

[22] The same is true for the bond angle O21-Ru1-O22. See Figure D.4 in Appendix D.

[23] The rotations are not exactly equal due to the finite precision of calculations.

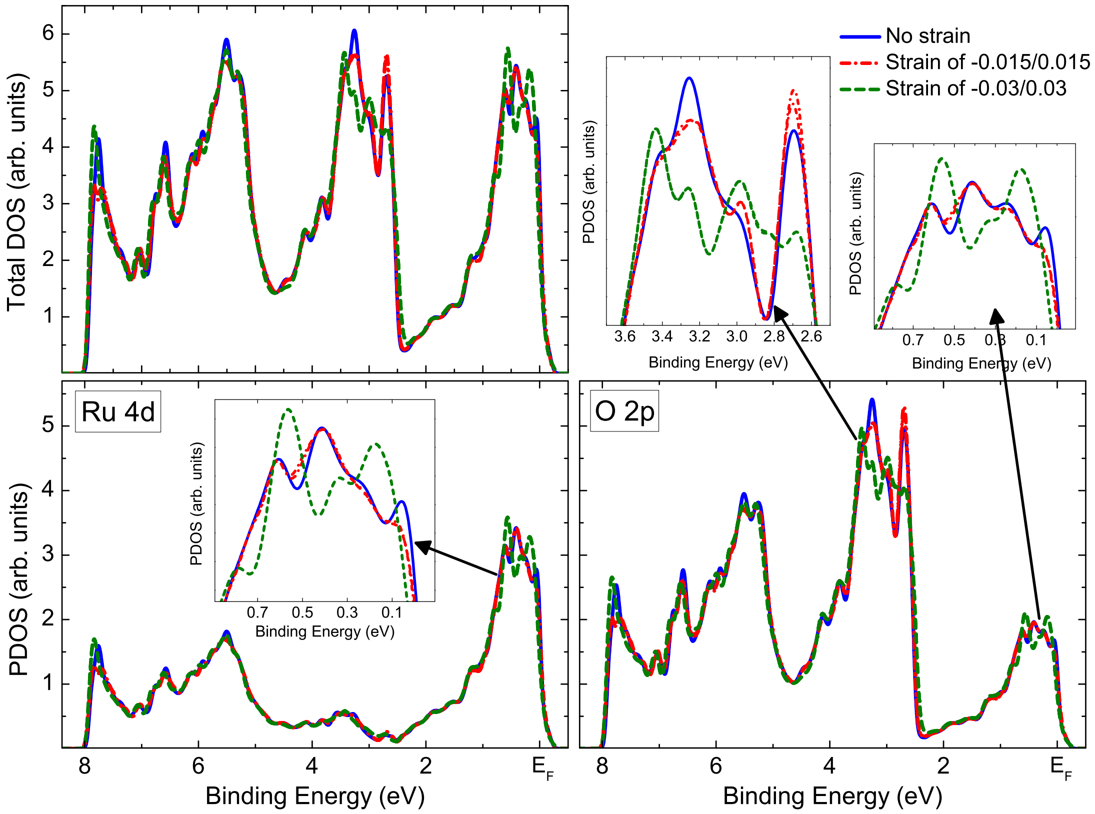

Figure 5.15 The total and projected DOS of ground-state orthorhombic $SrRuO_3$ under C_{44} related shear deformation calculated using PBEsol exchange-correlation functional.

does not depend on whether the applied deformation is compressive or tensile. The plots presented in Figure 5.15 reveal only a small change in the evolution of the spectra which is more visible in the insets — at the Fermi level for Ru 4*d* and at slightly higher binding energies for O 2*p*. Here, the curves representing DOS of unstrained $SrRuO_3$ and $SrRuO_6$ under $-0.015/0.015$ deformation exhibit a close resemblance, while a curve of $-0.03/0.03$ strain somewhat changes its profile. Although the connection between electronic structure and isosymmetric phase transition appears to be weak, a particular investigation is needed to identify the response of magnetic and other important properties of $SrRuO_3$.

On the whole, we believe that all these previously unknown findings not only shed a new light on $SrRuO_3$ from a fundamental perspective, but they are also essential for the successful engineering of the promising $SrRuO_3$-based technological applications. And it is not surprising that our further intentions are to help with the following efforts.

Chapter 6

Summary of the Results and Conclusions

In this study, two well-known perovskite crystals — $LaNiO_3$ and $SrRuO_3$ — have been investigated. A variety of important issues were taken into account, starting from the appropriate treatment of core and valence states, relativistic effects, and chemical bonding in $LaNiO_3$ up to electron correlation effects, role of oxygen vacancies, mechanical stability, and elastic behaviour of $SrRuO_3$. To sum up, it can be concluded that:

1. Among the examined exchange-correlation functionals, the revised PBEsol demonstrates the best performance while reproducing crystalline structure of $LaNiO_3$, despite that the inclusion of 15–30% of the exact HF exchange into PBE0 scheme has an appreciable improvement over the PBE results. This reveals the effectiveness of the revision made to PBEsol functional.

2. Pure DFT calculations tend to underestimate binding energies of the strongly localized core level states in $LaNiO_3$, whereas hybrid scheme due to the partly compensated SIE significantly improves the description of the peak positions. But at the valence band, however, hybrid scheme fails to simulate the experiment, while pure DFT calculations exhibit a good agreement because of the delocalized nature of the present electrons. These findings indicate that by applying pure DFT approximations and their hybrid schemes for the different regions of the spectrum it is possible to accurately reproduce the essential photoemission results. However, the correct identification of the peaks in the core region requires relativistic treatment, namely, the inclusion of spin-orbit interaction.

3. The electron density difference map, Mulliken population analysis, and a much weaker hybridization of La 5*d* and O 2*p* orbitals in comparison to that of Ni 3*d* and O 2*p* orbitals reveal a predominantly ionic character of La-O bond and a substantial covalent part in Ni-O bond which represent a

different bonding picture of $LaNiO_3$ compared to the formal ionic one.

4. The revisions made to the examined exchange-correlation functionals for solids allow to effectively improve the description of the crystalline structure of $SrRuO_3$ compared to the standard LDA and PBE frameworks. The step that restores back the precise value of the second-order gradient expansion for exchange ($\frac{10}{81}$) has a much larger impact than modification of correlation parameters or the form of the exchange enhancement factor.

5. A good agreement between DFT, UPS, and HAXPES results indicates that $SrRuO_3$ is a weakly correlated material with a sharp coherent Ru $4d$ peak at the Fermi level. The incoherent feature which experimentally manifests itself as a broad shoulder at 1.2–1.5 eV below E_F could be due to the the finite admixture of O $2p$ states in the dominant Ru $4d$ region and the asymmetric shape of coherent Ru $4d$ peak. Moreover, $SrRuO_3$ does not show any differences in its surface and bulk electronic structure thus raising doubts on the localized surface states as naturally occurring ones.

6. The spectral weight transfer in Ru $4d$ PDOS resulting in an increasing contribution of the incoherent peak as the oxygen content in $SrRuO_3$ decreases is perfectly consistent with the evolution of UPS spectra in annealing experiment. It allows to claim that the dominance of the incoherent feature, previously observed in *ex situ* measurements, could emerge *not* due to the manifestation of strong electron correlation in stoichiometric specimens, as it was thought, but due to the redistribution of electronic states caused by the introduction of oxygen vacancies during the cleaning or/and growth of the samples. Thus, the artificially affected surface states of $SrRuO_3$ should not be related with its natural internal electronic structure.

7. Tetragonal $SrRuO_3$ is mechanically unstable at zero temperature and pressure conditions, since under C_{44} related shear deformation the system tends to occupy the energetically lower states compared to the strain-free crystal. The structural transformation which could be related to this unusual behaviour is an abrupt reorientation of RuO_6 octahedra around x and z axes.

8. Under C_{44} related shear deformation, orthorhombic $SrRuO_3$ displays a distinct deviation from the initial parabolic behaviour at the critical strain values of $\sim \pm 0.02$ which are slightly dependent on the DFT approach used. The structural transformation that could be associated with the following discontinuity in behaviour is a strongly pronounced rotation of RuO_6 octahedra around z axis. The fact that this phenomenon is not accompanied by a change in crystallographic space group speaks for the manifestation of isosymmetric phase transition.

Appendix A

Hartree-Fock Theory

Within the adiabatic approximation, the electronic Schrödinger equation is written as

$$\hat{H}\Psi(\mathbf{x},\mathbf{R}) = E(\mathbf{R})\Psi(\mathbf{x},\mathbf{R}), \tag{A.1}$$

where the corresponding electronic Hamiltonian $\hat{H}$ is given by (2.5). The electronic wavefunction $\Psi(\mathbf{x},\mathbf{R})$ and its energy $E(\mathbf{R})$ depend on the coordinates of the nuclei $\mathbf{R}$ only parametrically, thus the notation $\mathbf{R}$ can be dropped. Repeating the calculations with different nuclear arrangements allows the potential energy surface to be mapped out and equilibrium geometry to be found. However, the crucial complication in such calculations is the presence of the electron-electron potential energy, which depends on the inter-electron distance $|\mathbf{r}_i - \mathbf{r}_j|$ [60], meaning that electron coordinates as variables cannot be separated. This complicates the guess of the possible form of the electronic wavefunction. As a first step in simplifying the following problem, it is convenient to express the N-electron wavefunction as a product of one-electron wavefunctions, called orbitals:

$$\Psi(\mathbf{x}_1, \mathbf{x}_2, \ldots, \mathbf{x}_N) = \psi_1(\mathbf{x}_1)\psi_2(\mathbf{x}_2)\ldots\psi_N(\mathbf{x}_N). \tag{A.2}$$

Since this solution reflects the idea of non-interacting system with no electron-electron repulsion term, it is referred to as an independent particle, or Hartree, approximation [61]. Unfortunately, (A.2) fails to satisfy the Pauli exclusion principle [208], which states that a wavefunction describing fermions should be antisymmetric with respect to the interchange of coordinates of any pair of electrons. Despite that, Fock demonstrated [62] that a Hartree product could be made antisymmetric by appropriately adding and subtracting all possible permutations of the Hartree product, thereby forming the Hartree-Fock (HF) wavefunction. Later, Slater showed [209] that the resulting wavefunction is simply a determinant, which can be expressed as

$$\Psi_{\mathrm{HF}}(\mathbf{x}_1, \mathbf{x}_2, \ldots, \mathbf{x}_N) = \frac{1}{\sqrt{N!}} \begin{vmatrix} \psi_1(\mathbf{x}_1) & \psi_2(\mathbf{x}_1) & \ldots & \psi_N(\mathbf{x}_1) \\ \psi_1(\mathbf{x}_2) & \psi_2(\mathbf{x}_2) & \ldots & \psi_N(\mathbf{x}_2) \\ \vdots & \vdots & \ddots & \vdots \\ \psi_1(\mathbf{x}_N) & \psi_2(\mathbf{x}_N) & \ldots & \psi_N(\mathbf{x}_N) \end{vmatrix}. \tag{A.3}$$

Replacing the true N-electron wavefunction by a single Slater determinant represents a drastic approach which results in a neglect of electron correlation, or equivalently, the inclusion of electron-electron repulsion only as an average effect. Hence, each electron is considered to be moving in the electrostatic field of the nuclei and the average field of the other $N-1$ electrons [60]. For this reason, the HF method is also referred to as a mean-field approximation. But this model can be improved with additional determinants generating solutions which can be made to converge towards the exact solution of the electronic Schrödinger equation [55].

The energy of an approximate wavefunction can be calculated as the expectation value of the Hamiltonian divided by the norm of the wavefunction:

$$E = \frac{\langle\Psi| \hat{H} |\Psi\rangle}{\langle\Psi|\Psi\rangle}. \tag{A.4}$$

For a normalized wavefunction the denominator is 1, therefore the expectation value of HF energy is found to be given by [59]

$$E_{\mathrm{HF}} = \langle\Psi_{\mathrm{HF}}| \hat{H} |\Psi_{\mathrm{HF}}\rangle = \sum_{i=1}^{N} H_i + \frac{1}{2}\sum_{i,j=1}^{N} (J_{ij} - K_{ij}), \tag{A.5}$$

where

$$H_i = \int \psi_i^*(\mathbf{x}) \left[-\frac{1}{2}\nabla^2 + V(\mathbf{r})\right] \psi_i(\mathbf{x}) d^3x, \tag{A.6}$$

$$J_{ij} = \int\int \frac{\psi_i(\mathbf{x})\psi_i^*(\mathbf{x})\psi_j^*(\mathbf{x}')\psi_j(\mathbf{x}')}{|\mathbf{r}-\mathbf{r}'|} d^3x d^3x', \tag{A.7}$$

$$K_{ij} = \int\int \frac{\psi_i^*(\mathbf{x})\psi_j(\mathbf{x})\psi_i(\mathbf{x}')\psi_j^*(\mathbf{x}')}{|\mathbf{r}-\mathbf{r}'|} d^3x d^3x'. \tag{A.8}$$

H_i defines the contribution due to the kinetic energy and the electron-nucleus attraction, while J_{ij} and K_{ij} are the Coulomb and exchange integrals, respectively, which represent the interaction between two electrons. It should be noted that

$$J_{ij} \geq K_{ij} \geq 0. \tag{A.9}$$

Besides,

$$J_{ii} = K_{ii}. \tag{A.10}$$

This is the reason the double summation in (A.5) can include the $i = j$ terms. If $i = j$, the integral (A.7) describes the Coulomb interaction of the charge distribution of one electron with itself. As a consequence, the energy of a one-electron system, in which there is definitely no electron-electron repulsion, would have a contribution from (A.7). Since the self-interaction is obviously spurious, the exchange term (A.8) takes care of this: for $i = j$, the Coulomb and exchange integrals are identical and due to the opposite signs in (A.5) exactly cancel each other. Therefore, the self-interaction problem is elegantly solved within the HF framework.

The system of equations for one-electron orbitals is obtained from the variational principle minimizing (A.5) and assuring the orthonormalization condition

$$\int \psi_i^*(\mathbf{x})\psi_j(\mathbf{x}) d^3x = \delta_{ij}. \tag{A.11}$$

The HF differential equations have the form

$$\hat{F}\psi_i(\mathbf{x}) = \sum_{j=1}^{N} \varepsilon_{ij}\psi_j(\mathbf{x}), \tag{A.12}$$

where the Fock operator

$$\hat{F} = \hat{T} + \hat{V} + \hat{J} - \hat{K}. \tag{A.13}$$

The Coulomb and exchange operators are defined by

$$\hat{J}(\mathbf{x})\psi_i(\mathbf{x}) = \sum_{j=1}^{N} \int \frac{\psi_j^*(\mathbf{x}')\psi_j(\mathbf{x}')\psi_i(\mathbf{x})}{|\mathbf{r} - \mathbf{r}'|} d^3x' \tag{A.14}$$

and

$$\hat{K}(\mathbf{x})\psi_i(\mathbf{x}) = \sum_{j=1}^{N} \int \frac{\psi_j^*(\mathbf{x}')\psi_j(\mathbf{x})\psi_i(\mathbf{x}')}{|\mathbf{r} - \mathbf{r}'|} d^3x', \tag{A.15}$$

respectively. Since the result of application of $\hat{J}(\mathbf{x})$ on $\psi_i(\mathbf{x})$ depends solely on $\psi_i(\mathbf{x})$ value at position $\mathbf{x}$, this operator and the corresponding potential are called local. But the result of $\hat{K}(\mathbf{x})$ acting on $\psi_i(\mathbf{x})$ depends on $\psi_i(\mathbf{x})$ value at all points in space because the following one-electron wavefunction is now related to the integration variable $\mathbf{x}'$. Consequently, this operator and the corresponding exchange potential are called non-local.

The matrix $\boldsymbol{\varepsilon}$ consists of Lagrange multipliers and its diagonal elements have the physical interpretation of orbital energies. The expression for orbital energies can be obtained by multiplying (A.12) by $\psi_i^*(\mathbf{x})$ and integrating:

$$\varepsilon_i \equiv \varepsilon_{ii} = \langle \psi_i | \hat{F} | \psi_i \rangle = H_i + \sum_{j=1}^{N} (J_{ij} - K_{ij}). \tag{A.16}$$

Summing over i and comparing with (A.5) yields

$$E_{\mathrm{HF}} = \sum_{i=1}^{N} \varepsilon_i - \frac{1}{2} \sum_{i,j=1}^{N} (J_{ij} - K_{ij}), \tag{A.17}$$

where the last term corresponds to the total electron-electron repulsion energy. Note that E_{HF} is not equal to the sum of orbital energies.

As the Fock operator depends on all the occupied electron orbitals appearing in the expression of the Coulomb and exchange operators, solution of (A.12) must proceed iteratively. Therefore, the HF method is based on the self-consistent field procedure, in which a trial set of orbitals is formulated and used to construct the Fock operator. Then, the HF equations are solved to obtain a new set of orbitals that are used to construct a revised Fock operator, and so on. The cycle of calculation and reformulation is repeated until a convergence criterion is satisfied [60].

Appendix B

Exchange-Correlation Hole

The concept of one-electron density (2.1) provides an answer to the question of how likely is it to find one electron of any spin within a particular volume element, while all other electrons may be anywhere [56]. If we are interested in probability of finding electron with an arbitrary spin s, then (2.1) transforms to [210]

$$n(\mathbf{x}) = N \int \dots \int |\Psi(\mathbf{x}, \mathbf{x}_2, \dots, \mathbf{x}_N)|^2 d^3x_2 \dots d^3x_N. \tag{B.1}$$

The one-electron density can be extended to the probability of simultaneously finding a pair of two electrons with spins s and s' within two particular volume elements d^3r and d^3r' among the remaining $N-2$ electrons in the system. The quantity that contains this information is the pair-electron density $\pi(\mathbf{x}, \mathbf{x}')$, which is defined as

$$\pi(\mathbf{x}, \mathbf{x}') = N(N-1) \int \dots \int |\Psi(\mathbf{x}, \mathbf{x}', \mathbf{x}_3, \dots, \mathbf{x}_N)|^2 d^3x_3 \dots d^3x_N. \tag{B.2}$$

Here, $\Psi(\mathbf{x}, \mathbf{x}', \mathbf{x}_3, \dots, \mathbf{x}_N) \equiv \Psi(\mathbf{x}_1, \mathbf{x}_2, \mathbf{x}_3, \dots, \mathbf{x}_N)$. In case of the probability of finding electrons with any combination of spins (one up, one down; both up; both down), the pair-electron density becomes

$$\pi(\mathbf{r}, \mathbf{r}') = N(N-1) \int \dots \int |\Psi(\mathbf{x}, \mathbf{x}', \mathbf{x}_3, \dots, \mathbf{x}_N)|^2 ds ds' d^3x_3 \dots d^3x_N. \tag{B.3}$$

The pair-electron density actually contains all the information about electron correlation. It is a non-negative quantity normalized to the total number of non-distinct electron pairs $N(N-1)$. Since one-electron density can be expressed

$$n(\mathbf{x}) = \frac{1}{N-1} \int \pi(\mathbf{x}, \mathbf{x}') d^3x', \tag{B.4}$$

and

$$\int n(\mathbf{x}) d^3x = N, \tag{B.5}$$

this leads to the following condition

$$\int\int \pi(\mathbf{x},\mathbf{x}')d^3xd^3x' = N(N-1). \tag{B.6}$$

From the antisymmetry of the many-electron wavefunction it follows that

$$\pi(\mathbf{x},\mathbf{x}) = -\pi(\mathbf{x},\mathbf{x}), \tag{B.7}$$

which is true only if $\pi(\mathbf{x},\mathbf{x}) = 0$ [56]. It means that the probability of finding two electrons with the same spin at the same point in space is zero. This feature is known as exchange or Fermi correlation, and is a direct consequence of the Pauli exclusion principle. It is in no way connected to the charge of electrons and applies equally to neutral fermions. However, one should keep in mind that exchange does not hold if the two electrons have different spins.

The electrostatic repulsion of electrons prevents them from coming too close to each other. This effect manifests as Coulomb or simply electron correlation, and is independent of the spin. The presence of exchange and correlation results in a reduced probability of finding another electron in the immediate vicinity of the reference electron [55]. In other words, each electron creates a depletion, or hole, of density around itself which keeps other electrons from approaching it.

For the definition of the exchange-correlation hole, it is convenient to introduce the concept of the conditional probability $\Omega(\mathbf{x}',\mathbf{x})$, which corresponds to the probability of finding any electron at position $\mathbf{x}'$ in coordinate-spin space if there is one already known to be at position $\mathbf{x}$:

$$\Omega(\mathbf{x}',\mathbf{x}) = \frac{\pi(\mathbf{x},\mathbf{x}')}{n(\mathbf{x})}. \tag{B.8}$$

The exchange-correlation hole is then defined as the difference between the conditional probability and the uncorrelated probability of finding an electron at $\mathbf{x}'$:

$$h_{\mathrm{XC}}(\mathbf{x},\mathbf{x}') = \frac{\pi(\mathbf{x},\mathbf{x}')}{n(\mathbf{x})} - n(\mathbf{x}'). \tag{B.9}$$

It describes the change in conditional probability caused by the correction for spurious self-interaction, exchange, and Coulomb correlation, compared to the completely uncorrelated situation. By taking into consideration (B.5) and (B.6), it can be shown that

$$\int \Omega(\mathbf{x}', \mathbf{x}) d^3x' = N - 1, \tag{B.10}$$

therefore, the exchange-correlation hole contains exactly the charge of one electron

$$\int h_{\mathrm{XC}}(\mathbf{x}, \mathbf{x}') d^3x' = -1. \tag{B.11}$$

Interestingly, the electrostatic repulsion energy of electrons $U[n]$ can be expressed in terms of the spin-independent pair-electron density $\pi(\mathbf{r}, \mathbf{r}')$:

$$U[n] = \frac{1}{2} \int \int \frac{\pi(\mathbf{r}, \mathbf{r}')}{|\mathbf{r} - \mathbf{r}'|} d^3r d^3r'. \tag{B.12}$$

The rearrangement of respective $h_{\mathrm{XC}}(\mathbf{r}, \mathbf{r}')$ results in

$$\pi(\mathbf{r}, \mathbf{r}') = n(\mathbf{r})n(\mathbf{r}') + n(\mathbf{r})h_{\mathrm{XC}}(\mathbf{r}, \mathbf{r}'), \tag{B.13}$$

which can be used for splitting (B.12) into two contributions

$$U[n] = \frac{1}{2} \int \int \frac{n(\mathbf{r})n(\mathbf{r}')}{|\mathbf{r} - \mathbf{r}'|} d^3r d^3r' + \frac{1}{2} \int \int \frac{n(\mathbf{r})h_{\mathrm{XC}}(\mathbf{r}, \mathbf{r}')}{|\mathbf{r} - \mathbf{r}'|} d^3r d^3r'. \tag{B.14}$$

The first term is already expressed as $J[n]$ in (2.10) and stands for the classical Coulomb repulsion energy of electrons. It is important to note that $J[n]$ contains the unphysical self-interaction. The second term is the energy of interaction between the electron density and the charge distribution of the exchange-correlation hole. Since this term includes the correction for the self-interaction together with all non-classical effects, it becomes obvious why the concept of the hole is of a great interest. The more we know about the characteristics of $h_{\mathrm{XC}}(\mathbf{r}, \mathbf{r}')$ and the better the approximate hole functions resemble the true ones, the more accurate results we can expect.

The exchange-correlation hole can be formally split into the Fermi hole, $h_{\mathrm{X}}(\mathbf{r}, \mathbf{r}') =$

$h_{\mathrm{X}}^{s=s'}(\mathbf{r},\mathbf{r}')$, and the Coulomb hole, $h_{\mathrm{C}}(\mathbf{r},\mathbf{r}') = h_{\mathrm{C}}^{s,s'}(\mathbf{r},\mathbf{r}')$,

$$h_{\mathrm{XC}}(\mathbf{r},\mathbf{r}') = h_{\mathrm{X}}^{s=s'}(\mathbf{r},\mathbf{r}') + h_{\mathrm{C}}^{s,s'}(\mathbf{r},\mathbf{r}'). \tag{B.15}$$

The exchange hole emerges due to the antisymmetry of the wavefunction and applies only to electrons with the same spin, whereas the correlation hole has contributions for electrons of either spin and results from the electrostatic interaction. Although this separation, motivated by HF picture in which only the Fermi hole is included, appears to be convenient, only the total hole has a real physical meaning.

Considering the Fermi hole, it should be noticed that it dominates by far the Coulomb hole. What is more, just like the total hole, it integrates to the charge of one electron

$$\int h_{\mathrm{X}}(\mathbf{r},\mathbf{r}')d^3r' = -1. \tag{B.16}$$

This means that the conditional probability for electrons of spin s integrates to $N_s - 1$ instead of N_s because there is one electron of the same spin s already known to be at $\mathbf{r}$. Therefore, this electron is removed from the distribution. By removal of the following charge, the Fermi hole also takes care of the self-interaction problem. Due to the Pauli exclusion principle, the Fermi hole has to become equal to the negative one-electron density for $\mathbf{r} \to \mathbf{r}'$,

$$h_{\mathrm{X}}(\mathbf{r} \to \mathbf{r}', \mathbf{r}') = -n(\mathbf{r}'). \tag{B.17}$$

It can be shown that

$$h_{\mathrm{X}}(\mathbf{r},\mathbf{r}') \leq 0, \tag{B.18}$$

besides, the actual shape of the Fermi hole depends on the one-electron density at $\mathbf{r}'$. As a consequence, $h_{\mathrm{X}}(\mathbf{r},\mathbf{r}')$ is not spherically symmetric.

From (B.11) and (B.16) it is obvious that the Coulomb hole must be normalized to zero, meaning that the integral over all space contains no charge:

$$\int h_{\mathrm{C}}(\mathbf{r},\mathbf{r}')d^3r' = 0. \tag{B.19}$$

The Coulomb hole is negative and acquires the largest value at the position of the reference electron, since it originates from the electrostatic interaction which keeps electrons apart. The fact that $h_{\mathrm{C}}(\mathbf{r}, \mathbf{r}')$ integrates to zero indicates that it must be positive in some regions. In other words, one-electron density is taken away from areas close to the reference electron and is brought to regions farther away from it.

In general, the sum rule (B.16) and negativity constraint (B.18) on the exchange hole represent stringent requirements, which together determine a well-defined spatial range for the exchange hole. In comparison, the corresponding sum rule (B.19) on the correlation hole is a much weaker constraint, since $h_{\mathrm{C}}(\mathbf{r}, \mathbf{r}')$ can have positive or negative values, and so the corresponding length scale is not that well-defined. However, a large part of success demonstrated by rather crude model of local density approximation (LDA) lies in the fact that its exchange-correlation hole satisfies most of the important relations established for the true exchange-correlation hole. Among those are the aforementioned sum rules and negativity constraint. Of course, the LDA and exact exchange-correlation holes differ in many details but it is also true that the homogeneous electron gas provides a reasonable first approximation to spherically averaged exchange-correlation holes of real systems. Hence, the straightforward inclusion of low-order gradient corrections violates requirements for the exchange-correlation hole, and this consequently results in much more erratic $E_{\mathrm{XC}}[n]$ values. This problem was solved by enforcing the restrictions valid for the true exchange-correlation holes through cut-off procedures that restore the violated constraints. Functionals that include the gradients of the one-electron density and restore the requirements for exchange-correlation hole in the cut-off manner became known as generalized gradient approximations (GGAs). Having in mind that GGAs can be more or less treated as mathematically complex structures developed to satisfy a set of requirements, it is no surprise that on the whole these functionals make it difficult to point out the clear-cut physics that stands behind them.

Appendix C

Adiabatic Connection

The introduction of exchange-correlation hole $h_{\mathrm{XC}}(\mathbf{r},\mathbf{r}')$ into the expression of electrostatic repulsion energy of electrons (B.14) allows to account for the non-classical contributions, namely, the exchange and Coulomb correlation. However, the exchange-correlation energy (2.22) also possesses a term which describes the kinetic correlation energy, $(T[n]-T_{\mathrm{S}}[n])$. In order to include this information, it is convenient to apply the adiabatic connection procedure [211] in which two systems — the non-interacting reference with no electron-electron repulsion and the real one with electron-electron interaction acting at full strength — are connected by gradually increasing the coupling strength parameter λ from 0 to 1:

$$\hat{H}_{\lambda} = \hat{T} + \lambda\hat{U} + \hat{V}_{\lambda}. \tag{C.1}$$

For each λ, the effective external potential $\hat{V}_{\lambda}$ is adapted in such a way that $n(\mathbf{r})$ remains fixed at the value corresponding to the density of the fully interacting system. Therefore, for $\lambda = 0$, the Hamiltonian of the non-interacting reference system is recovered with $\hat{V}_{\lambda=0} = \hat{V}_{\mathrm{S}}$ [see (2.15)], while $\lambda = 1$ gives the regular expression for the real system. Equation (C.1) describes how these two endpoints are smoothly connected through a continuum of artificial, partially interacting systems [56]. Now, the total energy of the interacting system $E_{\lambda=1}[n]$ can be expressed through the following integral

$$E_{\lambda=1}[n] - E_{\lambda=0}[n] = \int_0^1 dE_{\lambda}[n], \tag{C.2}$$

as

$$E_{\lambda=1}[n] = \int_0^1 dE_{\lambda}[n] + E_{\lambda=0}[n]. \tag{C.3}$$

To utilize this relation, an explicit expression for $dE_{\lambda}[n]$ is needed. The change in total energy $E_{\lambda}[n]$ upon an infinitesimal change in the coupling strength parameter

λ can be written using the exchange-correlation hole formalism:

$$dE_\lambda[n] = \frac{1}{2}d\lambda \int\int \frac{n(\mathbf{r})n(\mathbf{r}')}{|\mathbf{r}-\mathbf{r}'|}d^3rd^3r' \\ + \frac{1}{2}d\lambda \int\int \frac{n(\mathbf{r})h^\lambda_{\mathrm{XC}}(\mathbf{r},\mathbf{r}')}{|\mathbf{r}-\mathbf{r}'|}d^3rd^3r' + \int n(\mathbf{r})dV_\lambda(\mathbf{r})d^3r. \quad \text{(C.4)}$$

Inserting (C.4) into (C.2) yields

$$E_{\lambda=1}[n] - E_{\lambda=0}[n] = \frac{1}{2}\int\int \frac{n(\mathbf{r})n(\mathbf{r}')}{|\mathbf{r}-\mathbf{r}'|}d^3rd^3r' \\ + \frac{1}{2}\int\int\int_0^1 \frac{n(\mathbf{r})h^\lambda_{\mathrm{XC}}(\mathbf{r},\mathbf{r}')}{|\mathbf{r}-\mathbf{r}'|}d^3rd^3r'd\lambda + \int n(\mathbf{r})[V_{\lambda=1}(\mathbf{r}) - V_{\lambda=0}(\mathbf{r})]d^3r, \quad \text{(C.5)}$$

where $n(\mathbf{r})$ independence of λ was taken into account. Replacing $V_{\lambda=1}(\mathbf{r})$ and $V_{\lambda=0}(\mathbf{r})$ by $V(\mathbf{r})$ and $V_\mathrm{S}(\mathbf{r})$, respectively, and using the total energy expression for the non-interacting system (2.20), the following equation for the real, interacting system is obtained:

$$E_{\lambda=1}[n] = T_\mathrm{S}[n] + \frac{1}{2}\int\int \frac{n(\mathbf{r})n(\mathbf{r}')}{|\mathbf{r}-\mathbf{r}'|}d^3rd^3r' \\ + \int n(\mathbf{r})V(\mathbf{r})d^3r + \frac{1}{2}\int\int \frac{n(\mathbf{r})\overline{h}_{\mathrm{XC}}(\mathbf{r},\mathbf{r}')}{|\mathbf{r}-\mathbf{r}'|}d^3rd^3r'. \quad \text{(C.6)}$$

Here, the notation

$$\overline{h}_{\mathrm{XC}}(\mathbf{r},\mathbf{r}') = \int_0^1 h^\lambda_{\mathrm{XC}}(\mathbf{r},\mathbf{r}')d\lambda \quad \text{(C.7)}$$

defines the coupling-strength integrated exchange-correlation hole. It is important to note that the last term in (C.6) corresponds to the exact exchange-correlation energy:

$$E_{\mathrm{XC}}[n] = \frac{1}{2}\int\int \frac{n(\mathbf{r})\overline{h}_{\mathrm{XC}}(\mathbf{r},\mathbf{r}')}{|\mathbf{r}-\mathbf{r}'|}d^3rd^3r'. \quad \text{(C.8)}$$

This means that the substitution of exchange-correlation hole with coupling-strength integrated exchange-correlation hole allows to include the difference between the kinetic energy of real and non-interacting systems. The price must be paid is a further complication of the exchange-correlation hole due to additional integration over the coupling strength parameter λ. However, this integration has no effect on the formal properties of $h_{\mathrm{XC}}(\mathbf{r},\mathbf{r}')$ discussed in Appendix B.

Appendix D

RuO_6 under Shear Deformation

Additional data on the evolution of RuO_6 structural parameters [see Figure 5.1(c)] for ground-state tetragonal $SrRuO_3$:

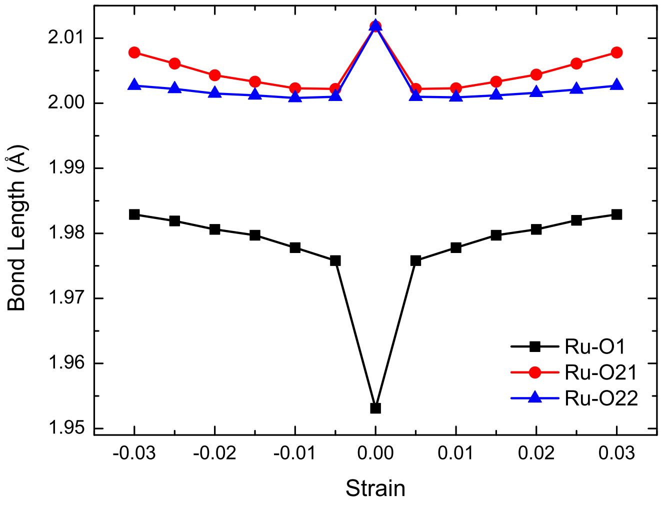

Figure D.1 Ru-O bond lengths of ground-state tetragonal $SrRuO_3$ as a function of strain under C_{44} related shear deformation within PBEsol exchange-correlation framework.

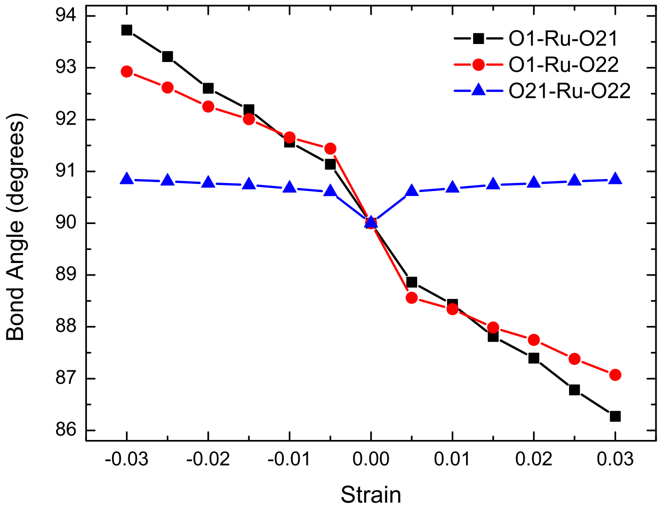

Figure D.2 O-Ru-O bond angles of ground-state tetragonal $SrRuO_3$ as a function of strain under C_{44} related shear deformation within PBEsol exchange-correlation framework.

Additional data on the evolution of RuO_6 structural parameters [see Figure 5.1(b)] for ground-state orthorhombic $SrRuO_3$:

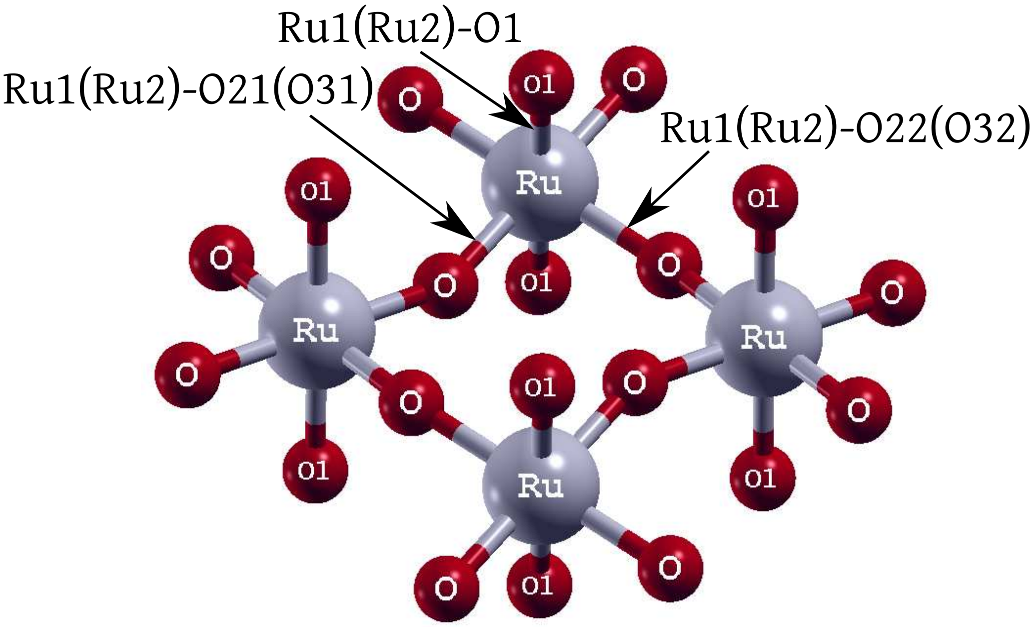

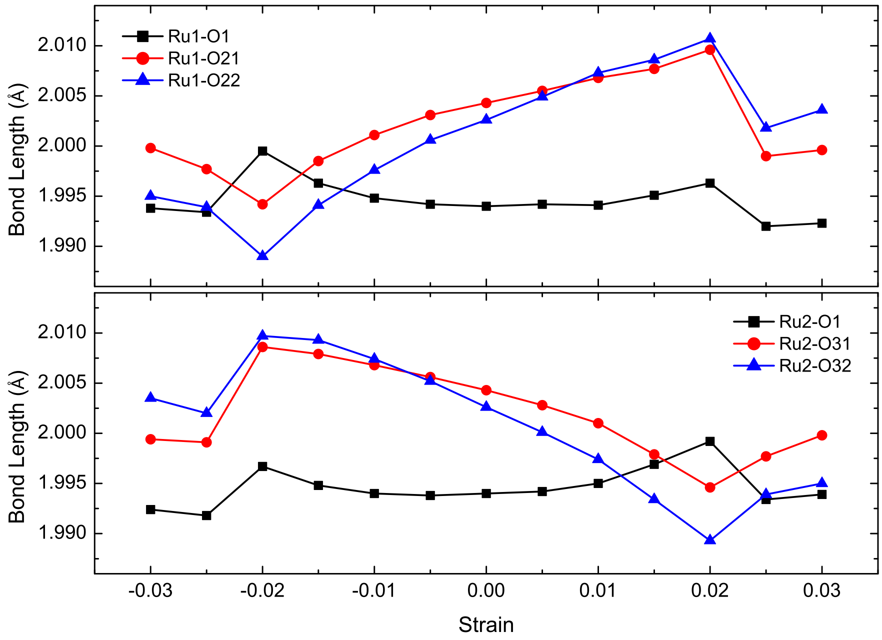

Figure D.3 Ru-O bond lengths of ground-state orthorhombic $SrRuO_3$ as a function of strain under C_{44} related shear deformation within PBEsol exchange-correlation framework.

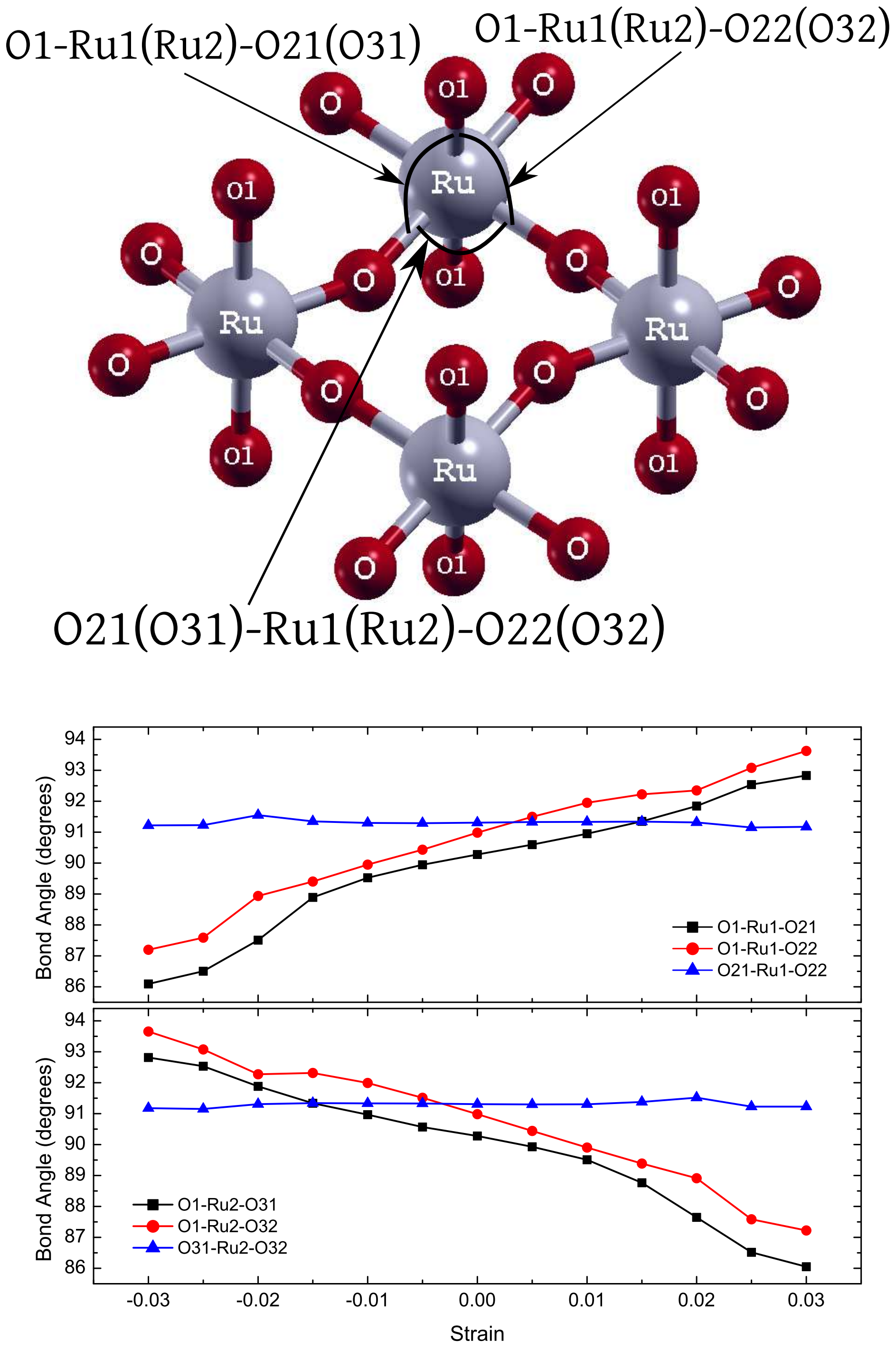

Figure D.4 O-Ru-O bond angles of ground-state orthorhombic $SrRuO_3$ as a function of strain under C_{44} related shear deformation within PBEsol exchange-correlation framework.

Bibliography

[1] T. Wolfram and S. Ellialtioglu, *Electronic and Optical Properties of d-Band Perovskites* (Cambridge University Press, New York, 2006).

[2] M. D. Graef and M. E. McHenry, *Structure of Materials: An Introduction to Crystallography, Diffraction, and Symmetry* (Cambridge University Press, New York, 2007).

[3] M. Murakami, Y. Ohishi, N. Hirao, and K. Hirose, "A perovskitic lower mantle inferred from high-pressure, high-temperature sound velocity data," Nature **485**, 90 (2012).

[4] L. G. Tejuca and J. L. G. Fierro, *Properties and Applications of Perovskite-Type Oxides* (Marcel Dekker, New York, 1993).

[5] J. He and C. Franchini, "Screened hybrid functional applied to $3d^0 \to 3d^8$ transition-metal perovskites LaMO$_3$ (M = Sc-Cu): Influence of the exchange mixing parameter on the structural, electronic, and magnetic properties," Phys. Rev. B **86**, 235117 (2012).

[6] M. A. Peña and J. L. G. Fierro, "Chemical structures and performance of perovskite oxides," Chem. Rev. **101**, 1981 (2001).

[7] M. B. Salamon and M. Jaime, "The physics of manganites: Structure and transport," Rev. Mod. Phys. **73**, 583 (2001).

[8] P. Vernoux, L. Lizarraga, M. N. Tsampas, F. M. Sapountzi, A. De Lucas-Consuegra, J.-L. Valverde, S. Souentie, C. G. Vayenas, D. Tsiplakides, S. Balomenou, and E. A. Baranova, "Ionically conducting ceramics as active catalyst supports," Chem. Rev. **113**, 8192 (2013).

[9] A. Y. Dobin, K. R. Nikolaev, I. N. Krivorotov, R. M. Wentzcovitch, E. D. Dahlberg, and A. M. Goldman, "Electronic and crystal structure of fully strained LaNiO$_3$ films," Phys. Rev. B **68**, 113408 (2003).

[10] G. Gou, I. Grinberg, A. M. Rappe, and J. M. Rondinelli, "Lattice normal modes and electronic properties of the correlated metal LaNiO$_3$," Phys. Rev. B **84**, 144101 (2011).

[11] P. Murugavel, R. Sharma, A. R. Raju, and C. N. R. Rao, "A study of ferroelectric thin films deposited on a LaNiO$_3$ barrier electrode by nebulized spray pyrolysis," J. Phys. D: Appl. Phys. **33**, 906 (2000).

[12] M. Jain, B. S. Kang, and Q. X. Jia, "Effect of conductive LaNiO$_3$ electrode on the structural and ferroelectric properties of Bi$_{3.25}$La$_{0.75}$Ti$_3$O$_{12}$ films," Appl. Phys. Lett. **89**, 242903 (2006).

[13] K.-T. Kim, C.-I. Kim, J.-G. Kim, and G.-H. Kim, "Effect of LaNiO$_3$ electrode on microstructural and ferroelectric properties of Bi$_{3.25}$La$_{0.75}$Ti$_3$O$_{12}$ thin films," Thin Solid Films **515**, 8082 (2007).

[14] R. Scherwitzl, P. Zubko, C. Lichtensteiger, and J.-M. Triscone, "Electric-field tuning of the metal-insulator transition in ultrathin films of $LaNiO_3$," Appl. Phys. Lett. **95**, 222114 (2009).

[15] P. Hansmann, X. Yang, A. Toschi, G. Khaliullin, O. K. Andersen, and K. Held, "Turning a nickelate Fermi surface into a cupratelike one through heterostructuring," Phys. Rev. Lett. **103**, 016401 (2009).

[16] J. Chaloupka and G. Khaliullin, "Orbital order and possible superconductivity in $LaNiO_3/LaMO_3$ superlattices," Phys. Rev. Lett. **100**, 016404 (2008).

[17] D. D. Sarma, N. Shanthi, S. R. Barman, N. Hamada, H. Sawada, and K. Terakura, "Band theory for ground-state properties and excitation spectra of perovskite $\mathrm{La}M\mathrm{O}_3$ (M = Mn, Fe, Co, Ni)," Phys. Rev. Lett. **75**, 1126 (1995).

[18] V. I. Anisimov, D. Bukhvalov, and T. M. Rice, "Electronic structure of possible nickelate analogs to the cuprates," Phys. Rev. B **59**, 7901 (1999).

[19] Y.-L. Lee, J. Kleis, J. Rossmeisl, and D. Morgan, "*Ab initio* energetics of $\mathrm{La}B\mathrm{O}_3(001)$ (B = Mn, Fe, Co, and Ni) for solid oxide fuel cell cathodes," Phys. Rev. B **80**, 224101 (2009).

[20] Y. Nohara, S. Yamamoto, and T. Fujiwara, "Electronic structure of perovskite-type transition metal oxides $\mathrm{La}M\mathrm{O}_3$ ($M = \mathrm{Ti} \sim \mathrm{Cu}$) by U + GW approximation," Phys. Rev. B **79**, 195110 (2009).

[21] T. Kiyama, K. Yoshimura, K. Kosuge, Y. Ikeda, and Y. Bando, "Invar effect of $SrRuO_3$: Itinerant electron magnetism of Ru 4*d* electrons," Phys. Rev. B **54**, R756 (1996).

[22] H. N. Lee, H. M. Christen, M. F. Chisholm, C. M. Rouleau, and D. H. Lowndes, "Thermal stability of epitaxial $SrRuO_3$ films as a function of oxygen pressure," Appl. Phys. Lett. **84**, 4107 (2004).

[23] G. Koster, L. Klein, W. Siemons, G. Rijnders, J. S. Dodge, C.-B. Eom, D. H. A. Blank, and M. R. Beasley, "Structure, physical properties, and applications of $SrRuO_3$ thin films," Rev. Mod. Phys. **84**, 253 (2012).

[24] D. E. Shai, C. Adamo, D. W. Shen, C. M. Brooks, J. W. Harter, E. J. Monkman, B. Burganov, D. G. Schlom, and K. M. Shen, "Quasiparticle mass enhancement and temperature dependence of the electronic structure of ferromagnetic $SrRuO_3$ thin films," Phys. Rev. Lett. **110**, 087004 (2013).

[25] J. Junquera and P. Ghosez, "Critical thickness for ferroelectricity in perovskite ultrathin films," Nature **422**, 506 (2003).

[26] T. Fujii, M. Kawasaki, A. Sawa, H. Akoh, Y. Kawazoe, and Y. Tokura, "Hysteretic current–voltage characteristics and resistance switching at an epitaxial oxide Schottky junction $SrRuO_3/SrTi_{0.99}Nb_{0.01}O_3$," Appl. Phys. Lett. **86**, 012107 (2005).

[27] S. Thota, Q. Zhang, F. Guillou, U. Lüders, N. Barrier, W. Prellier, A. Wahl, and P. Padhan, "Anisotropic magnetocaloric effect in all-ferromagnetic ($La_{0.7}Sr_{0.3}MnO_3/SrRuO_3$) superlattices," Appl. Phys. Lett. **97**, 112506 (2010).

[28] M. K. Niranjan, J. D. Burton, J. P. Velev, S. S. Jaswal, and E. Y. Tsymbal, "Magnetoelectric effect at the $SrRuO_3/BaTiO_3$ (001) interface: An *ab initio* study," Appl. Phys. Lett. **95**, 052501 (2009).

[29] S. C. Gausepohl, M. Lee, L. Antognazza, and K. Char, "Magnetoresistance probe of spatial current variations in high-T_c $YBa_2Cu_3O_7$–$SrRuO_3$–$YBa_2Cu_3O_7$ Josephson junctions," Appl. Phys. Lett. **67**, 1313 (1995).

[30] M. Feigenson, L. Klein, M. Karpovski, J. W. Reiner, and M. R. Beasley, "Suppression of the superconducting critical current of Nb in bilayers of $Nb/SrRuO_3$," J. Appl. Phys. **97**, 10J120 (2005).

[31] K. Fujioka, J. Okamoto, T. Mizokawa, A. Fujimori, I. Hase, M. Abbate, H. J. Lin, C. T. Chen, Y. Takeda, and M. Takano, "Electronic structure of $SrRuO_3$," Phys. Rev. B **56**, 6380 (1997).

[32] J. Okamoto, T. Mizokawa, A. Fujimori, I. Hase, M. Nohara, H. Takagi, Y. Takeda, and M. Takano, "Correlation effects in the electronic structure of $SrRuO_3$," Phys. Rev. B **60**, 2281 (1999).

[33] M. V. R. Rao, V. G. Sathe, D. Sornadurai, B. Panigrahi, and T. Shripathi, "Electronic structure of $ARuO_3$ (A = Ca, Sr and Ba) compounds," J. Phys. Chem. Solids **62**, 797 (2001).

[34] J. Kim, J. Chung, and S.-J. Oh, "*In situ* photoemission study on $SrRuO_3/SrTiO_3$ films grown by pulsed laser deposition," Phys. Rev. B **71**, 121406 (2005).

[35] W. Siemons, G. Koster, A. Vailionis, H. Yamamoto, D. H. A. Blank, and M. R. Beasley, "Dependence of the electronic structure of $SrRuO_3$ and its degree of correlation on cation off-stoichiometry," Phys. Rev. B **76**, 075126 (2007).

[36] K. Horiba, H. Kawanaka, Y. Aiura, T. Saitoh, C. Satoh, Y. Kikuchi, M. Yokoyama, Y. Nishihara, R. Eguchi, Y. Senba, H. Ohashi, Y. Kitajima, and S. Shin, "Electronic structure of $SrRu_{1-x}Mn_xO_3$ studied by photoemission and x-ray absorption spectroscopy," Phys. Rev. B **81**, 245127 (2010).

[37] J. M. Rondinelli, N. M. Caffrey, S. Sanvito, and N. A. Spaldin, "Electronic properties of bulk and thin film $SrRuO_3$: Search for the metal-insulator transition," Phys. Rev. B **78**, 155107 (2008).

[38] E. Jakobi, S. Kanungo, S. Sarkar, S. Schmitt, and T. Saha-Dasgupta, "LDA + DMFT study of Ru-based perovskite $SrRuO_3$ and $CaRuO_3$," Phys. Rev. B **83**, 041103 (2011).

[39] H. Hadipour and M. Akhavan, "Electron correlation in Sr(Ca)RuO_3 by GWA and LSDA + U," Eur. Phys. J. B **84**, 203 (2011).

[40] B. J. Kennedy and B. A. Hunter, "High-temperature phases of $SrRuO_3$," Phys. Rev. B **58**, 653 (1998).

[41] A. T. Zayak, X. Huang, J. B. Neaton, and K. M. Rabe, "Structural, electronic, and magnetic properties of $SrRuO_3$ under epitaxial strain," Phys. Rev. B **74**, 094104 (2006).

[42] J.-M. Albina, M. Mrovec, B. Meyer, and C. Elsässer, "Structure, stability, and electronic properties of $SrTiO_3/LaAlO_3$ and $SrTiO_3/SrRuO_3$ interfaces," Phys. Rev. B **76**, 165103 (2007).

[43] P. García-Fernández, S. Ghosh, N. J. English, and J. A. Aramburu, "Benchmark study for the application of density functional theory to the prediction of octahedral tilting in perovskites," Phys. Rev. B **86**, 144107 (2012).

[44] S. Yamanaka, T. Maekawa, H. Muta, T. Matsuda, S. Kobayashi, and K. Kurosaki, "Thermophysical properties of $SrHfO_3$ and $SrRuO_3$," J. Solid State Chem. **177**, 3484 (2004).

[45] B. Dabrowski, M. Avdeev, O. Chmaissem, S. Kolesnik, P. W. Klamut, M. Maxwell, and J. D. Jorgensen, "Freezing of octahedral tilts below the Curie temperature in $SrRu_{1-v}O_3$ perovskites," Phys. Rev. B **71**, 104411 (2005).

[46] J. J. Hamlin, S. Deemyad, J. S. Schilling, M. K. Jacobsen, R. S. Kumar, A. L. Cornelius, G. Cao, and J. J. Neumeier, "ac susceptibility studies of the weak itinerant ferromagnet $SrRuO_3$ under high pressure to 34 GPa," Phys. Rev. B **76**, 014432 (2007).

[47] A. Vailionis, H. Boschker, W. Siemons, E. P. Houwman, D. H. A. Blank, G. Rijnders, and G. Koster, "Misfit strain accommodation in epitaxial ABO_3 perovskites: Lattice rotations and lattice modulations," Phys. Rev. B **83**, 064101 (2011).

[48] S. H. Chang, Y. J. Chang, S. Y. Jang, D. W. Jeong, C. U. Jung, Y.-J. Kim, J.-S. Chung, and T. W. Noh, "Thickness-dependent structural phase transition of strained $SrRuO_3$ ultrathin films: The role of octahedral tilt," Phys. Rev. B **84**, 104101 (2011).

[49] A. Herklotz, M. Kataja, K. Nenkov, M. D. Biegalski, H.-M. Christen, C. Deneke, L. Schultz, and K. Dörr, "Magnetism of the tensile-strain-induced tetragonal state of $SrRuO_3$ films," Phys. Rev. B **88**, 144412 (2013).

[50] W. Lu, W. Dong Song, K. He, J. Chai, C.-J. Sun, G.-M. Chow, and J.-S. Chen, "The role of octahedral tilting in the structural phase transition and magnetic anisotropy in $SrRuO_3$ thin film," J. Appl. Phys. **113**, 063901 (2013).

[51] P. Fulde, *Correlated Electrons in Quantum Matter* (World Scientific, Singapore, 2012).

[52] R. A. Evarestov, *Quantum Chemistry of Solids: The LCAO First Principles Treatment of Crystals* (Springer, Berlin, 2007).

[53] J. P. Perdew, A. Ruzsinszky, J. Tao, V. N. Staroverov, G. E. Scuseria, and G. I. Csonka, "Prescription for the design and selection of density functional approximations: More constraint satisfaction with fewer fits," J. Chem. Phys. **123**, 062201 (2005).

[54] K. G. Dyall and K. Fægri, *Introduction to Relativistic Quantum Chemistry* (Oxford University Press, New York, 2007).

[55] F. Jensen, *Introduction to Computational Chemistry* (John Wiley & Sons, Chichester, 1999).

[56] W. Koch and M. C. Holthausen, *A Chemist's Guide to Density Functional Theory* (Wiley-VCH, Weinheim, 2001).

[57] P. Hohenberg and W. Kohn, "Inhomogeneous electron gas," Phys. Rev. **136**, B864 (1964).

[58] W. Kohn and L. J. Sham, "Self-consistent equations including exchange and correlation effects," Phys. Rev. **140**, A1133 (1965).

[59] R. G. Parr and W. Yang, *Density-Functional Theory of Atoms and Molecules* (Oxford University Press, New York, 1989).

[60] P. Atkins and R. Friedman, *Molecular Quantum Mechanics* (Oxford University Press, New York, 2005).

[61] D. R. Hartree, "The wave mechanics of an atom with a non-Coulomb central field. Part I. Theory and methods, Part II. Some results and discussion, Part III. Term values and intensities in series in optical spectra," Proc. Camb. Phil. Soc. **24**, 89, 111, 426 (1928).

[62] V. Fock, "Näherungsmethode zur lösung des quantenmechanischen mehrkörperproblems [An approximate method for solving the quantum mechanical many-body problem]," Z. Phys. **61**, 126 (1930).

[63] E. J. Baerends and O. V. Gritsenko, "A quantum chemical view of density functional theory," J. Phys. Chem. A **101**, 5383 (1997).

[64] L. H. Thomas, "The calculation of atomic fields," Proc. Camb. Phil. Soc. **23**, 542 (1927).

[65] E. Fermi, "Eine statistische methode zur bestimmung einiger eigenschaften des atoms und ihre anwendung auf die theorie des periodischen systems der elemente [A statistical method for the determination of some properties of the atom and its application to the theory of the periodic system of the elements]," Z. Phys. **48**, 73 (1928).

[66] P. A. M. Dirac, "Note on exchange phenomena in the Thomas atom," Proc. Camb. Phil. Soc. **26**, 376 (1930).

[67] D. M. Ceperley and B. J. Alder, “Ground state of the electron gas by a stochastic method,” Phys. Rev. Lett. **45**, 566 (1980).

[68] S. H. Vosko, L. Wilk, and M. Nusair, “Accurate spin-dependent electron liquid correlation energies for local spin density calculations: A critical analysis,” Can. J. Phys. **58**, 1200 (1980).

[69] J. P. Perdew and A. Zunger, “Self-interaction correction to density-functional approximations for many-electron systems,” Phys. Rev. B **23**, 5048 (1981).

[70] J. P. Perdew and Y. Wang, “Accurate and simple analytic representation of the electron-gas correlation energy,” Phys. Rev. B **45**, 13244 (1992).

[71] P. Haas, F. Tran, P. Blaha, L. S. Pedroza, A. J. R. da Silva, M. M. Odashima, and K. Capelle, “Systematic investigation of a family of gradient-dependent functionals for solids,” Phys. Rev. B **81**, 125136 (2010).

[72] B. Baumeier, P. Krüger, J. Pollmann, and G. V. Vajenine, “Electronic structure of alkali-metal fluorides, oxides, and nitrides: Density-functional calculations including self-interaction corrections,” Phys. Rev. B **78**, 125111 (2008).

[73] W. Kohn, “Nobel lecture. Electronic structure of matter — wave functions and density functionals,” Rev. Mod. Phys. **71**, 1253 (1999).

[74] A. D. Becke, “Density-functional exchange-energy approximation with correct asymptotic behaviour,” Phys. Rev. A **38**, 3098 (1988).

[75] C. Lee, W. Yang, and R. G. Parr, “Development of the Colle-Salvetti correlation-energy formula into a functional of the electron density,” Phys. Rev. B **37**, 785 (1988).

[76] J. P. Perdew, K. Burke, and M. Ernzerhof, “Generalized gradient approximation made simple,” Phys. Rev. Lett. **77**, 3865 (1996).

[77] J. P. Perdew, A. Ruzsinszky, G. I. Csonka, O. A. Vydrov, G. E. Scuseria, L. A. Constantin, X. Zhou, and K. Burke, “Restoring the density-gradient expansion for exchange in solids and surfaces,” Phys. Rev. Lett. **100**, 136406 (2008).

[78] E. H. Lieb and S. Oxford, “Improved lower bound on the indirect Coulomb energy,” Int. J. Quantum Chem. **19**, 427 (1981).

[79] S.-K. Ma and K. A. Brueckner, “Correlation energy of an electron gas with a slowly varying high density,” Phys. Rev. **165**, 18 (1968).

[80] J. P. Perdew, L. A. Constantin, E. Sagvolden, and K. Burke, “Relevance of the slowly varying electron gas to atoms, molecules, and solids,” Phys. Rev. Lett. **97**, 223002 (2006).

[81] P. Haas, F. Tran, P. Blaha, K. Schwarz, and R. Laskowski, "Insight into the performance of GGA functionals for solid-state calculations," Phys. Rev. B **80**, 195109 (2009).

[82] P. Haas, F. Tran, and P. Blaha, "Calculation of the lattice constant of solids with semilocal functionals," Phys. Rev. B **79**, 085104 (2009).

[83] D. M. Roessler and W. C. Walker, "Electronic spectrum and ultraviolet optical properties of crystalline MgO," Phys. Rev. **159**, 733 (1967).

[84] L. S. Pedroza, A. J. R. da Silva, and K. Capelle, "Gradient-dependent density functionals of the Perdew-Burke-Ernzerhof type for atoms, molecules, and solids," Phys. Rev. B **79**, 201106 (2009).

[85] G. I. Csonka, J. P. Perdew, A. Ruzsinszky, P. H. T. Philipsen, S. Lebègue, J. Paier, O. A. Vydrov, and J. G. Ángyán, "Assessing the performance of recent density functionals for bulk solids," Phys. Rev. B **79**, 155107 (2009).

[86] S. Kurth and J. P. Perdew, "Density-functional correction of random-phase-approximation correlation with results for jellium surface energies," Phys. Rev. B **59**, 10461 (1999).

[87] S. Kurth, J. P. Perdew, and P. Blaha, "Molecular and solid-state tests of density functional approximations: LSD, GGAs, and meta-GGAs," Int. J. Quantum Chem. **75**, 889 (1999).

[88] V. N. Staroverov, G. E. Scuseria, J. Tao, and J. P. Perdew, "Tests of a ladder of density functionals for bulk solids and surfaces," Phys. Rev. B **69**, 075102 (2004).

[89] J. Tao, J. P. Perdew, V. N. Staroverov, and G. E. Scuseria, "Climbing the density functional ladder: Non-empirical meta-generalized gradient approximation designed for molecules and solids," Phys. Rev. Lett. **91**, 146401 (2003).

[90] V. N. Staroverov, G. E. Scuseria, J. Tao, and J. P. Perdew, "Comparative assessment of a new nonempirical density functional: Molecules and hydrogen-bonded complexes," J. Chem. Phys. **119**, 12129 (2003).

[91] Y. Zhang and W. Yang, "Comment on "Generalized gradient approximation made simple"," Phys. Rev. Lett. **80**, 890 (1998).

[92] B. Hammer, L. B. Hansen, and J. K. Nørskov, "Improved adsorption energetics within density-functional theory using revised Perdew-Burke-Ernzerhof functionals," Phys. Rev. B **59**, 7413 (1999).

[93] P. R. Antoniewicz and L. Kleinman, "Kohn-Sham exchange potential exact to first order in $\rho(K \rightarrow)/\rho_0$," Phys. Rev. B **31**, 6779 (1985).

[94] Y. Zhao and D. G. Truhlar, "Construction of a generalized gradient approximation by restoring the density-gradient expansion and enforcing a tight Lieb-Oxford bound," J. Chem. Phys. **128**, 184109 (2008).

[95] A. Ruzsinszky, G. I. Csonka, and G. E. Scuseria, “Regularized gradient expansion for atoms, molecules, and solids,” J. Chem. Theory Comput. **5**, 763 (2009).

[96] M. Ropo, K. Kokko, and L. Vitos, “Assessing the Perdew-Burke-Ernzerhof exchange-correlation density functional revised for metallic bulk and surface systems,” Phys. Rev. B **77**, 195445 (2008).

[97] G. I. Csonka, A. Ruzsinszky, J. P. Perdew, and S. Grimme, “Improved description of stereoelectronic effects in hydrocarbons using semilocal density functional theory,” J. Chem. Theory Comput. **4**, 888 (2008).

[98] R. Wahl, D. Vogtenhuber, and G. Kresse, “$SrTiO_3$ and $BaTiO_3$ revisited using the projector augmented wave method: Performance of hybrid and semilocal functionals,” Phys. Rev. B **78**, 104116 (2008).

[99] J. P. Perdew, A. Ruzsinszky, G. I. Csonka, L. A. Constantin, and J. Sun, “Workhorse semilocal density functional for condensed matter physics and quantum chemistry,” Phys. Rev. Lett. **103**, 026403 (2009).

[100] P. Hao, Y. Fang, J. Sun, G. I. Csonka, P. H. T. Philipsen, and J. P. Perdew, “Lattice constants from semilocal density functionals with zero-point phonon correction,” Phys. Rev. B **85**, 014111 (2012).

[101] J. Sun, M. Marsman, A. Ruzsinszky, G. Kresse, and J. P. Perdew, “Improved lattice constants, surface energies, and CO desorption energies from a semilocal density functional,” Phys. Rev. B **83**, 121410 (2011).

[102] Z. Wu and R. E. Cohen, “More accurate generalized gradient approximation for solids,” Phys. Rev. B **73**, 235116 (2006).

[103] F. Tran, R. Laskowski, P. Blaha, and K. Schwarz, “Performance on molecules, surfaces, and solids of the Wu-Cohen GGA exchange-correlation energy functional,” Phys. Rev. B **75**, 115131 (2007).

[104] A. D. Becke, “A new mixing of Hartree-Fock and local density-functional theories,” J. Chem. Phys. **98**, 1372 (1993).

[105] A. D. Becke, “Density-functional thermochemistry. III. The role of exact exchange,” J. Chem. Phys. **98**, 5648 (1993).

[106] P. J. Stephens, F. J. Devlin, C. F. Chabalowski, and M. J. Frisch, “*Ab initio* calculation of vibrational absorption and circular dichroism spectra using density functional force fields,” J. Phys. Chem. **98**, 11623 (1994).

[107] J. P. Perdew, M. Ernzerhof, and K. Burke, “Rationale for mixing exact exchange with density functional approximations,” J. Chem. Phys. **105**, 9982 (1996).

[108] K. Burke, M. Ernzerhof, and J. P. Perdew, “The adiabatic connection method: A non-empirical hybrid,” Chem. Phys. Lett. **265**, 115 (1997).

[109] C. Adamo and V. Barone, “Toward reliable density functional methods without adjustable parameters: The PBE0 model,” J. Chem. Phys. **110**, 6158 (1999).

[110] J. Paier, M. Marsman, K. Hummer, G. Kresse, I. C. Gerber, and J. G. Ángyán, “Screened hybrid density functionals applied to solids,” J. Chem. Phys. **124**, 154709 (2006).

[111] I. C. Gerber, J. G. Ángyán, M. Marsman, and G. Kresse, “Range separated hybrid density functional with long-range Hartree-Fock exchange applied to solids,” J. Chem. Phys. **127**, 054101 (2007).

[112] J. Heyd, J. E. Peralta, G. E. Scuseria, and R. L. Martin, “Energy band gaps and lattice parameters evaluated with the Heyd-Scuseria-Ernzerhof screened hybrid functional,” J. Chem. Phys. **123**, 174101 (2005).

[113] J. Muscat, A. Wander, and N. Harrison, “On the prediction of band gaps from hybrid functional theory,” Chem. Phys. Lett. **342**, 397 (2001).

[114] S. Kümmel and L. Kronik, “Orbital-dependent density functionals: Theory and applications,” Rev. Mod. Phys. **80**, 3 (2008).

[115] J. Paier, M. Marsman, and G. Kresse, “Why does the B3LYP hybrid functional fail for metals?,” J. Chem. Phys. **127**, 024103 (2007).

[116] A. Stroppa and S. Picozzi, “Hybrid functional study of proper and improper multiferroics,” Phys. Chem. Chem. Phys. **12**, 5405 (2010).

[117] B. G. Janesko, T. M. Henderson, and G. E. Scuseria, “Screened hybrid density functionals for solid-state chemistry and physics,” Phys. Chem. Chem. Phys. **11**, 443 (2009).

[118] O. A. Vydrov and G. E. Scuseria, “Effect of the Perdew-Zunger self-interaction correction on the thermochemical performance of approximate density functionals,” J. Chem. Phys. **121**, 8187 (2004).

[119] A. Filippetti and N. A. Spaldin, “Self-interaction-corrected pseudopotential scheme for magnetic and strongly-correlated systems,” Phys. Rev. B **67**, 125109 (2003).

[120] L. Petit, A. Svane, Z. Szotek, and W. M. Temmerman, “First-principles study of rare-earth oxides,” Phys. Rev. B **72**, 205118 (2005).

[121] C. J. Cramer, *Essentials of Computational Chemistry: Theories and Models* (John Wiley & Sons, Chichester, 2004).

[122] T. Archer, C. D. Pemmaraju, S. Sanvito, C. Franchini, J. He, A. Filippetti, P. Delugas, D. Puggioni, V. Fiorentini, R. Tiwari, and P. Majumdar, “Exchange interactions and magnetic phases of transition metal oxides: Benchmarking advanced *ab initio* methods,” Phys. Rev. B **84**, 115114 (2011).

[123] S. Patchkovskii and T. Ziegler, “Improving “difficult” reaction barriers with self-interaction corrected density functional theory,” J. Chem. Phys. **116**, 7806 (2002).

[124] B. G. Johnson, C. A. Gonzales, P. M. Gill, and J. A. Pople, “A density functional study of the simplest hydrogen abstraction reaction. Effect of self-interaction correction,” Chem. Phys. Lett. **221**, 100 (1994).

[125] G. I. Csonka and B. G. Johnson, “Inclusion of exact exchange for self-interaction corrected H3 density functional potential energy surface,” Theor. Chem. Acc. **99**, 158 (1998).

[126] S. Patchkovskii and T. Ziegler, “Phosphorus NMR chemical shifts with self-interaction free, gradient-corrected DFT,” J. Phys. Chem. A **106**, 1088 (2002).

[127] S. Goedecker and C. J. Umrigar, “Critical assessment of the self-interaction-corrected local-density-functional method and its algorithmic implementation,” Phys. Rev. A **55**, 1765 (1997).

[128] D. Vogel, P. Krüger, and J. Pollmann, “Self-interaction and relaxation-corrected pseudopotentials for II-VI semiconductors,” Phys. Rev. B **54**, 5495 (1996).

[129] B. Baumeier, P. Krüger, and J. Pollmann, “Bulk and surface electronic structures of alkaline-earth metal oxides: Bound surface and image-potential states from first principles,” Phys. Rev. B **76**, 205404 (2007).

[130] V. I. Anisimov, J. Zaanen, and O. K. Andersen, “Band theory and Mott insulators: Hubbard U instead of Stoner I,” Phys. Rev. B **44**, 943 (1991).

[131] L. Hedin, “New method for calculating the one-particle Green’s function with application to the electron-gas problem,” Phys. Rev. **139**, A796 (1965).

[132] A. Georges, G. Kotliar, W. Krauth, and M. J. Rozenberg, “Dynamical mean-field theory of strongly correlated fermion systems and the limit of infinite dimensions,” Rev. Mod. Phys. **68**, 13 (1996).

[133] R. Gillen, S. J. Clark, and J. Robertson, “Nature of the electronic bandgap in lanthanide oxides,” Phys. Rev. B **87**, 125116 (2013).

[134] S. J. Clark and J. Robertson, “Screened exchange density functional applied to solids,” Phys. Rev. B **82**, 085208 (2010).

[135] G. Pacchioni, “Modeling doped and defective oxides in catalysis with density functional theory methods: Room for improvements,” J. Chem. Phys. **128**, 182505 (2008).

[136] V. Eyert, “VO_2: A novel view from band theory,” Phys. Rev. Lett. **107**, 016401 (2011).

[137] Y. Guo, S. J. Clark, and J. Robertson, “Electronic and magnetic properties of Ti_2O_3, Cr_2O_3, and Fe_2O_3 calculated by the screened exchange hybrid density functional,” J. Phys.: Condens. Matter **24**, 325504 (2012).

[138] W. Heitler and F. London, “Wechselwirkung neutraler atome und homöopolare bindung nach der quantenmechanik [The interaction of neutral atoms and homopolar bond according to quantum mechanics],” Z. Phys. **44**, 455 (1927).

[139] G. Kotliar, S. Y. Savrasov, K. Haule, V. S. Oudovenko, O. Parcollet, and C. A. Marianetti, “Electronic structure calculations with dynamical mean-field theory,” Rev. Mod. Phys. **78**, 865 (2006).

[140] E. Morosan, D. Natelson, A. H. Nevidomskyy, and Q. Si, “Strongly correlated materials,” Adv. Mater. **24**, 4896 (2012).

[141] G. Kotliar and D. Vollhardt, “Strongly correlated materials: Insights from dynamical mean-field theory,” Phys. Today **57**, 53 (2004).

[142] R. Dovesi, V. R. Saunders, C. Roetti, R. Orlando, C. M. Zicovich-Wilson, F. Pascale, B. Civalleri, K. Doll, N. M. Harrison, I. J. Bush, P. D’Arco, and M. Llunell, CRYSTAL09 User’s Manual (University of Torino, Torino, 2009).

[143] C. G. Broyden, “The convergence of a class of double-rank minimization algorithms. 1. General considerations,” IMA J. Appl. Math. **6**, 76 (1970).

[144] C. G. Broyden, “The convergence of a class of double-rank minimization algorithms. 2. The new algorithm,” IMA J. Appl. Math. **6**, 222 (1970).

[145] R. Fletcher, “A new approach to variable metric algorithms,” Comput. J. **13**, 317 (1970).

[146] D. Goldfarb, “A family of variable-metric methods derived by variational means,” Math. Comput. **24**, 23 (1970).

[147] D. F. Shanno, “Conditioning of quasi-Newton methods for function minimization,” Math. Comput. **24**, 647 (1970).

[148] H. B. Schlegel, “Estimating the hessian for gradient-type geometry optimizations,” Theoret. Chim. Acta **66**, 333 (1984).

[149] J. M. Wittbrodt and H. B. Schlegel, “Estimating stretching force constants for geometry optimization,” J. Mol. Struc. (THEOCHEM) **398-399**, 55 (1997).

[150] D. D. Johnson, “Modified Broyden’s method for accelerating convergence in self-consistent calculations,” Phys. Rev. B **38**, 12807 (1988).

[151] D. R. Hamann, “Semiconductor charge densities with hard-core and soft-core pseudopotentials,” Phys. Rev. Lett. **42**, 662 (1979).

[152] P. J. Hay and W. R. Wadt, "*Ab initio* effective core potentials for molecular calculations. Potentials for K to Au including the outermost core orbitals," J. Chem. Phys. **82**, 299 (1985).

[153] S. Piskunov, E. Heifets, R. Eglitis, and G. Borstel, "Bulk properties and electronic structure of $SrTiO_3$, $BaTiO_3$, $PbTiO_3$ perovskites: An *ab initio* HF/DFT study," Comput. Mater. Sci. **29**, 165 (2004).

[154] M. Couty and M. B. Hall, "Basis sets for transition metals: Optimized outer p functions," J. Comput. Chem. **17**, 1359 (1996).

[155] L. Valenzano, F. J. Torres, D. Klaus, F. Pascale, C. M. Zicovich-Wilson, and R. Dovesi, "*Ab initio* study of the vibrational spectrum and related properties of crystalline compounds: The case of $CaCO_3$ calcite," Z. Phys. Chem. **220**, 893 (2006).

[156] M. F. Peintinger, D. V. Oliveira, and T. Bredow, "Consistent Gaussian basis sets of triple-zeta valence with polarization quality for solid-state calculations," J. Comput. Chem. **34**, 451 (2013).

[157] R. A. Evarestov, E. A. Kotomin, Y. A. Mastrikov, D. Gryaznov, E. Heifets, and J. Maier, "Comparative density-functional LCAO and plane-wave calculations of $LaMnO_3$ surfaces," Phys. Rev. B **72**, 214411 (2005).

[158] DIRAC, a relativistic *ab initio* electronic structure program, Release DIRAC08 (2008), written by L. Visscher, H. J. A. Jensen, and T. Saue, with new contributions from R. Bast, S. Dubillard, K. G. Dyall, U. Ekström, E. Eliav, T. Fleig, A. S. P. Gomes, T. U. Helgaker, J. Henriksson, M. Iliaš, Ch. R. Jacob, S. Knecht, P. Norman, J. Olsen, M. Pernpointner, K. Ruud, P. Sałek, and J. Sikkema (see http://dirac.chem.sdu.dk).

[159] M. J. Frisch, G. W. Trucks, H. B. Schlegel, G. E. Scuseria, M. A. Robb, J. R. Cheeseman, J. A. Montgomery, Jr., T. Vreven, K. N. Kudin, J. C. Burant, J. M. Millam, S. S. Iyengar, J. Tomasi, V. Barone, B. Mennucci, M. Cossi, G. Scalmani, N. Rega, G. A. Petersson, H. Nakatsuji, M. Hada, M. Ehara, K. Toyota, R. Fukuda, J. Hasegawa, M. Ishida, T. Nakajima, Y. Honda, O. Kitao, H. Nakai, M. Klene, X. Li, J. E. Knox, H. P. Hratchian, J. B. Cross, V. Bakken, C. Adamo, J. Jaramillo, R. Gomperts, R. E. Stratmann, O. Yazyev, A. J. Austin, R. Cammi, C. Pomelli, J. W. Ochterski, P. Y. Ayala, K. Morokuma, G. A. Voth, P. Salvador, J. J. Dannenberg, V. G. Zakrzewski, S. Dapprich, A. D. Daniels, M. C. Strain, O. Farkas, D. K. Malick, A. D. Rabuck, K. Raghavachari, J. B. Foresman, J. V. Ortiz, Q. Cui, A. G. Baboul, S. Clifford, J. Cioslowski, B. B. Stefanov, G. Liu, A. Liashenko, P. Piskorz, I. Komaromi, R. L. Martin, D. J. Fox, T. Keith, M. A. Al-Laham, C. Y. Peng, A. Nanayakkara, M. Challacombe, P. M. W. Gill, B. Johnson, W. Chen, M. W. Wong, C. Gonzalez, and J. A. Pople, Gaussian 03, Revision C.02, Gaussian, Inc., Wallingford, CT, 2004.

[160] M. Iliaš, H. J. A. Jensen, V. Kellö, B. O. Roos, and M. Urban, "Theoretical study of PbO and the PbO anion," Chem. Phys. Lett. **408**, 210 (2005).

[161] A. S. P. Gomes, K. G. Dyall, and L. Visscher, “Relativistic double-zeta, triple-zeta, and quadruple-zeta basis sets for the lanthanides La–Lu,” Theor. Chem. Acc. **127**, 369 (2010).

[162] K. D. Dobbs and W. J. Hehre, “Molecular orbital theory of the properties of inorganic and organometallic compounds. 5. Extended basis sets for first-row transition metals,” J. Comput. Chem. **8**, 861 (1987).

[163] W. J. Hehre, R. Ditchfield, R. F. Stewart, and J. A. Pople, “Self-consistent molecular orbital methods. IV. Use of Gaussian expansions of Slater-type orbitals. Extension to second-row molecules,” J. Chem. Phys. **52**, 2769 (1970).

[164] G. Grimvall, *Thermophysical Properties of Materials* (North-Holland, Amsterdam, 1999).

[165] D. C. Wallace, *Thermodynamics of Crystals* (Dover Publications, New York, 1998).

[166] O. Beckstein, J. E. Klepeis, G. L. W. Hart, and O. Pankratov, “First-principles elastic constants and electronic structure of $\alpha-$Pt$_2$Si and PtSi,” Phys. Rev. B **63**, 134112 (2001).

[167] W. Voigt, *Lehrbuch der Kristallphysik* [Textbook on Crystal Physics] (Teubner, Leipzig, 1928).

[168] A. Reuss, “Berechnung der fließgrenze von mischkristallen auf grund der plastizitätsbedingung für einkristalle [Estimation of the yield surface of polycrystals based on the plastic behaviour of single crystals],” Z. Angew. Math. Mech. **9**, 49 (1929).

[169] R. Hill, “The elastic behaviour of a crystalline aggregate,” Proc. Phys. Soc. London Sect. A **65**, 349 (1952).

[170] F. Birch, “Finite elastic strain of cubic crystals,” Phys. Rev. **71**, 809 (1947).

[171] A. M. Glazer, “The classification of tilted octahedra in perovskites,” Acta Cryst. B **28**, 3384 (1972).

[172] L. Guan, B. Liu, L. Jin, J. Guo, Q. Zhao, Y. Wang, and G. Fu, “Electronic structure and optical properties of LaNiO$_3$: First-principles calculations,” Solid State Commun. **150**, 2011 (2010).

[173] A. B. Alchagirov, J. P. Perdew, J. C. Boettger, R. C. Albers, and C. Fiolhais, “Energy and pressure versus volume: Equations of state motivated by the stabilized jellium model,” Phys. Rev. B **63**, 224115 (2001).

[174] J. L. García-Muñoz, J. Rodríguez-Carvajal, P. Lacorre, and J. B. Torrance, “Neutron-diffraction study of RNiO$_3$ (R=La,Pr,Nd,Sm): Electronically induced structural changes across the metal-insulator transition,” Phys. Rev. B **46**, 4414 (1992).

[175] Š. Masys, S. Mickevičius, S. Grebinskij, and V. Jonauskas, "Electronic structure of LaNiO_{3-x} thin films studied by x-ray photoelectron spectroscopy and density functional theory," Phys. Rev. B **82**, 165120 (2010).

[176] J. Choisnet, R. Evarestov, I. Tupitsyn, and V. Veryazov, "Investigation of the chemical bonding in nickel mixed oxides from electronic structure calculations," J. Phys. Chem. Solids **57**, 1839 (1996).

[177] B. J. Kennedy, B. A. Hunter, and J. R. Hester, "Synchrotron x-ray diffraction reexamination of the sequence of high-temperature phases in SrRuO_3," Phys. Rev. B **65**, 224103 (2002).

[178] B. C. Chakoumakos, S. E. Nagler, S. T. Misture, and H. M. Christen, "High-temperature structural behavior of SrRuO_3," Physica B **241-243**, 358 (1998).

[179] S. N. Bushmeleva, V. Y. Pomjakushin, E. V. Pomjakushina, D. V. Sheptyakov, and A. M. Balagurov, "Evidence for the band ferromagnetism in SrRuO_3 from neutron diffraction," J. Magn. Magn. Mat. **305**, 491 (2006).

[180] Š. Masys and V. Jonauskas, "A first-principles study of structural and elastic properties of bulk SrRuO_3," J. Chem. Phys. **139**, 224705 (2013).

[181] J. Manica, M. Abbate, J. Gayone, J. Guevara, and S. Cuffini, "O 1s X-ray absorption spectra and band structure calculations of $\text{Ca}_{1-x}\text{Sr}_x\text{RuO}_3$," J. Alloys Compd. **377**, 25 (2004).

[182] K. Maiti, "Role of covalency in the ground-state properties of perovskite ruthenates: A first-principles study using local spin density approximations," Phys. Rev. B **73**, 235110 (2006).

[183] S. Grebinskij, Š. Masys, S. Mickevičius, V. Lisauskas, and V. Jonauskas, "*Ab initio* and photoemission study of correlation effects in SrRuO_3 thin films," Phys. Rev. B **87**, 035106 (2013).

[184] J. Park, S.-J. Oh, J.-H. Park, D. M. Kim, and C.-B. Eom, "Electronic structure of epitaxial $(\text{Sr,Ca})\text{RuO}_3$ films studied by photoemission and x-ray absorption spectroscopy," Phys. Rev. B **69**, 085108 (2004).

[185] K. Maiti and R. S. Singh, "Evidence against strong correlation in 4d transition-metal oxides CaRuO_3 and SrRuO_3," Phys. Rev. B **71**, 161102 (2005).

[186] K. Maiti, R. S. Singh, and V. R. R. Medicherla, "Evolution of a band insulating phase from a correlated metallic phase," Phys. Rev. B **76**, 165128 (2007).

[187] R. S. Singh, V. R. R. Medicherla, and K. Maiti, "Role of electron correlation and long range magnetic order in the electronic structure of Ca(Sr)RuO_3," Physica B **403**, 1398 (2008).

[188] M. Takizawa, D. Toyota, H. Wadati, A. Chikamatsu, H. Kumigashira, A. Fujimori, M. Oshima, Z. Fang, M. Lippmaa, M. Kawasaki, and H. Koinuma, "Manifestation of correlation effects in the photoemission spectra of $Ca_{1-x}Sr_xRuO_3$," Phys. Rev. B **72**, 060404 (2005).

[189] H. Kumigashira, M. Minohara, M. Takizawa, A. Fujimori, D. Toyota, I. Ohkubo, M. Oshima, M. Lippmaa, and M. Kawasaki, "Interfacial electronic structure of $SrTiO_3/SrRuO_3$ heterojuctions studied by *in situ* photoemission spectroscopy," Appl. Phys. Lett. **92**, 122105 (2008).

[190] D. Toyota, I. Ohkubo, H. Kumigashira, M. Oshima, T. Ohnishi, M. Lippmaa, M. Takizawa, A. Fujimori, K. Ono, M. Kawasaki, and H. Koinuma, "Thickness-dependent electronic structure of ultrathin $SrRuO_3$ films studied by *in situ* photoemission spectroscopy," Appl. Phys. Lett. **87**, 162508 (2005).

[191] http://lasurface.com/xps/imfpgrapher.php#

[192] J. J. Yeh and I. Lindau, "Atomic subshell photoionization cross sections and asymmetry parameters: $1 \leq Z \leq 103$," At. Data Nucl. Data Tables **32**, 1 (1985).

[193] J. J. Yeh and I. Lindau, *Atomic Calculation of Photoionization Cross-Sections and Asymmetry Parameters* (Gordon and Breach Science Publishers, Langhorne, 1993).

[194] A. Vailionis, W. Siemons, and G. Koster, "Room temperature epitaxial stabilization of a tetragonal phase in ARuO$_3$ (A = Ca and Sr) thin films," Appl. Phys. Lett. **93**, 051909 (2008).

[195] J. Shin, S. Kalinin, H. Lee, H. Christen, R. Moore, E. Plummer, and A. Baddorf, "Surface stability of epitaxial $SrRuO_3$ films," Surf. Sci. **581**, 118 (2005).

[196] Š. Masys, V. Jonauskas, S. Grebinskij, S. Mickevičius, V. Pakštas, and M. Senulis, "Theoretical and experimental study of non-stoichiometric $SrRuO_3$: A role of oxygen vacancies in electron correlation effects," Lith. J. Phys. **53**, 150 (2013).

[197] C. Etz, I. V. Maznichenko, D. Böttcher, J. Henk, A. N. Yaresko, W. Hergert, I. I. Mazin, I. Mertig, and A. Ernst, "Indications of weak electronic correlations in $SrRuO_3$ from first-principles calculations," Phys. Rev. B **86**, 064441 (2012).

[198] S. F. Pugh, "XCII. Relations between the elastic moduli and the plastic properties of polycrystalline pure metals," Philos. Mag. **45**, 823 (1954).

[199] I. N. Frantsevich, F. F. Voronov, and S. A. Bokuta, *Elastic Constants and Elastic Moduli of Metals and Insulators* (Naukova Dumka, Kiev, 1982).

[200] D. H. Chung and W. R. Buessem, "The elastic anisotropy of crystals," J. Appl. Phys. **38**, 2010 (1967).

[201] S. I. Ranganathan and M. Ostoja-Starzewski, "Universal elastic anisotropy index," Phys. Rev. Lett. **101**, 055504 (2008).

[202] L. G. Wang, M. Šob, and Z. Zhang, "Instability of higher-energy phases in simple and transition metals," J. Phys. Chem. Solids **64**, 863 (2003).

[203] W. F. Perger, J. Criswell, B. Civalleri, and R. Dovesi, "*Ab-initio* calculation of elastic constants of crystalline systems with the CRYSTAL code," Comput. Phys. Commun. **180**, 1753 (2009).

[204] J. M. Rondinelli and S. Coh, "Large isosymmetric reorientation of oxygen octahedra rotation axes in epitaxially strained perovskites," Phys. Rev. Lett. **106**, 235502 (2011).

[205] S. J. May, J.-W. Kim, J. M. Rondinelli, E. Karapetrova, N. A. Spaldin, A. Bhattacharya, and P. J. Ryan, "Quantifying octahedral rotations in strained perovskite oxide films," Phys. Rev. B **82**, 014110 (2010).

[206] R. J. Zeches, M. D. Rossell, J. X. Zhang, A. J. Hatt, Q. He, C. H. Yang, A. Kumar, C. H. Wang, A. Melville, C. Adamo, G. Sheng, Y. H. Chu, J. F. Ihlefeld, R. Erni, C. Ederer, V. Gopalan, L. Q. Chen, D. G. Schlom, N. A. Spaldin, L. W. Martin, and R. Ramesh, "A strain-driven morphotropic phase boundary in $BiFeO_3$," Science **326**, 977 (2009).

[207] A. J. Hatt, N. A. Spaldin, and C. Ederer, "Strain-induced isosymmetric phase transition in $BiFeO_3$," Phys. Rev. B **81**, 054109 (2010).

[208] W. Pauli, "Über den zusammenhang des abschlusses der elektronengruppen im atom mit der komplexstruktur der spektren [On the connection between the closing of electron groups in atoms and the complex structure of spectra]," Z. Phys. **31**, 765 (1925).

[209] J. C. Slater, "The theory of complex spectra," Phys. Rev. **34**, 1293 (1929).

[210] R. McWeeny, *Methods of Molecular Quantum Mechanics* (Academic Press, London, 1992).

[211] J. Harris, "Adiabatic-connection approach to Kohn-Sham theory," Phys. Rev. A **29**, 1648 (1984).